MEAN FLOW CHARACTERIZATION OF SWEPT SHOCK/TURBULENT BOUNDARY LAYER
INTERACTIONS INDUCED BY AN IMPINGING OBLIQUE SHOCK

by

Jesse Groves

A Thesis Submitted to the Faculty of the

DEPARTMENT OF AEROSPACE AND MECHANICAL ENGINEERING

In Partial Fulfillment of the Requirements

For the Degree of

MASTER OF SCIENCE

In the Graduate College

THE UNIVERSITY OF ARIZONA

2024

THE UNIVERSITY OF ARIZONA
GRADUATE COLLEGE

As members of the Master's Committee, we certify that we have read the thesis
prepared by: Jesse Groves
titled: Mean Flow Characterization of Swept Shock/Turbulent Boundary Layer
                 Interactions Induced by an Impinging Oblique Shock

and recommend that it be accepted as fulfilling the thesis requirement for the Master's Degree.

James Threadgill
_____   Date: _Jan 13, 2025_
James Threadgill

Jesse Little
Jesse Little (Jan 13, 2025 15:30 EST)
_____   Date: _Jan 13, 2025_
Jesse Little

_____   Date: _Jan 13, 2025_
Alex Craig

Final approval and acceptance of this thesis is contingent upon the candidate's submission of the
final copies of the thesis to the Graduate College.

We hereby certify that we have read this thesis prepared under our direction and recommend that
it be accepted as fulfilling the Master's requirement.

James Threadgill
_____   Date: _Jan 13, 2025_
James Threadgill
Thesis Committee Chair
Department of Aerospace and Mechanical Engineering

Jesse Little
Jesse Little (Jan 13, 2025 15:30 EST)
_____   Date: _Jan 13, 2025_
Jesse Little
Thesis Committee Co-Chair
Department of Aerospace and Mechanical Engineering

ACKNOWLEDGMENTS

LAND ACKNOWLEDGMENT

We respectfully acknowledge the University of Arizona is on the land and territories of Indigenous peoples. Today, Arizona is home to 22 federally recognized tribes, with Tucson being home to the O'odham and the Yaqui. Committed to diversity and inclusion, the University strives to build sustainable relationships with sovereign Native Nations and Indigenous communities through education offerings, partnerships, and community service.

DEDICATION

Dedicated to my grandfather. You continue to inspire me to be successful everyday, and I will always cherish the time we had together.

TABLE OF CONTENTS

LIST OF FIGURES

LIST OF TABLES

ABSTRACT

Experiments have been conducted in a blowdown wind tunnel at Mach 2.1 and Mach 3.0 to study swept shock boundary layer interactions (SBLIs) generated by impinging, oblique shocks on a fully turbulent boundary layer. The overall goal of this work is to determine the effect of increasing the aspect ratio of the SBLI by comparing results to similar experiments conducted in a smaller wind tunnel. Shock sweep angles (ψ) of 20° and 40° are tested at each Mach number. The quasi-infinite region is increased by increasing the aspect ratio of the shock generator from 2.33 in previous studies to 2.75 in the current study. To isolate the effect of sweep, a fixed inviscid pressure rise normal to the sweep angle of $C_{p_n} = 0.6$ is used for each case. The mean flow topology is studied using three methods: infrared thermography, mean pressure measurements, and oil flow visualization.

Mean flow results from each of the three techniques show good agreement and are able to identify salient features of the SBLI. The Stanton number distribution from infrared thermography accurately provides the location of the initial pressure rise and separation via a local minima and maxima in the Stanton number distribution. Mean pressure results also validate the locations of the initial pressure rise and separation locations determined from infrared thermography results. Oil flow shows the local skin friction direction on the SBLI surface and offers the most conclusive separation and reattachment locations, but also allows for the visualization of the initial pressure rise. The initial pressure rise and separation locations for all three methods align well, validating the use of infrared thermography to identify these salient features of the SBLI.

A local maxima of the Stanton number distribution is seen in both separated and attached SBLIs. Therefore, heat flux data can be used to aid in determining the location of the separation for the SBLI, but does not offer conclusive results for whether the flow has separated or remains attached. Further, the Stanton number distribution is not sufficient in determining a precise location of reattachment if the flow has separated. Oil flow visualization offers the most conclusive results when determining separation and reattachment.

Previous results from a smaller aspect ratio interaction show that separation exhibits conical similarity for 20° sweep in Mach 2.3 flow. However, oil flow visualization at Mach 2.1 for the larger aspect ratio interaction investigated here exhibits cylindrical behavior. This suggests that the SBLI aspect ratio influences the mean flow topology in that lower aspect ratios promote conical similarity. Comparison of the 40° sweep cases for the two different aspect ratio tests show similar structures, but Mach 3.0 results require further analysis since oil flow offers the most accurate reattachment location but was unable to be obtained for these tests.

Chapter 1

Introduction

Shock Boundary Layer Interactions (SBLIs) occur when a shock wave interacts with the boundary layer of a surface exposed to supersonic flow. These interactions have been a major area of focus for high-speed aerodynamicists over the last several decades. Due to the subsonic and supersonic regions of the boundary layer, these interactions have conflicting effects of higher viscosity effects for the subsonic region of the boundary layer, and higher compressibility and inertial forces for the supersonic portion of the boundary layer that create unique challenges for many aerospace applications such as internal and external flows related to aircraft, missiles, rockets, spacecraft, etc. These SLBIs are often associated with increased drag, unsteadiness, and high surface heat transfer, all of which have significant adverse effects on vehicle performance (Gaitonde and Adler, 2023; Clemens and Narayanaswamy, 2014; Ganapathisubramani et al., 2009; Délery and Dussauge, 2009). The unsteadiness can be of sufficiently low frequency that it couples with the vehicle structure causing severe damage.

Before delving into the specifics discussed later in the paper, it is important to highlight fundamental features of SBLIs. These interactions are driven by three main flow features: the state of the incoming boundary layer, the intensity of the pressure gradient, and the shock generation geometry. Each of these factors contributes to the likelihood the boundary layer will separate and the extent of the separation, should it occur.

The state of the incoming boundary layer could be laminar, transitional, or turbulent. It plays a major role in flow parameters such as drag and heat transfer, but it also influences the SBLI. Just as in subsonic flow, turbulent boundary layers have higher inertial forces compared to laminar boundary layers. This allows turbulent boundary layers to overcome stronger adverse pressure gradients compared to laminar boundary layers. Thus, as the boundary layer transitions from laminar to turbulent, it becomes less likely to separate (Chapman et al., 1958).

The inviscid pressure rise across the shock has a significant influence on the SBLI. For example, if the incoming flow is slightly higher than Mach 1, then the pressure rise across a normal shock will be very small and the flow is more likely to stay attached. In the normal shock case, as the Mach number is increased, the pressure rise across the shock increases. When the shock strength is sufficiently high, the boundary layer is no longer able to withstand the adverse pressure gradient and separates from the surface. Souverein et al. (2013) developed a model to determine the relation between separation length, Mach number, and
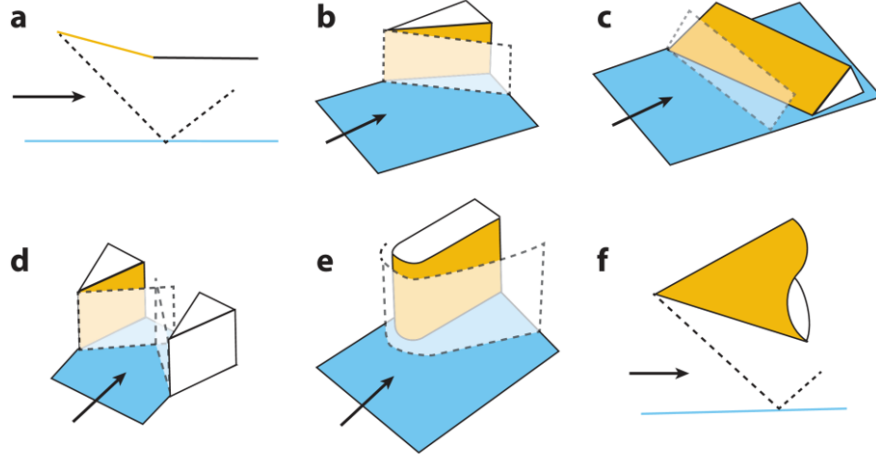
Figure 1.1: Examples of commonly used geometries to study different types of swept SBLI (Gaitonde and Adler, 2023).

shock strength. In doing this, Souverein et al. found that the interaction scale was independent of Reynolds number for higher Reynolds numbers, and only slightly dependent on Reynolds number for lower Reynolds numbers. Souverein et al. further derived Equation 1.1, where q_e is dynamic pressure of the freestream, k is a constant chosen based on Reynolds number, and Δp is the difference in pressure before and after the adverse pressure gradient (in this case, the shock). $S_e^* \geq 1$ results in a separated flow, and $S_e^* \leq 1$ results in flow that does not separation. This shows that increasing the adverse pressure gradient (shock strength) increases the separation length. Souverein et al. suggest $k = 3.0$ for $Re_\theta \leq 1 \times 10^4$ and $k = 2.5$ for $Re_\theta > 1 \times 10^4$. However, Threadgill and Bruce (2016) studied SBLIs from impinging, oblique shocks with Re_θ near this threshold of 10^4 and found that a value of $k = 2.5$ under-predicted the separation length, whereas a value of $k = 3.0$ over-predicted the separation length of the interactions, suggesting this discontinuous k criterion could require further investigation.

$$S_e^* = k\frac{\Delta p}{q_e} \tag{1.1}$$

Lastly, the geometry of the shock generator determines whether the shock is swept or unswept, and what configuration this SBLI forms. Some examples of commonly used swept SBLI configurations are shown in Figure 1.1. Examples and further explanations of the different geometries used to generate SBLIs are discussed in greater detail in the following sections.

One of the first observations of an SBLI was made by Ferri (1939) while studying an airfoil in supersonic flow. This research studied an SBLI subject to a pressure gradient induced by the airfoil, but this complex geometry created challenges for researchers to study these phenomena systematically. Later work in the 1940's and 1950's looked at SBLI with pressure gradients imposed on a flat plate. These shocks were generated with simple geometries that were easy to adjust, replicate, and allowed the pressure gradient to

be induced solely by the shock wave and not by the geometry, as in the airfoil case. Roshko and Dshawan (1952); Bardsley and Mair (1951); Gadd et al. (1954) studied SBLI induced by oblique shock waves on a flat plate. Bardsley and Mair found that as the strength of the shock increased, the boundary layer is much more likely to separate. Similarly, Roshko and Dshawan discovered that the state of the boundary layer had the highest impact on the SBLI structure. Namely, it was found that the flow separates nearly all the time when the boundary layer is laminar, but a turbulent boundary layer is much more likely to stay attached. Similarly, Gadd et al. studied these impinging, oblique SBLI, but also studied SBLI that were formed by a wedge on the SBLI surface, and found that this configuration has similar characteristics as the SBLI produced by an oblique shock wave. More recent work by Threadgill and Bruce (2016) and Souverein et al. (2013) also compared impinging, oblique SBLI with SBLI generated by a compression ramp and found that the separation length for SBLIs generated by both compression ramps and shock generators create separation lengths that scale similarly.

1.1   2-D Interactions

The simple geometries this early work focused on have proven to be very effective in isolating key aspects of the flow, and are therefore still used today (Délery and Dussauge, 2009). Some examples of this include a compression ramp (Clemens and Narayanaswamy, 2014; Ganapathisubramani et al., 2009), an impinging oblique shock (Piponniau et al., 2009), and normal shock waves (Szulc et al., 2024). These experiments are focused on interactions that have constant properties along the span of the interaction, otherwise known as two-dimensional (2-D) because a slice of the interaction can be studied and will provide an accurate model of the entire span of the interaction excluding sidewall effects. As an example, Figure 1.2 shows an impinging oblique SBLI. In an inviscid case, the oblique shock wave would simply be reflected off the surface, resulting in an immediate pressure rise. However, due to the subsonic region in the boundary layer, a portion of the flow near the wall does not have this shock wave or the associated pressure rise across the shock. This leaves a small subsonic area on the boundary layer surface where high pressure downstream and low pressure upstream smoothly transition from low pressure to high pressure rather than the immediate pressure rise as in the inviscid case. This causes the flow in the boundary layer to slow and thicken for weaker pressure rises, and can force the flow to travel upstream if the pressure gradient is sufficiently high. This creates a region of reverse flow and thickens the boundary layer downstream of the interaction as highlighted by Figure 1.2c. However, the plateau region just after separation is dependent on the strength of the impinging shock. Xue et al. (2023) tested 2-D SBLI Mach 5 flow in attempts to determine the pressure rise of the separation bubble at different shock strengths. Xue et al. showed that with higher shock strengths, this plateau is much more defined than those of the weaker shocks. An example of their findings is shown in Figure 1.3, with more normal shock angles relative to the SBLI surface equating to a stronger pressure rise. This correlates to the pressure plateau region in the corresponding pressure distributions that show minimal pressure plateau regions for weaker shocks.
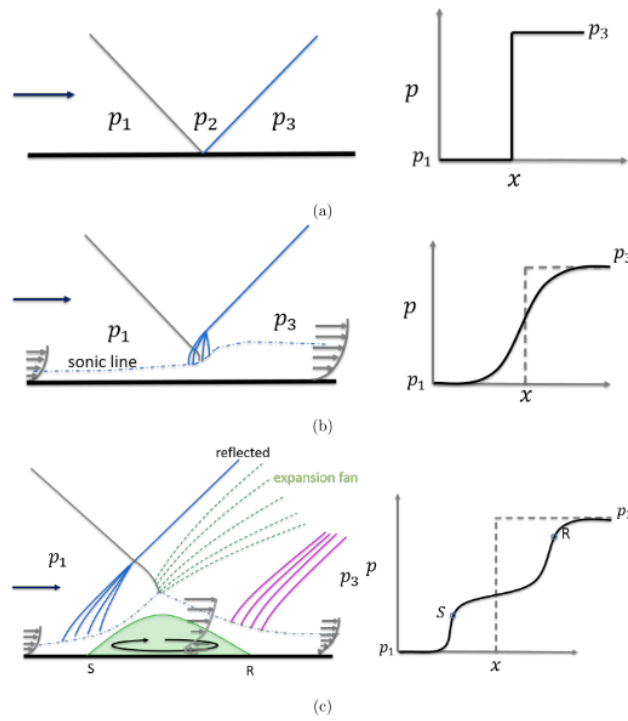
Figure 1.2: Comparison of mean pressure rise for inviscid (a), viscous with no separation (b), and viscous separated flow (c), where S and R represent separation and reattachment points respectively (Padmanabhan, 2023).
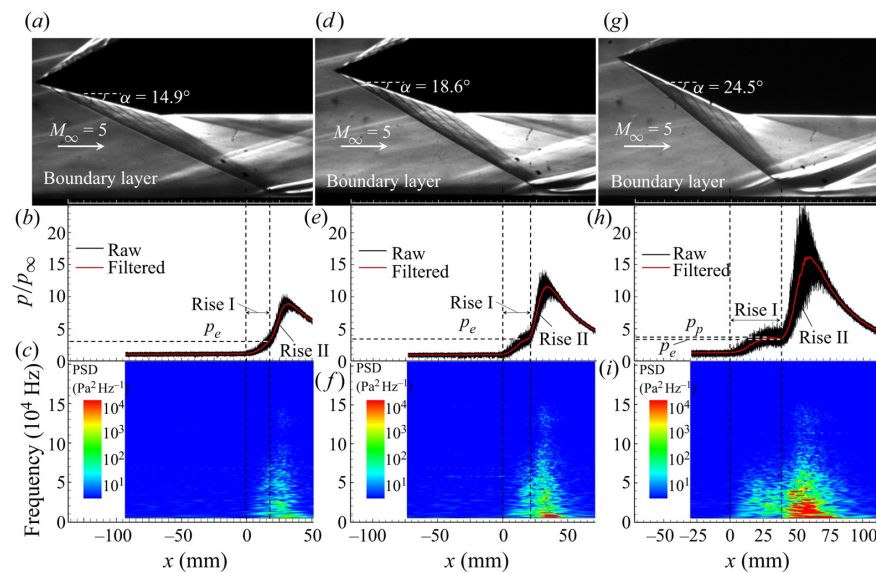
Figure 1.3: Pressure plateau region of different shock strengths over a turbulent boundary layer at Mach 5 (Xue et al., 2023).
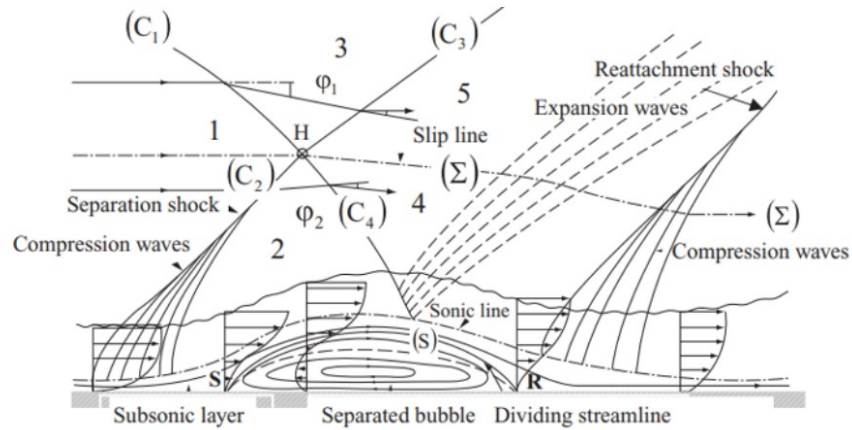
Figure 1.4: A schematic of a typical separation bubble in an SBLI, highlighting the important features of the interaction (Délery and Dussauge, 2009).

Figure 1.4 shows a typical separated region in an SBLI. As a result of this separated region, the boundary layer thickens and acts similar to a fluidic ramp, forcing flow just outer flow to turn away from the surface. However, since this is not a fixed, abrupt change in flow direction like a compression ramp, the flow turns more gradually due to the thickening of the boundary layer, then separates more suddenly. This causes the flow to go through a series of smaller shocks that coalesce into a separation shock away from the surface rather than at the at the surface. This part of the interaction creates an initial influence of the shock through a pressure rise on the surface of the SBLI upstream of where the inviscid shock location would be on the surface, and slightly upstream of the separation region. As flow further moves downstream, an expansion fan forms near the peak of the separation bubble as the flow now has room to turn back towards the surface and accelerates behind the separation region. The flow then goes through a final turn as it is forced to return to parallel with the SBLI surface and crosses a series of shocks similar to the separation shock to form the reattachment shock. Looking at the pressure distribution on the surface of this interaction Figure 1.2, the pressure plateaus just after separation and begins to rise again upstream of reattachment. Due to the thicker region of subsonic flow near reattachment compared to separation, pressure does not plateau across the entire separation bubble. A larger subsonic area causes a second pressure rise just upstream of the reattachment location of the boundary layer. All this shows that without particle imaging velocimetry (PIV) or some form of 3-D flow visualization, it can be very difficult to determine exactly where the separation bubble begins and ends, but its location can be estimated with reasonable accuracy from other tools such as oil flow visualization (skin friction direction visualization) and heat flux measurements. Likewise, the pressure plateau is a good indicator of separation as shown in Figure 1.2 but has not been proven to be true of all cases. Lee and Gross (2022) showed in a numerical study that a flow that experiences separation does not always see this pressure plateau. So, a lack of the pressure plateau is not always an indicator that the flow did not separate.

Other work by Hayashi and Aso (1986) and Hayashi et al. (1986) study heat flux measurements on these 2-D SBLI. Hayashi et al. used thin film heat gauges to measure the heat flux of impinging oblique shocks at varying shock strengths to study the effects of separation on surface heating. Figure 1.5 shows a comparison of the heat flux and pressure distributions for these interactions and notes the important aspects of the flow for each case. Highlighting the bottom right figure, the important aspects of the flow are noted by the first local heat flux minima (1), flow separation (2), a second local heat flux minima (3), and the effects from the expansion fan (4). On the other three graphs, points C, D, and E represent the local minima (or just the maximum gradient for point C which has no second local minima) similar to point (3) on bottom right figure. As the strength of the shock increases, this local minima becomes stronger, and can therefore be used to validate the mean strength of the interaction.

The first local feature in the heat flux measurements is a local minima. This phenomena occurs in both separated and attached flow, and correlates to the initial pressure rise. This was the first observation that the heat flux begins to drop before the shock wave enters the boundary layer. The adverse pressure gradient from the shock wave causes the velocity gradient in the boundary layer to reduce near the surface. As a result, the skin friction at that location is also decreased which has less heat flux to the surface. This local minima of heat flux is very close to the initial pressure rise, and this local minima aligns well with the location of the initial pressure rise.

The second feature is the local peak heat flux between the two minima and occurs at the onset of separation. Following this point, the flow in the separation bubble has lower skin friction and reduced heat flux which results in a second heat flux minima.

While not noted on these figures, there is a slight decrease in the slope of the heat flux between points 3 and 4, and this point correlates with the reattachment point of the separated region. After the separation region, the heat flux continues to rise. This is a result of the expansion fan at the top of the separation bubble which direct the flow towards the surface and increase skin friction in that region. The final point on this chart is due to the expansion fan, but this is not as relevant to the present study.

Humble et al. (2007) studied impinging, oblique SBLI using PIV to characterize the mean flow properties of the separated region and the unsteady properties of the interaction. Humble et al. found that instantaneous measurements of the SBLI region show significant reverse flow, but this was not observed in mean. Thus, high-frequency measurements could be required to show separation in certain incipient cases.

1.2   3-D Interactions

While these 2-D interactions have been extensively studied, much less work has been done in SBLI that add sweep to the shock in the x-z plane. This sweep introduces additional complexity through three-dimensional (3-D) effects added from a spanwise flow component not found in 2-D interactions, as well as additional unsteady effects (Threadgill and Little, 2020; Lee and Gross, 2022). These are particularly important for

20
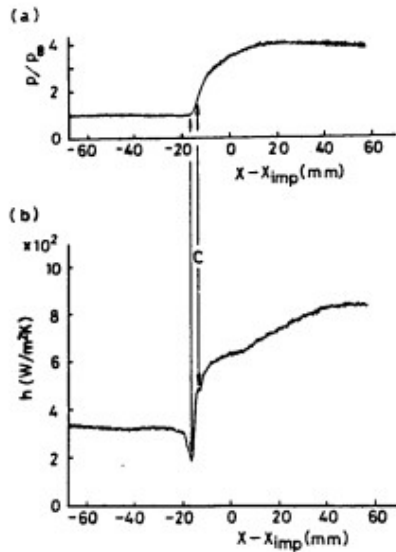
Figure 10. At the incident shock
angle 19.2°
(a) pressure distribution (b) heat-
transfer coefficient distribution
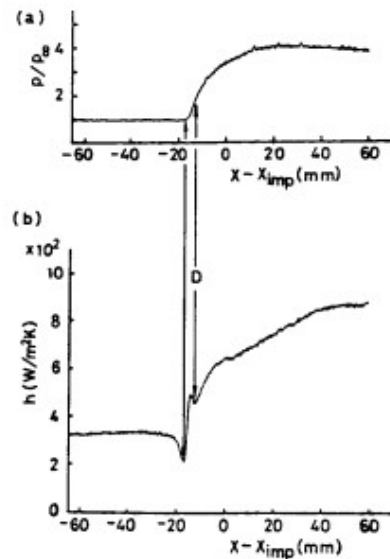
Figure 11. At the incident shock
angle 20.2 (case 1)°
(a) pressure distribution (b) heat-
transfer coefficient distribution
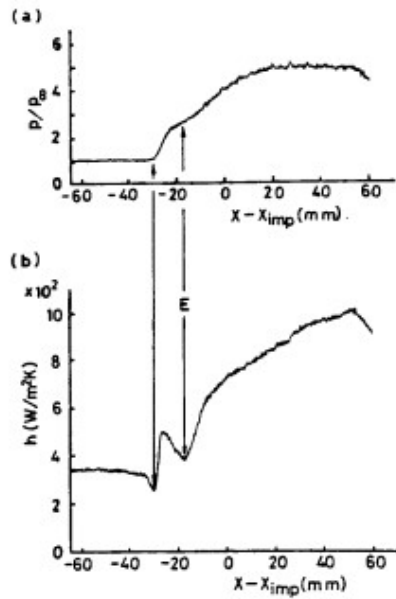
Figure 12. At the incident shock
angle 20.2° (case 2)
(a) pressure distribution (b) heat-
transfer coefficient distribution
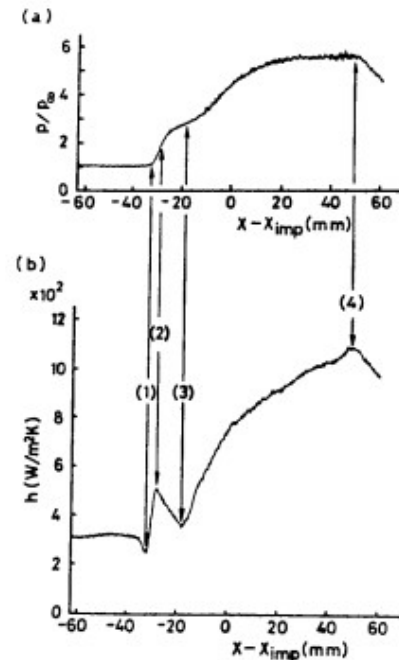
Figure 13. At the incident shock angle
22.1°
(a) pressure distribution (b) heat-
transfer coefficient distribution

Figure 1.5: Comparison of pressure measurements and heat flux measurements across 2-D impinging oblique SBLI at varying shock strengths Hayashi et al. (1986).
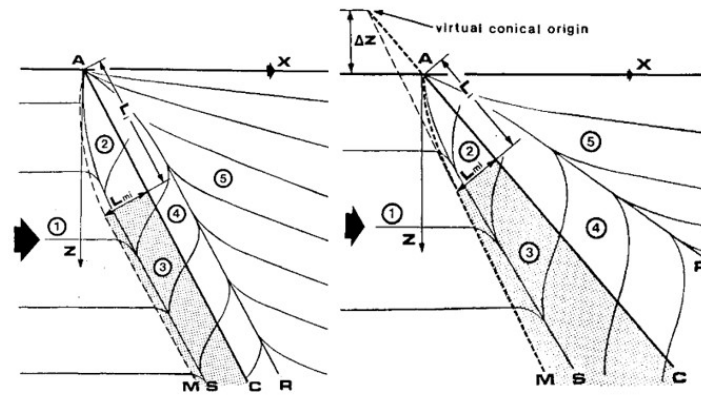
Figure 1.6: Schematic of cylindrical SBLI (left) and conical SBLI (right) with surface streak lines (Settles and Teng, 1984).

applications such as supersonic air-breathing engine inlets, control surfaces, and propulsion systems to name a few (Threadgill and Little, 2020; Settles and Teng, 1984).

Initial investigations of 3-D SBLIs were performed by Stalker (1957) in the late 1950's with a fin mounted perpendicular to a flat plate, and more detailed studies followed these into the 1970's and 1980's. These works investigated the effect of sweep on swept compression ramps (McCabe, 1966), swept shocks induced by a fin normal to the surface (Goldberg, 1973), and the effect of Mach number on the separation region with turbulent boundary layers (Dolling, 1984). These investigations also set out to determine how to scale the separation size of 3-D separation bubbles. Another study by Korkegi (1973) found that the deflection angle for the incipient separation for low Mach numbers ($M < 2$) is inversely proportional to the incoming Mach number, whereas in higher Mach flows the incipient separation is independent of Mach number. Later work by Goldberg (1973) and Dolling (1984) agreed with these results, studying separation ranging from Mach 2 to Mach 6, and found the incipient separation to be independent of Mach number.

A final important flow feature to discuss in 3-D separation bubbles is cylindrical versus conical similarity. 2-D separation is typically scaled with the height of the incoming boundary layer, but most 3-D separation bubbles grow canonically in the spanwise direction from a virtual conical origin (VCO) (see Figure 1.6). The shock wave reduces the velocity in the x-direction but does not affect the velocity of the flow in the spanwise direction. Thus, the sweep angle downstream of the interaction is larger than the sweep angle upstream of the interaction which creates this conical trait of the separation region (Lee and Gross, 2022). This change in the separation length along the span makes it difficult to scale the entire interaction with a single length scale for these conical separation cases. The distinction between conical and cylindrical separation is clear in theory, but it is much more difficult to characterize in real studies due to the difficulty in determining the separation and reattachment locations.
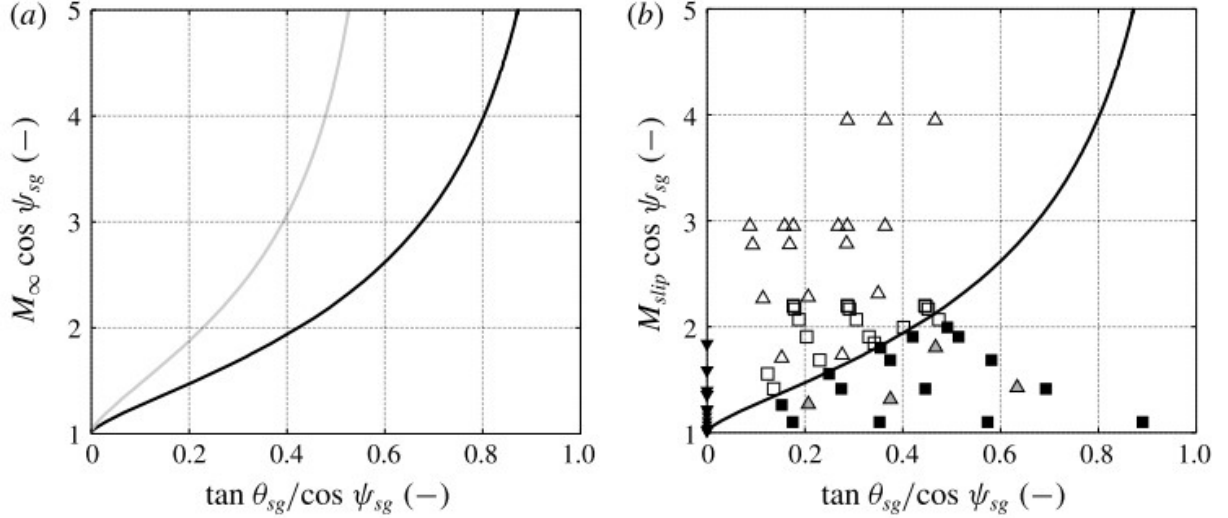
Figure 1.7: Theoretical threshold for cylindrical and conical separation for impinging shocks (black line) and reflected shocks (gray line). Values above and to the left of each line are predicted be cylindrical. Filled in markers are reported as conical, and open markers are reported as cylindrical (Threadgill and Little, 2020).

While the concept of cylindrical and conical separation had been noted before, no explanations were given as to why these interactions required further scaling until Settles and Teng (1984) attempted to model what conditions caused separation to behave conically, and conversely what conditions cause the interactions to behave cylindrically. This was achieved using a range swept compression ramps in Mach 2.95 flow. Settles and Teng (1984) studied attached and detached shocks of swept compression ramps. An attached shock refers to a shock that occurs close to the tip of the compression ramp, whereas a detached shock will form a normal shock in front of the tip of the compression ramp before turning into an oblique shock. Settles and Teng (1984) theorized that separation will exhibit cylindrical behavior for attached shocks and conical behavior for detached shocks and supported these hypotheses with the experimental studies of the swept compression ramps. Figure 1.7a shows the relationship Settles and Teng determined for predicting cylindrical and conical separation for impinging and reflected shocks. This relationship is modeled using an effective Mach number near the wall that approximates the boundary between the viscous and inviscid rotational domains of the boundary layer. This is defined as M_{slip}, but the precise location of this line is difficult to predict and is dependent upon the pressure rise across the shock, the upstream boundary layer conditions, and the ratio of shear velocities across the shock foot (Rosen et al., 1980). Figure 1.7b shows a collection of work done that was labeled as cylindrical or conical, and how the theoretical threshold reasonably predicts cylindrical or conical similarity, but is still flawed and requires further work to determine the true solution of this threshold.

However, recent studies (Padmanabhan et al., 2022; Vitols, 2024) have produced inconsistent results with these findings to suggest this is not the case. Other work by Vanstone et al. (2018) has postulated that due to the limited scale of most supersonic wind tunnels, interactions classified as cylindrical may have only been

classified as such because they were measured in the inception region. Vanstone et al. argues 3-D interactions can have a truly cylindrical interaction, and further theorizes that the inception region of weakly separated flows is very long, and thus has not developed into a cylindrical interaction in the limited span of the test section.

The previously mentioned studies, and more recent studies, done on swept SBLI offer relevant results using a compression ramp on the SBLI surface (Settles and Kimmel, 1986; Lu et al., 1990; Alvi and Settles, 1992; Settles et al., 1986; Erengil and Dolling, 1993), but few studies from the literature focus on SBLI from impinging oblique shocks (Holden, 1984). A renewed interest in sustained high-speed flight has highlighted the necessity to improve air-breathing inlets and isolators, and thus has driven recent efforts to better understand 3-D SBLI from impinging oblique shocks (Gross et al., 2018; Threadgill et al., 2017). Hainsworth et al. (2014) and Dawson et al. (2015) studied a swept impinging oblique shock using particle image velocimetry at different sweep angles and found that more swept cases exhibited conical separation. However, this work did not study the effect of caused by maintaining constant pressure rise across the shock. Only recently has this effect been studied. Doehrmann (2018) further studied this work and studied these swept impinging shocks at sweep angles of $\psi = 0°, 15°, 22.5°, 30°$, and $40°$. Doehrmann, Dawson et al., and Hainsworth et al. all found that sweep cases under $22.5°$ exhibit cylindrical separation behavior, and the higher sweep cases exhibit conical separation. However, these works were flawed in that PIV was only taken in one plane which provided insufficient data to make these conclusions. More recent work related to this by Threadgill et al. (2017) found that the interaction for each sweep case exhibits conical separation for the same conditions. Recent work by Ceci et al. (2023) and Ceci et al. (2024) introduce a spanwise component of flow to the numerical study to observe swept SBLI in the hypersonic regime. Ceci et al. found that the Free Interaction Theory holds true for the hypersonic swept interaction, but only in the initial part of the interaction region. They also conclude that hypersonic interaction exhibit the same characteristic interaction traits as supersonic interactions, further supporting a Mach independence of the interaction. Other relevant work by Zuo et al. (2023) are conducted to investigate the fluid-structure interaction of swept SBLI, and work by Dooner et al. (2024) is conducted to study a new model to create more complex loading on the SBLI surface to study the fluid-structure interaction.

Padmanabhan et al. (2021b, 2022); Padmanabhan (2023); Lee and Gross (2022); Vitols (2024) have attempted to isolate the effect of sweep on these interactions. Lee and Gross found that the separation point moves upstream and the reattachment point moves downstream with increasing sweep angle, suggesting that the separation region becomes larger with increasing sweep. Padmanabhan was able to show that in Mach 2.3 flow for lower sweep angles ($\psi = 15°$) and a weak pressure rise, separation and reattachment lines asymptotically approach a constant value. This study looked at the pressure rise across the shock (C_p), and it shows that the interaction exhibits cylindrical separation behavior. This suggests that given enough span, weakly separated flow can become cylindrically separated and not stay a conically separated flow across the span of the interaction. Padmanabhan gave numerical and experimental evidence that supported

quasi-conical similarity between interactions occurring in separated flows with higher sweep angles. Results from Padmanabhan (2023) are consistent with the hypothesis produced by Threadgill and Little (2020) in determining cylindrical versus conical separation. Further work by Vitols (2024) attempted to better isolate sweep by using the pressure rise normal to the shock (C_{p_n}, this is further discussed in section 2.3) as proposed by Threadgill and Little (2020), rather than just C_p as was studied in earlier works. Results by Vitols were consistent with Padmanabhan findings, but showed that with a 40° sweep, with his configuration, there were no signs of separation when C_{p_n} was held constant between shock generator configurations. Comparing cases with C_{p_n} was sufficient at collapsing results across many sweeps to common results over the entire interaction, but requires further analysis to determine if these results can be collapsed across different pressure rise values or different tunnel configurations.

The most commonly compared configurations of these swept SBLI are swept compression ramps and swept reflected shocks. This comparison is important because reflected shocks have sidewall effects in which the viscous effects near the wall cause the shock near the wall to be more of a normal shock that gradually becomes a swept shock. Further influence of the interaction by the root and tip effects of the shock generator for reflected shocks must also be taken into consideration due to the expansion of the flow around the model. Each of these makes the quasi-infinite region for an impinging reflected shock small, and it can be difficult to achieve a quasi-infinite region in smaller wind tunnels. Some examples of comparisons of impinging reflected shock SBLI and compression ramp SBLI are work by Threadgill and Little (2020) in which work by Settles and Teng (1984), Alvi and Settles (1992), and Settles and Kimmel (1986) that consist of swept compression ramp and swept impinging shock SBLI are compared. In these works, this comparison is used to show that the interaction length can scale in a similar manner as each other (although exactly how they scale is not fully understood).

As Vanstone et al. has proposed, due to the small size of most university-scale supersonic wind tunnels, sidewall and shock generator tip effects make the quasi-infinite region small. If these effects were to cover too much of the interaction, or have effects on this region of interest, then much of this data could be missing large parts of the interaction – particularly in determining cylindrical or conical interactions. This suggests the need for further verification with a larger quasi-infinite region. This can be achieved by bringing the leading edge of the shock generator closer to the boundary layer surface, making the shock generator span further in the z-direction, or increasing the size of the wind tunnel. Of course, increasing the span of the shock generator is often impossible due to tunnel limitations, and increasing the span of the tunnel is impossible unless using a different facility. The next option to bring the shock generator closer to the surface could be the best option, but supersonic wind tunnels go through a "startup" period when air is first sent through the test section in which the flow is not yet supersonic. This phenomenon is a function of the frontal area of the object in the tunnel and the total area of the test section. If the shock generator spans the entire length of the tunnel, the frontal area could be too large for the flow to start. Likewise, if the shock generator is too close to the boundary layer surface, the flow is choked between these surfaces and is unable to start

in that region. Along with the choked flow, should the shock generator be too close to the surface, optical access could become much more difficult for the SBLI surface. Lastly, increasing the size of the wind tunnel makes the quasi-infinite region larger, but does not increase the scale of the separated region when compared to the span of the interaction. The way to measure this is called the aspect ratio, and it is defined as the length of the shock generator divided by the height of the leading edge of the shock generator to the SBLI surface. Alone, each of these options to increase aspect ratio produce their own challenges and drawbacks, so it is best to find some combination of the three to increase aspect ratio while maintaining tunnel operability. This presents the unique issue that other swept SBLI configurations have less of a concern with of creating a high aspect ratio to increase the interaction length, mitigate the sidewall effects and shock generator tip effects, and while also allowing the tunnel to start.

The present investigation focuses on a turbulent boundary layer over a flat plate with a swept impinging oblique shock. The goal of this work is to determine what flow characteristics influence the mean flow topology of these swept SBLI at a range of different conditions by varying Reynolds number, Mach number, normal pressure rise, and sweep angle. This will provide insight into what conditions have the greatest effect on the mean interaction characteristics, and what conditions of the incoming flow have less of an impact on the interaction. This is accomplished using three techniques to study the surface of the SBLI: Infrared Thermography (IR) to study the heat transfer, oil flow visualization to study the skin friction direction, and mean pressure measurements. Coupled together, these measurements are used to characterize the mean flow patterns for the SBLI surface across several shock generator configurations. Other goals of this work are to compare these results to similar experiments done by Vitols (2024) in a smaller aspect ratio wind tunnel at the University of Arizona to assess if increasing aspect ratio yields similar results. Showing similar cases run in different wind tunnels can help determine an appropriate scaling factor on the interaction as well as further verifying that the quasi-infinite region in the smaller tunnel is large enough to be confident that the data taken from it is not affected by the sidewalls or the tip of the shock generator.

Chapter 2

Experimental Setup

2.1   Overview

Experiments were conducted at the University of Arizona using the Arizona Polysonic Wind Tunnel (APWT), and supporting work has also been conducted at the University of Arizona using the Indraft Supersonic Wind Tunnel (ISWT). This investigation focuses on a swept impinging oblique SBLI (as seen in Figure 2.1) using a range of shock generator and wind tunnel configurations to collect a matrix of data that isolates different flow features in attempts to determine what drives the mean flow topology of the SBLI. Furthermore, a comparison of the data taken from both tunnels is made to compare and validate the findings from each. A shock generator is mounted to the sidewall of each tunnel with a window opposite the shock generator for optical access for each case.

To characterize the SBLI, mean pressure measurements, oil flow visualization, and IR thermography were used. Additionally, with APWT being a relatively new facility at the University of Arizona, it is an important step to characterize the boundary layer that occurs on the SBLI surface. This section will introduce the wind tunnels used in this work, discuss each method used in APWT to characterize the flow, and go over the instruments used with the associated error with each instrument. Table 2.1 shows the final test matrix of the tests completed in APWT.

2.2   APWT

The remainder of this section will discuss the setup and experiments conducted in the Arizona Polysonic Wind Tunnel (APWT). APWT is a blowdown tunnel that was originally built and operated in the 1950's and has been recently acquired by the University of Arizona. The tunnel has subsonic, transonic, supersonic, and

Table 2.1: APWT Test Matrix

M_∞	2.1		3.0		
ψ	20	40	20		40
C_{p_n}	0.6	0.6	0.4	0.6	0.6
Oil	✓	✓			
Mean Pressure	✓	✓	✓*	✓	✓
IR	✓	✓	✓	✓	✓

*Mean pressure data for this case is more course than other cases.

26
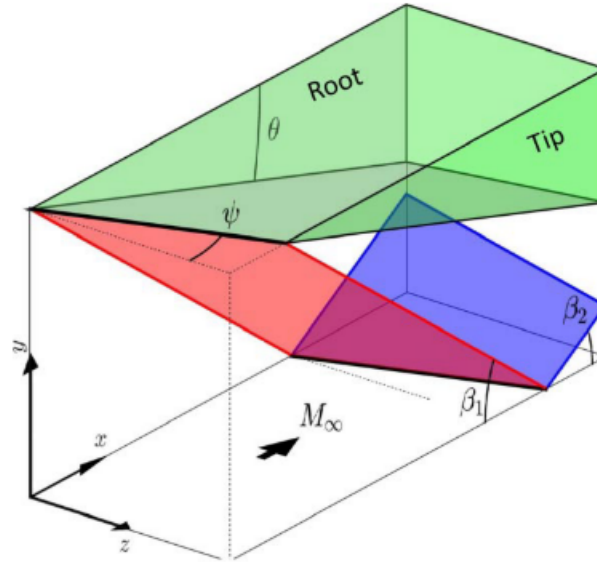
Figure 2.1: Schematic of a swept impinging shock with relevant angles (Threadgill and Little, 2020).

Table 2.2: Boundary Layer Characterization of APWT and ISWT.

Tunnel	M_∞ [-]	$u_\infty [\frac{m}{s}]$	δ [mm]	δ^* [mm]	θ [mm]	H [-]	C_f [-]	$Re_\infty/L\ [\frac{1}{m}]$
APWT	2.07	516	15.25	5.58	1.01	5.50 (1.3)	3×10^{-3}	2.80×10^7
APWT	2.07	518	15.25	5.62	1.02	5.51 (1.3)	3×10^{-3}	4.24×10^7
ISWT	2.28	554.8	6.53	2.03	0.56	3.66 (1.39)	2.00×10^{-3}	9.99×10^6

Figure 2.2: Image of Arizona Polysonic Wind Tunnel (APWT).

hypersonic capabilities and is run with high pressure air blown through the test section down to atmospheric conditions. Large pressure tanks hold 1200 cubic feet of filtered, unheated air held at 2000 psig to give an approximate total run time of 2 minutes per day. However, the actual total run time is dependent on the Mach number and number of runs done per day. Lower Mach numbers have higher mass flow rates (for supersonic flows), and each time the tunnel is stopped and started again, some air is lost in the flow starting and unstarting process just before and after the test respectively.

APWT has a nominally square test section of 15" × 15" × 52" (W × H × L) with visual access via a 14.5" diameter window on either side. Interchangeable nozzles allow for a variable Mach number that range from 1.75-4 with plans to extend this range in the future, but this investigation focuses only on Mach 2.1 and 3. Modification to new and existing floor and ceiling parts allow for the SBLI surface parts to be interchangeable as well. However, while the ceiling and floor panels are interchangeable, all tests conducted in APWT were done on the ceiling. This eliminates any error that could be associated with differences in incoming flow properties or boundary layers on the floor compared to the ceiling. The tunnel ceiling is made of a steel plate that was cut to house a plug that sits flush with the surface. The shock generators were positioned such that this plug is the SBLI surface for all cases, and different plugs were installed for each different type of test. An explanation of each of these will be further explained later in this section.

While ISWT has constant total conditions, APWT is faced with the challenge of maintaining constant conditions in the settling chamber as seen in Figure 2.3 and Figure 2.2. This is accomplished via a PID controller, two pressure transducers in the settling chamber, and two hydraulic valves (combined Cv=366) that throttles the flow ahead of the settling chamber. As the pressure in the tanks that hold the air drops, the valves controlled by the PID controller open more to make the pressure in the settling chamber constant
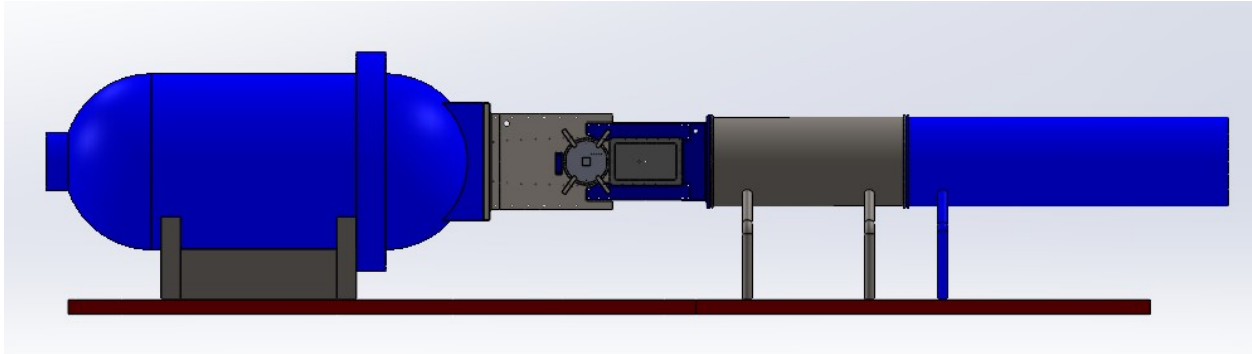
Figure 2.3: Schematic of Arizona Polysonic Wind Tunnel (APWT) settling chamber (left), test section (middle), and diffuser (right).

(a) Total Temperature
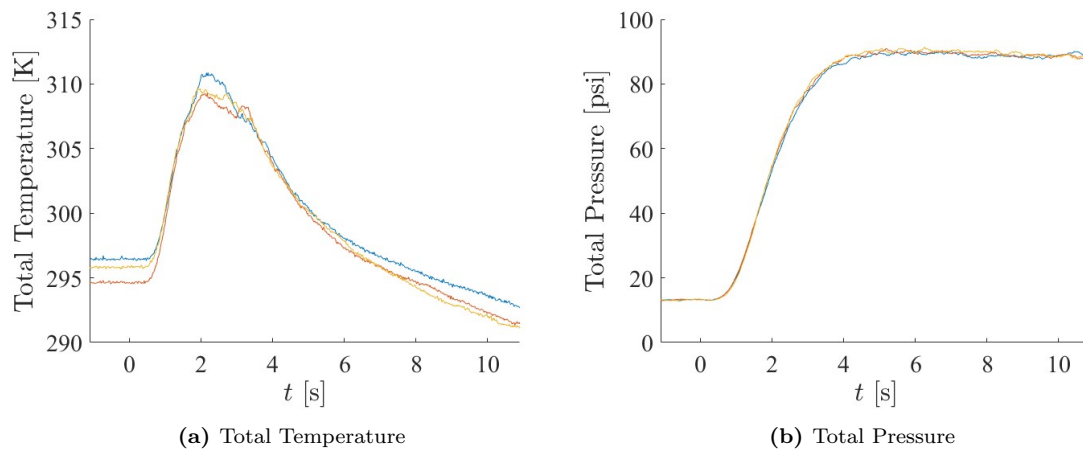
(b) Total Pressure

Figure 2.4: Example of total pressure and temperature during three runs at Mach 3.0.
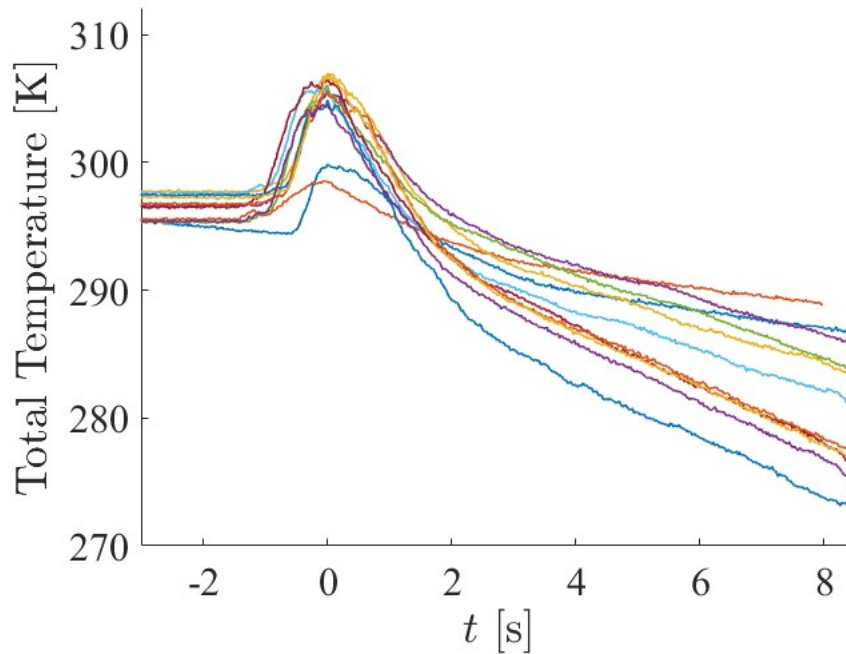
Figure 2.5: Total temperature for several runs at Mach 2.1 after tests for this thesis were completed.

during the run. This provides a relatively constant total pressure, but is not perfectly constant during each run and it adds variability between runs. In addition to this, the total temperature drops during the run and could be an additional source of error. A plot of the settling chamber temperature and pressure during a run is shown in Figure 2.4. Each of these conditions are measured and stored during the run to be accounted for when processing results, but early work conducted at Mach 2.1 does not have total temperature data. The data is estimated by using other Mach 2.1 runs taken after these tests which adds another margin of error compared to Mach 3.0 tests. Figure 2.5 shows a plot of total temperature in several Mach 2.1 runs conducted in different experiments in APWT once the total temperature was able to be measured. The model to estimate the total temperature for runs conducted for this thesis was made based off these temperature profiles, thus adding a level confidence greater than just assuming constant total temperature, but acknowledging there is variability between runs that is very difficult to account for when processing results without biasing the results to look as expected. It is for this reason that the total temperature is kept to the same estimated linear fit between all Mach 2.1 runs. However, this estimation of total temperature is not expected to have much of an effect of the results in all measurement types.

The main benefit of APWT compared to ISWT is the ability increase aspect ratio. To determine the aspect ratio for these tests, it is best to get the highest aspect ratio possible while still allowing the flow to become supersonic. This ensures the SBLI has enough spanwise distance to fully develop and prevents sidewall influences from affecting the region of interest. The aspect ratio is defined as the shock generator
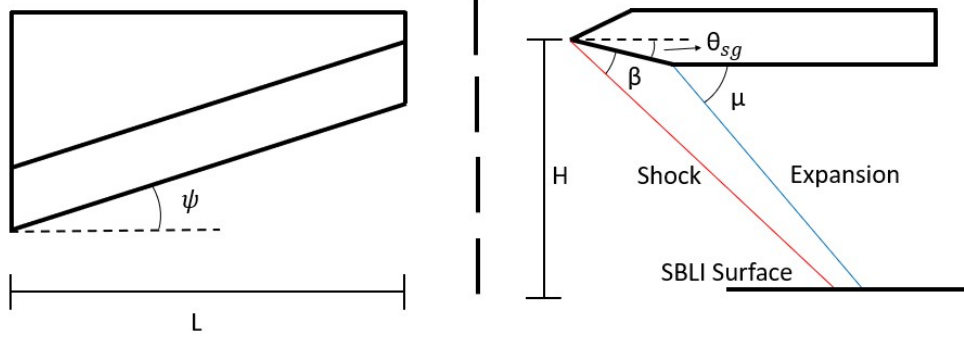
Figure 2.6: Schematic of aspect ratio.

length over the height of the leading edge as shown in Figure 2.6. This is limited partly by tunnel constraints and partly by the startup phenomena mentioned previously.

The shock generator takes up a large percentage of the test section and acts as a second throat of the test section. If this second throat becomes too small, the model will choke the flow and prevent the tunnel from starting. Equation 2.1 shows the relation between the ratio of the second throat area and the test section area, and Mach number (Pope and Goin, 1965) where A_2^* is the second-throat area, A_T is the test section area, M_1 is the freestream Mach number, and M_2 is the Mach number behind the normal shock upstream of the second throat and is defined by Equation 2.2. These equations are derived using isentropic and normal shock relations, and they assume the Mach number is equal to one at the second throat to give the maximum theoretical area ratio of the second throat and the test section. The ratio of the second throat area and the test section area can be found with simple geometry, and this value should not exceed the results from Equation 2.1 at any given Mach number.

The aspect ratio for the shock generators used in these experiments was found for Mach 2.1 set at 2.75. However, this was found with a few assumptions. Firstly, the momentum thickness is required to determine the second throat area and the area of the test section. The determination of the area ratio was done prior to the boundary layer being characterized, and the momentum thickness was incorrectly assumed to be twice as high as the true value. Further, Equation 2.1 is known to have a low level of confidence. Due the high cost and long lead time of building these shock generators, it was important that the first shock generator allowed the flow to start. Therefore, a 10 percent margin of error was added to the height of the shock generator as well to ensure the flow would start. The length of the shock generator was chosen to be 12.5 inches, and the best height of the leading edge based on these assumptions and calculations was found to be 4.5455 inches. To ensure testing at each configuration only varied sweep, this aspect ratio was held constant for all shock generators. However, this leaves room for future testing to increase this aspect ratio by bringing the shock generator towards the SBLI surface because there is such a high safety factor on this aspect ratio value of 2.75.

$$\frac{A_2{}^*}{A_T} = \frac{M_2}{M_1}\left[\frac{1+\frac{(\gamma-1)}{2}M_2{}^2}{1+\frac{(\gamma-1)}{2}M_1{}^2}\right]^{\frac{\gamma+1}{2(\gamma-1)}} \tag{2.1}$$

$$M_2{}^2 = \frac{\frac{2}{\gamma-1}+M_1{}^2}{\frac{2\gamma M_1{}^2}{\gamma-1}-1} \tag{2.2}$$

2.3   Shock Generator Configurations

As previously mentioned, the strength of the shock is one of the primary factors that determines the characteristics of the SBLI. This strength is quantified using C_p, as shown in Equation 2.3, by utilizing the pressure rise across the reflected shock and the incoming Mach number. In Equation 2.3, if the shock is swept, C_p remains the same. This could lead to inconsistencies between sweep cases as M_∞ is entering the SBLI at a different direction relative to the normal of the interaction, and thus the Mach number normal to the shock in changing with sweep which changes the interaction strength if the impinging angle is not changed. In an attempt to isolate the effect of sweep, C_p is modified as proposed by Threadgill and Little (2020) to C_{p_n} and is used to characterize the strength of the interaction normal to the shock rather than just in the freestream direction as C_p is. Equation 2.4 shows that is similar to C_p, but M_∞ is replaced with $M_\infty cos(\theta)$ as the flow direction relative to the interaction is proposed to be the important factor when comparing cases with different sweep angles.

$$C_p = \frac{2}{\gamma M_\infty{}^2}\left(\frac{p}{p_\infty}-1\right) \tag{2.3}$$

$$C_{p_n} = \frac{2}{\gamma M_\infty{}^2 cos^2\psi}\left(\frac{p}{p_\infty}-1\right) \tag{2.4}$$

Ideally, a full test matrix to study this theory is conducted to capture many different sweep conditions, C_{p_n} values, and Mach numbers. This work marks the beginning of a test matrix that supports similar work done in ISWT which has a lower aspect ratio. These conditions are met with shock generators mounted to the wall of the wind tunnel as shown in Figure 2.7. In this figure, flow goes from left to right, and the SBLI surface is the plug below the shock generator. Each shock generator is mounted such that the shock lands in the same location on the plug, but one further case was able to be conducted by placing the $\psi = 20°$ shock generator designed for Mach 2.1 in Mach 3.0 flow. This allowed for a test that varied in C_{p_n} without fabricating a new shock generator. A full test matrix of the flow conditions met in these experiments is shown in Table 2.1.

A schematic of the shock generators designed for these experiments are shown Figure 2.6. Further, a model of a shock generator made for these experiments is shown in Figure 2.8. In Figure 2.8, the five larger holes are threaded holes for 1/2 inch diameter bolts used to hold the shock generator to the tunnel wall,
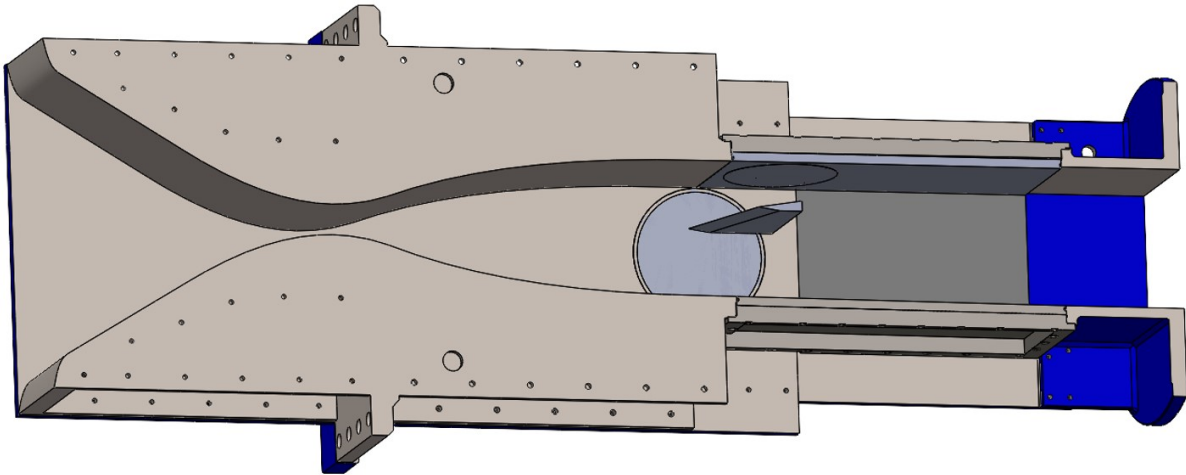
Figure 2.7: Schematic of shock generator set up in APWT test section.

and the two smaller holes are for $1/4$ inch diameter dowel pins that ensure precise placement of the shock generator. As seen in Figure 2.6, θ_{sg} represents the angle at which the freestream air is deflected in the x-y plane and ψ is the sweep angle of the shock. Two important aspects of this are the shock angle and the expansion fan, both of which are based on the angle of θ_{sg} and ψ. The shock angle and expansion fan angle are found using the θ-β-M relation to find the shock angle where M is the component of the Mach number normal to the sweep angle (M_n), and θ is the angle of the shock generator normal to the sweep angle (θ_n) of the shock generator. The angle of the first part of the expansion fan off the rear side of the compression ramp of the shock generator is found using the Prandtl-Meyer equation using the Mach number component normal to the sweep angle. These equations are shown in Equation 2.5 and Equation 2.6 for the θ-β-M relation and the Prandtl-Meyer expansion fan respectively. In these equations, the subscript n represents the normal direction to the sweep angle.

As depicted in Figure 2.6, the initial wave of the expansion fan is at a steeper angle compared to the shock angle, and thus the length of the compression ramp portion of the shock generator is designed to be long enough such that the expansion fan lands far enough downstream of the shock as to not interfere with the SBLI. Wu et al. (2024) studied the effect the expansion fan has on an SBLI in a hypersonic inlet of an air-breathing propulsion system, and found that the effect of the expansion fan did not prevent the SBLI from separating, but did prevent the pressure from reaching the full pressure rise value after the shock compared to the same pressure rise with no expansion fan. There are a few differences of these experiments compared to the work done for this thesis, namely that Wu et al. worked on 2-D interactions in hypersonic flow. Little work has been done on the effect the expansion fan has on the SBLI, so it is best practice make the expansion fan further downstream to prevent any unknown effects of this on the interaction until the effect of the expansion fan on the SBLI is better understood.
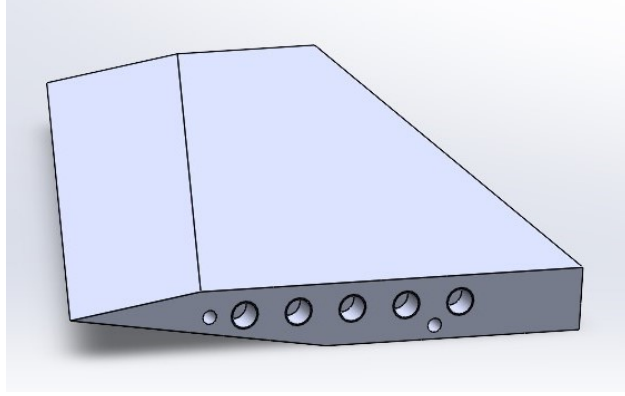
Figure 2.8: Model of shock generator designed for APWT.

$$\tan(\theta_n) = \cot \beta_n \frac{M_{1n}^2 \sin^2(\beta_n) - 1}{M_{1n}^2(\gamma + \cos(2\beta_n)) + 2} \tag{2.5}$$

$$\mu_{1n} = \arcsin\left(\frac{1}{M_{1n}}\right) \tag{2.6}$$

The shock generators were fabricated at the University of Arizona with a precision of the θ_{sg} of $\pm 0.1°$. The shock generators are bolted to an aluminum blank in place of one of the windows and clamped tightly to prevent any shifting during the run. To ensure the shock generator is level with the SBLI surface, an electronic level is placed on the SBLI surface (ceiling) and tared. However, the ceiling of the tunnel diverges slightly to account for the growth of the boundary layer along the x-direction, and this was not taken into account when determining the angle the shock generator was placed at in relation to the freestream. The shock generator is then adjusted within a precision of $0° \pm 0.1°$. This leaves a combined associated error in the defined θ_{sg} of up to $0.2°$ based on the precision of the machined surface and the accuracy the shock generator is mounted. This error equates to around a $\pm$ 0.015 change in the C_{p_n}, and is not considered a major source of error.

2.4   Boundary Layer Characterization

As of the time of writing this thesis, APWT has been operational at the University of Arizona for only a few years, and minimal work up until this point has been completed to characterize the flow in the tunnel since being installed. Determining a boundary layer profile is important in determining whether the boundary layer is laminar or turbulent and relevant aspects such as the boundary layer height, momentum thickness, and displacement thickness. Besides verifying freestream conditions and boundary layer properties, it is often relevant to scale SBLIs based on these boundary layer properties. Thus, to accurately attempt to characterize this interaction, an important step is to determine the boundary layer profile.

Figure 2.9: Boundary layer rake installed in APWT.

The freestream velocity and boundary layer profile for the Mach 2.1 nozzle pair has been determined using pressure transducers equipped in the tunnel and a boundary layer rake equipped with 12 Pitot probes mounted to the SBLI surface as shown in Figure 2.9. Pressure in the settling chamber (p_0) is measured with two fast-response PX409 Omega pressure transducers rated from 0-1000 psi (absolute). The associated error with each transducer is ±0.08%, which equates to 0.8 psi and is not considered a major source of error in this discussion (refer to Figure 2.4 to see the noise of the pressure measured in the settling chamber). The Pitot probes collect mean pressure data through a Scanivalve DSA pressure scanner with a sensor range of 100 psi and an advertised 0.05% error associated with the unit. However, the pressure read by the DSA is a slow-response system that was recorded at 50 Hz through approximately 20 feet of tubing. The longer tubing in this case presents some level of error as it takes time for the information to travel along to tubing to the DSA unit. This is important to note because Mach number is calculated by using the data measured from the probes and the total pressure measured in the settling chamber. This "lag" from the measured pressure at the end of the Pitot tube to the DSA unit is small, and because the pressures from each probe are averaged over time, it this is not considered a major source of error in this section. Lastly, the pressure in the freestream (p_1) is measured using two fast-response PX409 Omega pressure transducers rated from 0-750 psi (absolute) with an associated error of ±0.08%.

Accurately measuring the boundary layer profile is difficult to do when measuring with Pitot tubes. The Pitot rake used to determine the boundary layer profile consists of 12 probes with spacers placed beneath the rake to adjust the height of the probes in relation to the tunnel walls, thus allowing for a more refined profile of points. However, even though the Pitot tubes are very small, the measured pressure is an average pressure of over the frontal area of the tube. In areas of high pressure gradients (near the wall), this can skew the results as some information is lost due to the size of the instrumentation. Further, it is very difficult to

get the probe close enough to the surface to measure the lower section of the boundary layer profile. So, to get an entire profile from this method, it is necessary to fit a profile to data collected.

The first step in modeling a fit to the velocity profile is to find the velocity at the locations of the Pitot probes. This is done by using the Rayleigh Pitot formula. The freestream pressure measured in the test section and total pressure measured by the the Pitot rake (p_{02}/p_1) to get a Mach number at each probe location. To get a velocity profile, it is important to find the temperature as well. This can be estimated for a turbulent, compressible boundary layer on a flat plate by using the Crocco temperature-velocity relationship as highlighted by Fernholz and Kline (1983).

$$\frac{\bar{T}}{T_\infty} = \frac{T_w}{T_\infty} + \left[1 + r\frac{\gamma - 1}{2}M_\infty^2 - \frac{T_w}{T_\infty}\right]\frac{\bar{u}}{u_\infty} - r\frac{\gamma - 1}{2}M_\infty^2\left(\frac{\bar{u}}{u_\infty}\right)^2 \tag{2.7}$$

Here, the recovery factor (r) is found by assuming a Prandtl number of 0.72, which equates to a recovery factor of 0.896 ($r \approx Pr^{1/3}$, this value will also be further supported in section 3.3) as is commonly used for a turbulent boundary layer (Wimbrow, 1949), and the wall temperature is assumed to be at room temperature which is a reasonable assumption for short run times. Lastly, using freestream conditions taken from the upper most probes, the equation can be solved iteratively by inputting a velocity to find a temperature. This temperature can then be used to find the velocity from the known Mach number. This process is repeated until the velocity input into Equation 2.7 matches the velocity found when using the calculated temperature and known Mach number. Once a velocity profile is found, those values are used to find a fit for the boundary layer.

The boundary layer consists of three parts: the viscous sublayer which is the region closest to the wall, the log-law region which consists of the highest part of the boundary layer profile, and the buffer region which is the section between the log-law region and viscous sublayer. The upper portion of the profile is where all of the measured points from the Pitot tubes lie. Using the method highlighted by Sun and Childs (1973), a profile for the upper portion of the boundary layer is fit to the data by using the log-law relationship with the freestream Mach number and total pressure. This profile is then used along with the relationship of the law of wall for the viscous sublayer to find the lower profile of the boundary layer. Due to no data able to be collected in this region, two methods of finding the lower profile are used to increase confidence in the results for this section of the boundary layer profile. The two methods are proposed by Musker (1979) and Spalding (1970). Both methods produced nearly identical results, so only the Spalding model is utilized for the remainder of the boundary layer characterization. The results of this model and the log-law model are shown in Figure 2.10 with the associated points measured in APWT. This model provides very useful information regarding the boundary layer profile that help determine the boundary layer state that the SBLI will interact with in these experiments.

A full profile of the normalized boundary layer is shown in Figure 2.10. For the upper profile, the coefficient of determination is 0.974, showing good agreement of the profile fit to the measured data. Further, using a Van Driest transformation (Van Driest, 2003), the profile can be compared to the law of the wall theory

(a) Boundary layer model estimate

(b) Law of the wall boundary layer profile
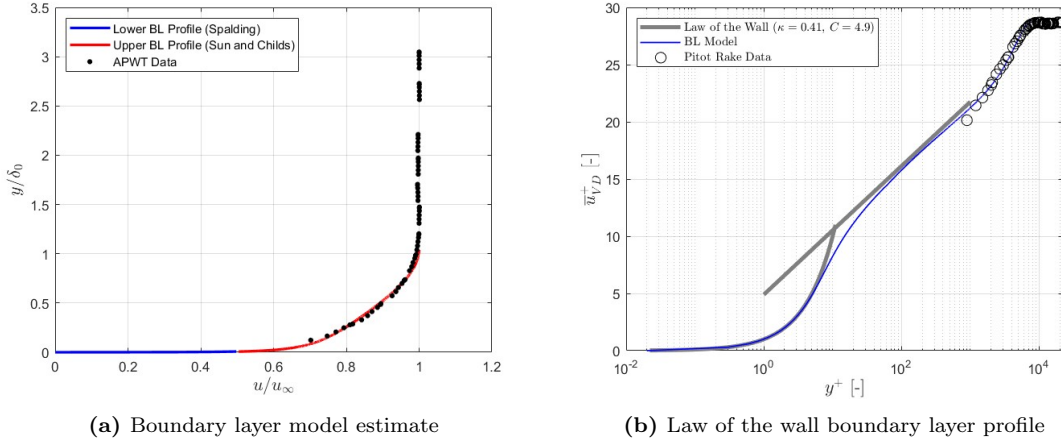
Figure 2.10: Boundary layer profile for Mach 2.1.

and shows good agreement across the entire profile. This agreement and a smooth transition from the upper portion of the profile to the lower portion of the profile further support that this model accurately represents the viscous sublayer and the buffer region.

From the models calculated, the boundary layer is determined to be fully turbulent with an incompressible shape factor of 1.3, which is common for a fully turbulent boundary layer (Schlichting, 1979). A profile was also calculated at two different Reynolds numbers: $Re/x = 2.80e7$ and $Re/x = 4.24e7$. These are the conditions all experiments run at Mach 2.1 were held at. As can be seen in Figure 2.11, the boundary layer profile of each of these cases is nearly identical, and it can be assumed that any difference seen from these two curves is within the associated error of the methods used to determine these profiles. Thus, it is assumed with minimal error that the profile from each Reynolds number case is the same. A list of notable characteristics of the boundary layer is shown in Table 2.2.

The Mach 3.0 nozzles and boundary layer profile have not yet been characterized, so the boundary layer for Mach 3.0 flow is assumed to be similar to the Mach 2 profile. Based on an assumed Mach number of exactly 3.0, the unit Reynolds number for the cases studied in these experiments is around $5e7$ depending on the total pressure and temperature which is on the same order of magnitude as the Mach 2.1 cases (lower total pressure cases of Mach 3.0 runs and higher total pressure cases of Mach 2.1 runs actually have some overlap in the unit Reynolds number). Based on this, assuming a similar profile as Mach 2.1 should produce minimal errors when comparing cases across different Mach numbers.

2.5 Mean Pressure Measurements

The first method discussed on how the SBLI is characterized is mean pressure measurements. A test matrix of the completed runs is shown in Table 2.3. This has been accomplished using and aluminum plug to sit flush with the ceiling of the tunnel. The plug is instrumented with 47 0.02" diameter holes connected to the
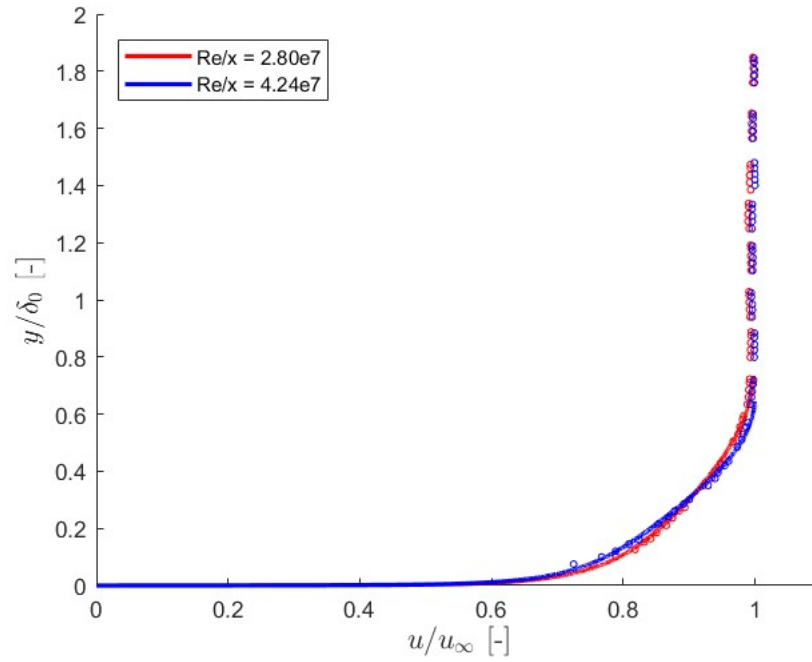
Figure 2.11: Boundary layer profile for Mach 2.1 at different Reynolds numbers.

Table 2.3: Mean Pressure Test Matrix

M_∞ [-]	2.1		3.0		
ψ [°]	20	40	20		40
p_0 [psi]	45	45	90		88
$\frac{Re}{L}^*$ $[\frac{1}{m}]$	4.05×10^7	3.96×10^7	8.40×10^7	8.31×10^7	7.93×10^7
C_{p_n} [-]	0.6	0.6	0.4	0.6	0.6
C_p [-]	0.5298	0.3521	0.3532	0.5298	0.3521
θ_{sg}	8.87°	5.47°	8.87°	11.04°	8.18°

*Reynolds numbers averaged over run due to changing total temperature.
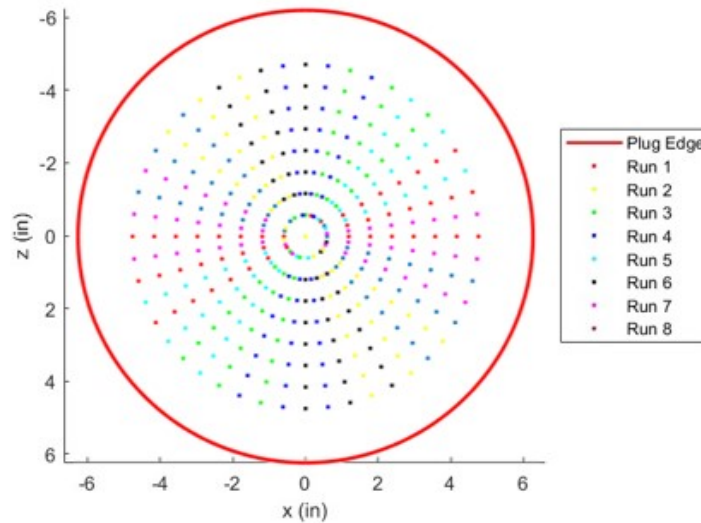
Figure 2.12: Plot of points collected for mean pressure tests. Each point represents a different pressure tap, and each color represents a different run.

previously mentioned Scanivalve unit. These holes are small enough as to not affect the flow field while also being large enough to get pressure data with assumed no lag due to the orifice sizing. The holes are arranged in three lines, each 15° apart, that go through the center of the plug. Each line consists of nine points evenly spaced apart at a diameter of 9.5", where the center point of each line is the shared center hole. The plug can be rotated in increments of 7.5°, so by running eight tests at different plug positions, a resolution of 369 total points over a 9.5" diameter circle is achieved. Due to the even spacing of the points along the radius, a fine resolution near the center of the plug is achieved at each radial point. This is beneficial because the impinging shock is designed to land in the center of the plug, so higher-pressure gradients are expected near the center. Figure 2.12 shows the data points collected with the red circle representing the edge of the plug, and each different color dot reflecting a separate run. However, while there is good resolution at each radial point near the center, there is not very good resolution along the radial direction. Due to instrumentation and run time limitations, this was the maximum number of points that could be measured in a reasonable amount of time. Further work with these run configurations would benefit from a higher resolution around the separation line as will be discussed later in the Results section.

A run was done with no shock generator to test the freestream pressure uniformity measured during the run, and Figure 2.13 shows a plot of this mean pressure data taken for two of these runs. At these constant conditions, the flow uniformity between sensors is not within the confidence of the provided accuracy as stated by Scanivalve. This pressure difference between sensors is not believed to be a major influence on the flow field due to the scale of the pressure variation among these sensors compared to the pressure rise on the surface due to the shock, but could be a possible source of error. The origin of these pressure fluctuations in the freestream is proposed to be noise from the tunnel and not poor calibration of the pressure sensors.

(a) Mean pressure measurements

(b) Locations on plug
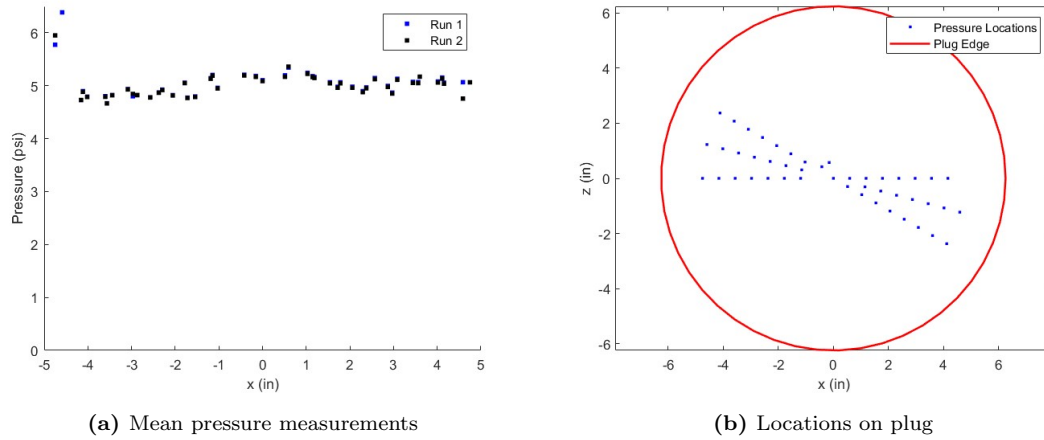
Figure 2.13: Pressure measurements from two runs of the freestream at Mach 2.1 with no shock generator (a) with the location in relation to the tunnel (b).
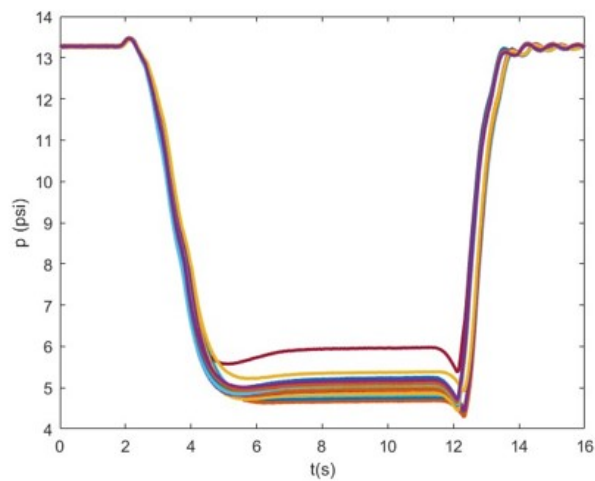
Figure 2.14: Pressure measured during entire duration of run.

To calculate the mean pressure, the pressure of the started flow is recorded for roughly 5 seconds and averaged over the run. Figure 2.14 shows an example of one of these runs, and further shows the conditions during the run remain constant. To present these pressure profiles on the surface, a grid is set in polar coordinates and data is linearly interpolated on that grid to represent the entire surface with no gaps in data. This of course leaves margin for error in that, in some places, the distance from the grid point to the nearest data point is quite far, which leaves some discrepancies in true flow physics and what the presented pressure field shows. This has an impact on the location of features on the interpolated image, and therefore must be taken into consideration when comparing pressure data to oil flow and heat flux measurements. A further complication of this interpolation is that a Gaussian kernel smoothing regression is used to smooth the data that has a lot of artificial steps due to the limited number of data points and the interpolation of data onto a grid. The kernel smoothing helps remove these artificial steps, but in the process also smooths over some real flow features if the smoothing is too high. Figure 2.15 shows how different regression values affect the visualization of the pressure field, with a value of 0 being no smoothing and 1 making all the values on the plot be the same. A regression value of 0.30 (Figure 2.15e) is chosen to be the smallest value that minimizes the loss of information in the smoothing process, but large enough to produce a realistic pressure field void of pressure steps that are solely a result of interpolating data to a grid. For this reason, these plots are mostly used as a way to visualize the pressure field on the surface and are not meant to be used to find true SBLI characteristics. The majority of the information presented in this thesis for mean pressure only uses pressures from data points and not values interpolated to the grid. This lowers spatial resolution of line plots but ensures only accurate data is studied and not artificial data. However, by using a quasi-infinite region rather than just a single line, line plots with high spatial resolution can be plotted and studied. The determination of this quasi-infinite region will be discussed in subsection 3.2.1.

The only value determined from this interpolated field is the initial pressure rise. The initial pressure rise is the first location upstream of the interaction in which a pressure increase is seen. When studying pressure distributions, it is best practice to systematically determine the location of the initial pressure rise without simply using a threshold for a certain C_{p_n} value. However, due to the limited number of data points, the interpolated field is used to find the location of the initial pressure rise, and a threshold of $C_{p_n} = 0.03$ is set as the first instance of the pressure rise. This method is only used to find the line that distributions the initial pressure rise, and a more systematic method of determining the location of the location of the initial pressure rise as will be discussed in subsection 3.2.1.

2.6   Infrared Thermography

The second method used to study the mean flow topology of the SBLI is infrared thermography (IR) to study the heat flux on the surface. Table 2.4 shows the runs completed for this method. Measurements were taken with a FLIR X8051sc camera run at 120 Hz for 14 seconds to capture the run from before the tunnel was started to after the flow had stopped. IR cameras do not see through regular glass, so the window

(a) Bandwidth = 0.22

(b) Bandwidth = 0.24

(c) Bandwidth = 0.26

(d) Bandwidth = 0.28

(e) Bandwidth = 0.30

(f) Bandwidth = 0.32

(g) Bandwidth = 0.34

(h) Bandwidth = 0.36
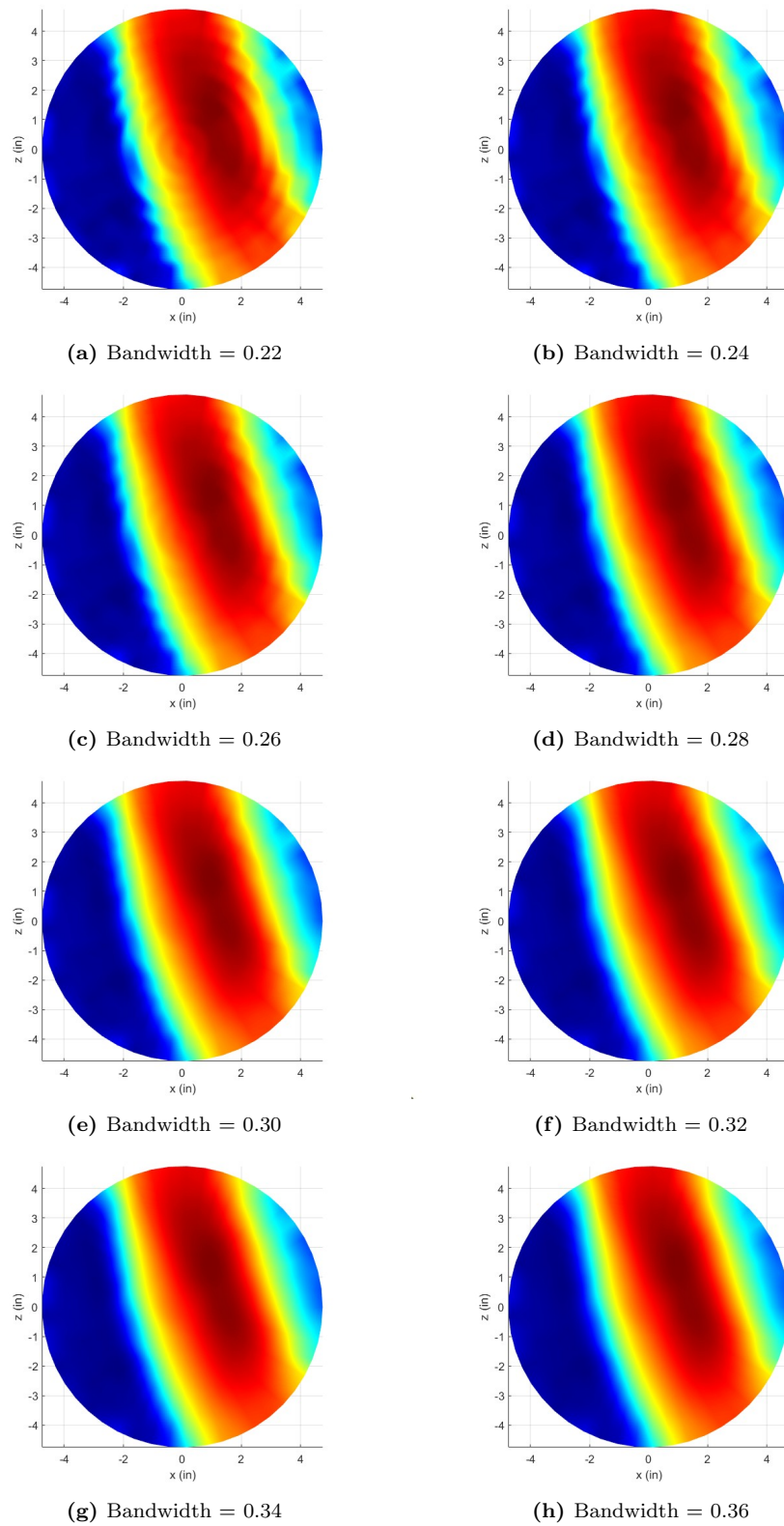
Figure 2.15: Effect of different kernel regression values on the pressure profile.

Table 2.4: IR Test Matrix

M_∞ [-]	2.1				3.0		
ψ [°]	20		40		20		40
p_0 [psi]	30	50	30	50	100	100	100
$\frac{Re}{L}^*$ [1/m]	30	50	30	50	100	100	100
C_{p_n} [-]	0.6	0.6	0.6	0.6	0.4	0.6	0.6
C_p [-]	0.5298	0.5298	0.3521	0.3521	0.3532	0.5298	0.3521
θ_{sg}	8.87°	8.87°	5.47°	5.47°	8.87°	11.04°	8.18°
T_w [K]	Unheated 30 50 80 100	Unheated 30 50 80 100	Unheated 30 50 80 100	Unheated 30 50 80 100	30 50 80	30 50 80	30 50 80

*Reynolds numbers averaged over run due to changing total temperature.

Table 2.5: PEEK Material Properties

Mechanical Properties	Values	Units
Tensile Strength	115	MPa
Thermal Conductivity	0.25	W/m·K
Density	1310	kg/m^3
Specific Heat	2200	J/kg·K
Emissivity	0.95	[-]

the camera looks through is made of sapphire. The directional emissivity of a material is a measure of how the emissivity of an object changes based on viewing angle. It is preferred to position the IR cameras near-perpendicular to the surface upon which the heat flux is measured to ensure this difference due to this effect of the directional emissivity is minimized, but the camera was positioned to look roughly 50° from the normal of the SBLI surface due to the experimental setup. However, studies show that associated error is generally within a 0.5°C margin if the camera is positioned to look at the heat flux surface at 60° from perpendicular (Mazdeyasna et al. (2023),Ibos et al. (2016)). To test this error, some heat flux measurements were done assuming a 2°K difference from the measured temperature, and the associated difference in the heat flux was around one percent. Further, a difference of 5°K resulted in less than a three percent difference in heat flux.

The SBLI surface used in this study is a 1/2" thick, 12.5" diameter plug made from polyether ketone (PEEK). This material is a well-known choice in the aerospace industry, and is chosen for its strength to be able to withstand pressures in the tunnel during the run as well as its well-documented material properties. The relevant properties are shown in Table 2.5. When looking at a surface with an IR camera, the camera does not just see the surface temperature depending on the given material. The IR camera is often able to

see through a small layer of the material and reads a temperature that is slightly different than the true surface temperature. For these experiments, PEEK is assumed to be an opaque surface. The effects of this assumption are not yet fully understood (Turbeville et al., 2024), but have been employed by Rataczak et al. (2021) and Turbeville et al. (2024) with reasonable confidence that this method produces small errors. This means that the temperature taken from the camera is interpreted as the surface temperature, and no correction is needed to find the surface temperature versus the measured temperature, which drastically decreases the computational requirements of the heat flux calculations. An important difference in the work done for these two works is that the heat flux tested by Turbeville et al. (2024) is done in a blowdown facility where the heat flux is calculated over longer duration (10 to 30 second intervals), whereas the work done by Rataczak et al. (2021) are conducted in a Ludwieg tube for tests around one second. This means that the temperature gradient in the material near the surface will be much higher for work done by Rataczak et al., but will penetrate a more shallow depth compared to the temperature distribution for the work done by Turbeville et al.. It is therefore reasonable to assume results for this thesis are more closely related to those done by Turbeville et al., and APWT is run for 10-15 seconds in these experiments which is much more similar compared to that of the work by Rataczak et al..

Comparing the work done by Turbeville et al. and the work done for this thesis in APWT, another notable difference is that the model used for these experiments is a flat plate, where as Turbeville et al. (2024) studied a hemisphere. This is important to note as the emissivity of a material changes based on the angle the surface is measured at by the camera. Turbeville et al. assumes the emissivity to be constant on the surface of the hemisphere and is shown to be a minor source of error. However, because this work is done on a flat plate, a constant emissivity across the plate is less of an assumption in this case, and should therefore be a smaller source of error than seen by Turbeville et al. (2024).

One limitation of PEEK is the strength of the material is not as high as a metal insert. PEEK being a type of plastic, it can withstand higher loads compared to other materials with similar properties that allow an IR camera to measure the temperature, but much smaller loading when compared to an aluminum or steel plug. This not only limits the size of the plug possible, but also the Reynolds numbers the tunnel can operate at. During a typical run, the pressure in the test section is much lower than ambient conditions of the room, so higher total pressures would yield less stress on the material in this case. However, if the tunnel is unable to start, the pressure behind the normal shock could be very high and likely blow the plug out of the tunnel which could be dangerous. Due to this and other starting loads, lower Reynolds numbers are required to ensure the model does not break. These lower pressures cause deflection of the material that can be seen during runs. This proved difficult to measure from the videos, so the deflection was modeled in SolidWorks using the known pressures during runs as shown in Figure 2.16. This pressure is modeled as the pressure difference between the tunnel during a run and the atmospheric pressure, and this difference is applied to the rear side of the plug. The maximum error when applying this pressure is estimated to be 0.047 in for Mach 3.0 runs and 0.027 in for Mach 2.1 runs based on the position of the camera in relation
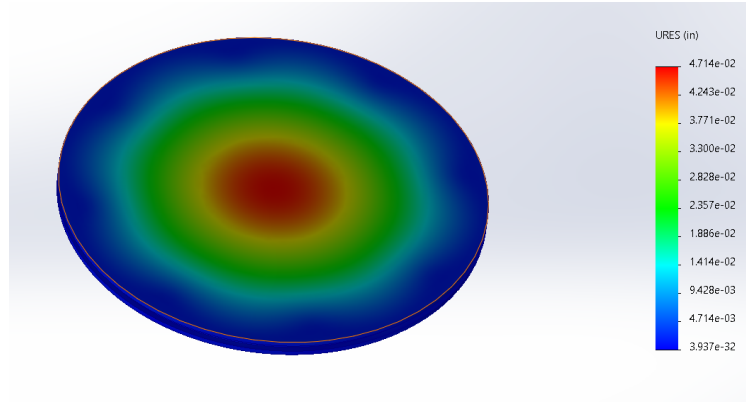
Figure 2.16: Simulation of PEEK displacement during Mach 3.0 run using SolidWorks assuming a 10 psi pressure load on the rear side of the plug.

(a) Displacement distribution along radius

(b) Surface angle relative to wall along radius
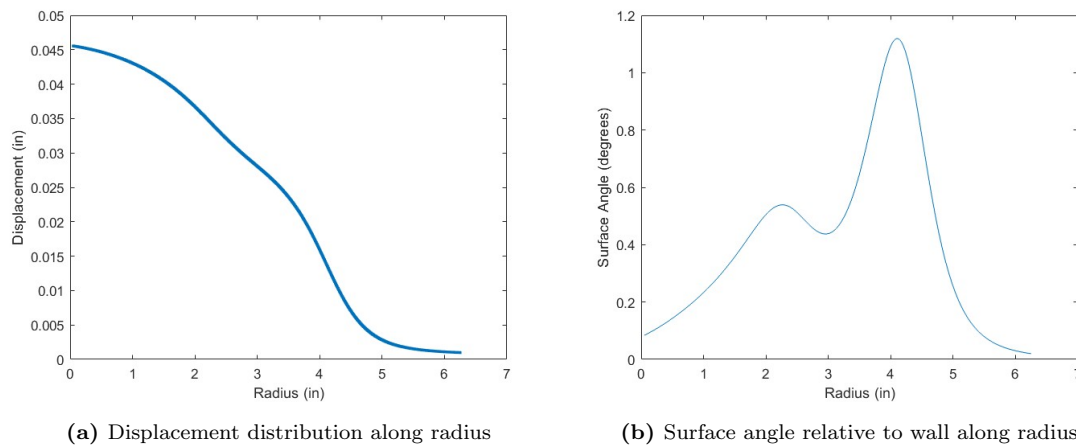
Figure 2.17: Average displacement along radius of the PEEK surface

to the tunnel and the modeled displacement from the simulations. This distance is within the error of the calibration dots used to transform the image and thus is not considered a source of error for the data taken from the PEEK plug. This also correlates to a maximum surface angle deflection of 1.12° and 0.47° for Mach 3.0 and Mach 2.1, respectively. The results of this for the Mach 3.0 case can be seen in Figure 2.17 which shows the average displacement and corresponding surface angle along the radius of the plug.

The IR camera does not measure in temperature, but instead measures counts. These counts must be converted to temperature by first being converted to radiance, and then converted from radiance to temperature. To do this, the camera must go through two calibrations. The first is a maintenance calibration that is only done roughly once a year. This requires that a blackbody of known emissivity and temperature are placed directly in front of the camera, and the measured counts are used to do a process similar to tarring a scale, but for the sensor in the camera. This calibration was done after the Mach 2.1 runs, but before the Mach 3.0 experiments. As will be shown, the Mach 3.0 experiments produced less noisy data
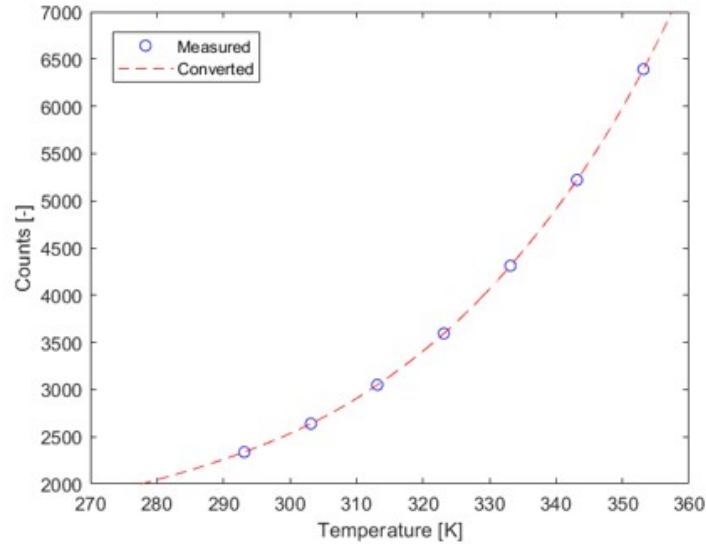
Figure 2.18: Conversion from counts measured by IR camera to surface temperature.

compared to that of the Mach 2.1 tests. It is unclear why this is, but this calibration could be reason the Mach 3.0 heat flux data has higher quality than that of the Mach 2.1 runs. Another possible explanation for this discrepancy between runs is that the camera shifted slightly or became out of focus for the Mach 2.1 runs. This would add minimal error compared to that of the Mach 3.0 runs.

The second method experiment specific and must be done every time the camera is moved. The camera is set up to view the appropriate surface as it would be as when the experiments are conducted. In place of the PEEK plug, the same black body is set up such that it is as close to where the SBLI surface would be as possible. The black body is set from $20 - 80°C$ in increments of $10°C$ to produce a plot of counts to temperature. This provides a conversion for counts to radiance, and the material properties are then accounted for when converting radiance to temperature. A line is then fit through these points to give an equation that can take counts as an input and produce a temperature for the given set up. A plot of this is shown in Figure 2.18. This calibration was done once for Mach 2.1 tests and once for Mach 3.0 tests. So, some variation between the two cases is expected, but not believed to be a source of error when comparing the two setups.

A final source of error is due to the window the camera looks through. Some runs show a region of reflection that is an artifact of this reflection and not a physical aspect of the flow. An example of this reflection is shown in Figure 2.19, where a sharp line can be seen in the middle of the plug. Once this feature was noticed, the camera angle was shifted minimally such that the reflected object no longer appeared on the surface.

The first step in studying this data is to transform the image in 2-D image. 25 calibration dots are drawn on the plug which are used to do the transformation. The prerun image (Figure 2.21a) is used for each case
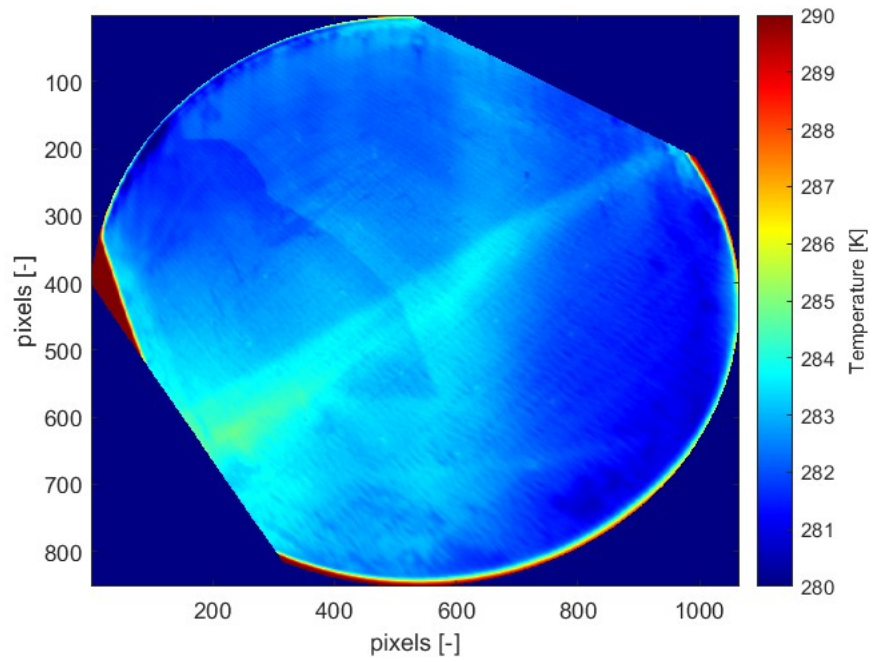
Figure 2.19: Raw image of temperature read by IR camera with a reflection from sapphire window.
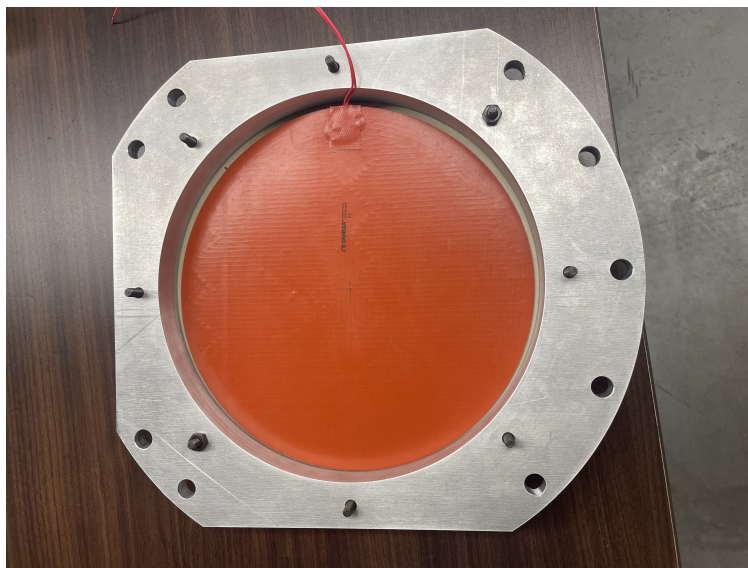
Figure 2.20: Image of the heater installed on the PEEK plug.

(a) Raw image converted to temperature   (b) Transformed image with non-PEEK surfaces removed
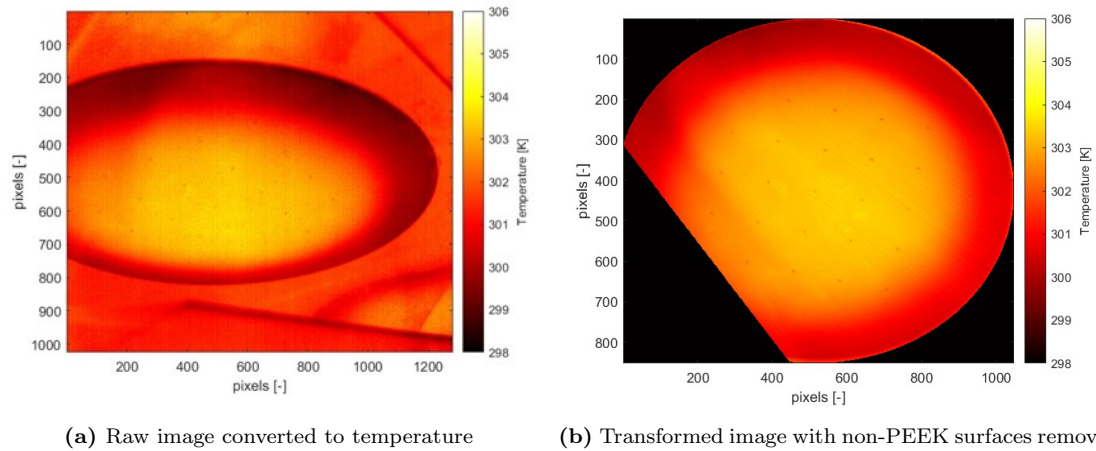
Figure 2.21: IR image before and after transformation is performed.

to do the transformation. Then, due to the tunnel shaking during the run, the entire video is place through a Matlab image stabilization code using the "Computer Vision Toolbox." This transformation is then applied to each frame in the video, resulting in a 2-D video of the run where the calibration points, and therefore the rest of the image, do not move during the run. This method has proven to produce reliable results for each of the tests performed throughout these runs. Due to the alignment of this data with the mean pressure and oil flow results, it is assumed that the error in the location this transformation provides is minimal.

The flow during the runs is very cold, and seeing heat flux on a cold wall is difficult and can produce noisy data. To increase the signal to noise ratio, a 10", $10W/m^2$ heater (Item\#SRFRA-10/10) is adhered to the rear side of the plug as shown in Figure 2.20 with a double-sided tape that can withstand the higher temperatures and effectively hold the heating pad to the plastic surface. The temperature is set and controlled by an Omega brand PID controller (Item# CN16DPT-304), and a schematic of the heater setup is also shown in Figure 2.22. The entire system is controlled by a standard 120V AC wall outlet. The heater is powered by a standard by the 120V power outlet, and the omega controller uses a power converter to convert the 120V AC power supply to 12V DC. The omega controller is then connected to a relay to turn the heater on and off as necessary to hold a constant temperature. PEEK has a glass transition temperature of around $140°C$. Because the PEEK was heated to over $100°C$ in some cases, it was important to use the temperature next to the heater to control the temperature of the plug rather than the temperature exposed to the flow. This not only ensured the structural integrity of the plug, but it was also found that there is a minimal temperature difference between the front an rear side before the run. This ensures an even temperature profile into the depth of the material in improves confidence in heat flux calculations.

A nylon ring is placed in between the PEEK surface and the aluminum frame the plug is attached to help insulate the PEEK and allow for more even heating on the surface along the radial direction. The plug has three thermocouples installed that are held in with a thermal epoxy. Two temperature probes are 0.1" beneath the SBLI surface, and one is placed just at the heater-PEEK interface. The thermocouple at
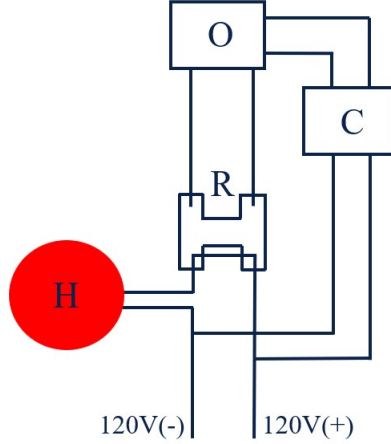
Figure 2.22: Schematic of heater used to heat PEEK plug. "H" is the heat pad, "C" is is the AC to DC power converter, "O" is the Omega controller, and "R" is the relay to divert power to and from the heater.

the heater-PEEK interface is used by the PID controller to set the plug temperature for each run, and the remaining two thermocouples at the surface are used to verify temperatures measured by the IR camera. A chart of the surface temperature measured from two thermocouples in the PEEK, one placed on the PEEK surface, and the IR camera compared to the set temperature of the PID controller is shown in Figure 2.23. The results of this show an error within $5°K$, which is higher than ideal, but again, only results a few percent error in heat flux and is therefore acceptable.

To measure heat flux, the 1-D heat transfer equation (Equation 2.8) is used in tandem with Equation 2.9. Equation 2.8 is used to assume a temperature profile where n represents a time index, and i is the location index of each node. The boundary conditions for this temperature profile are such that the rear temperature is held constant through the run, and the front temperature is taken directly from the camera measurement. The heater is left on for a sufficiently long time to allow for the entire depth of the plug to reach a constant temperature. Figure 2.24 shows the surface temperature versus the temperature of the side of the plug touching the heater at different set temperatures. This shows that once the plug has been heated a sufficient amount of time, the temperature of the plug is relatively even throughout the entire depth of the plug, and only small differences were seen from the front compared to the rear temperature. A linear relation between the front and rear temperature is used to estimate the temperature profile of the rear side before each run. Further measurements from the rear thermocouple show that, during the run, the temperature of the rear side of the plug remains constant (see Figure 2.26).

$$T_i^{n+1} = T_i^n + \alpha \left[\frac{T_{i-1}^n - 2T_i^n + T_{i+1}^n}{\delta x^2} \right] \delta t \tag{2.8}$$

$$q = -k \frac{dT(x)}{dx} \tag{2.9}$$
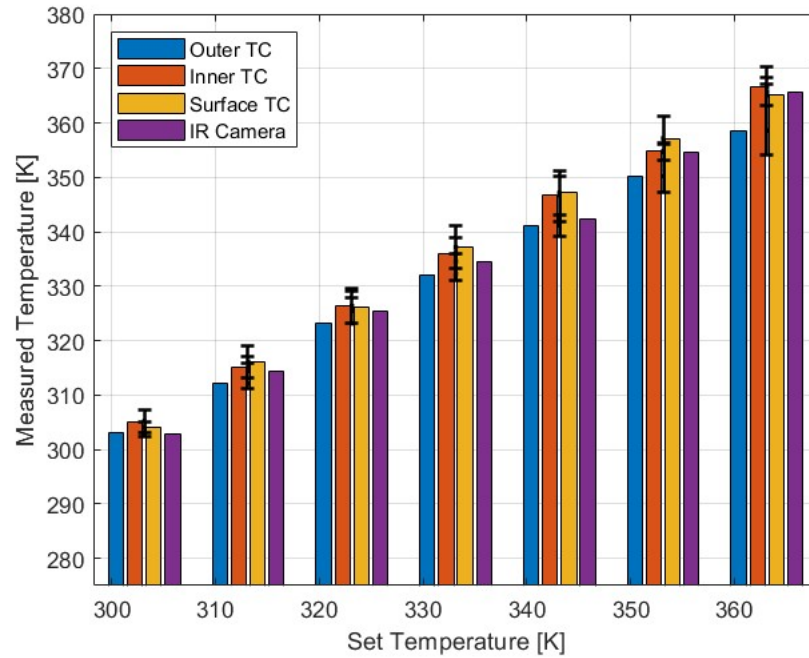
Figure 2.23: Comparison of measured temperatures from a thermocouple (TC) near the center of the plug (inner TC), a thermocouple closer to the edge of the plug (outer TC), a thermocouple placed on the surface just for these measurements (surface TC), and the IR camera measurements (IR camera).
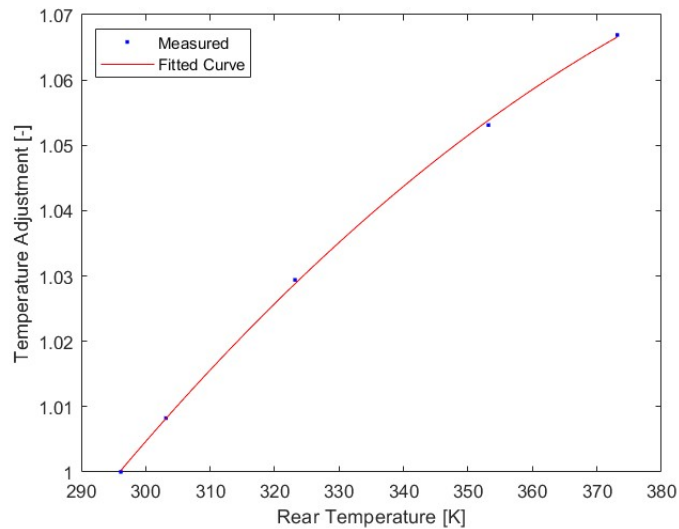
Figure 2.24: Temperature difference between heated surface and tunnel side surface before the run at different set temperatures.

(a) Heat flux in time at one location

(b) Corresponding temperature profile in time
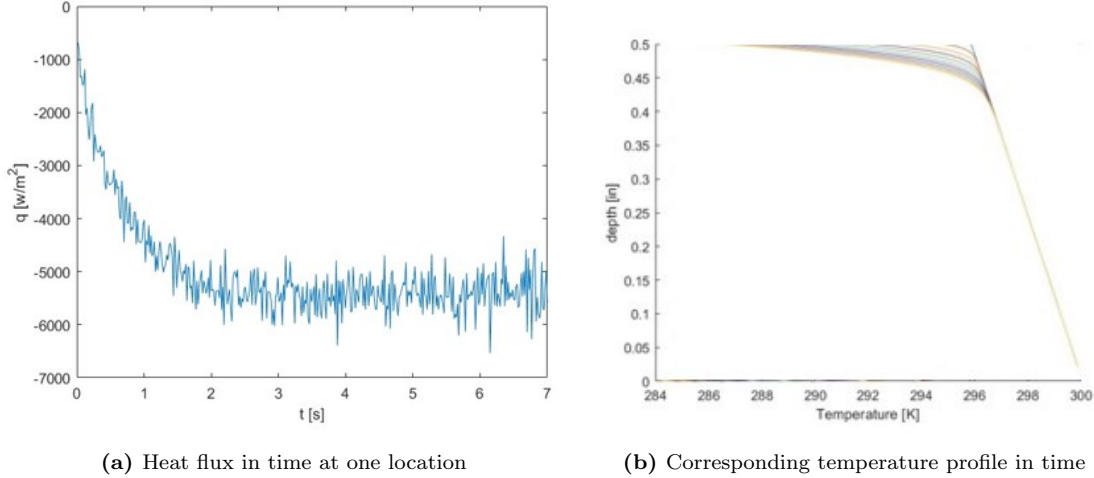
Figure 2.25: Heat flux throughout a run and the associated temperature profile in the plug for one location. Each line representing a step in time.

These heat flux measurements are used to find the Stanton number across the interaction. St is calculated using Equation 2.10, where T_{aw} is the adiabatic wall temperature, q_w is found from the IR camera and the 1-D heat transfer equation, T_w is the surface temperature of the plug, the flow conditions at the time of the run are used to find velocity and density during the run, and C_p is assumed constant at $1005 \frac{J}{kg \cdot K}$.

Figure 2.25 shows the heat flux for a single point during a run and the associated temperature profile at that point in the plug. Each line in the right figure represents a temperature profile for a given time step, with the initial temperature profile being the straight line. It is worth noting there is an associated error in this method. Due to computational limitations, calculating the heat flux for the entire run was not feasible. As a result, the linear temperature profile approximation is not a good representation of the temperature profile at the time of the run. Since the beginning of the heat flux calculations is taken in the middle of the run, the temperature profile is better represented with a profile similar to one of the temperature profiles in the middle of the run. Attempts to artificially introduce this temperature profile by using the pre-run temperature and an arbitrary time step until the first temperature of the available data proved to mostly remove this nonlinear section of the heat flux, but increased the values of the constant heat flux section which likely skews the data and is not the true heat flux values. It is therefore assumed that the original temperature profile is linear, and the only data taken from the linear section of the hear flux data is used in the remaining calculations.

$$St = \frac{q_w}{\rho_\infty u_\infty C_p (T_{aw} - T_w)} \tag{2.10}$$

The use of the heater aids in two aspects of studying heat flux: it reduces noise as temperature gradients are much higher than compared to an unheated surface, and it provides a way to support an adiabatic wall temperature estimate throughout the entire interaction. Vitols (2024) and Gross et al. (2018) have shown
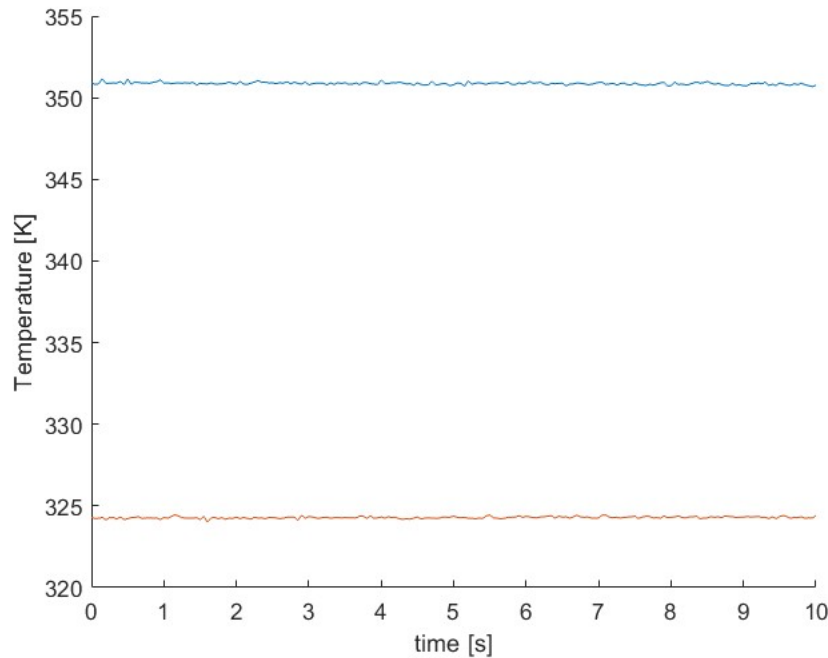
Figure 2.26: Temperature measured on the rear surface thermocouple during two different runs.

that the adiabatic wall temperature changes in different locations of the interaction, so fitting a profile is useful in finding an accurate Stanton number over the surface. To do this, heat flux is measured at multiple wall temperatures, and a linear regression is fit through the data to find at what wall temperature heat flux is zero on a heat flux versus temperature plot to extrapolate the adiabatic wall temperature. This will be discussed further in the results section.

The use of the heater does introduce some challenges. Namely, the heater is only a 10" diameter compared to the 12.5" diameter plug. This means the outer radius of the plug is not heated and leaves an uneven heating profile which is difficult to model and adds a level of uncertainty in the heat flux results. An image of this uneven heating profile before a run is shown in Figure 2.27. The average temperature profile along the radius of the plug is shown to further highlight this uneven heating. Calculating Stanton number should make the sections of the plug unaffected by the SBLI to have a constant value. Yet, for higher plug temperatures in particular, this is not the case. For these higher temperature plug temperatures, there is a clear ring of higher Stanton number values near the outer ring of the plug and a steep decrease in Stanton number in the unheated regions. The first possible explanation of this error is in the rear temperature profile. To determine the temperature of the rear surface of the plug, the temperature profile of the pre-run plug is used with the errors outlined in Figure 2.24. The appropriate error is multiplied to the pre-run profile and this is the assumed temperature profile of the rear side of the plug. It is speculated that there are some 2-D heat transfer effects that cause the rear temperature profile to have a larger constant temperature region compared to the surface temperature profile shown in Figure 2.27. This would artificially increase the heat

(a) Assumed Rear Temperature Profile with Heater Edge   **(b)** Prerun Temperature Profile Uniformity
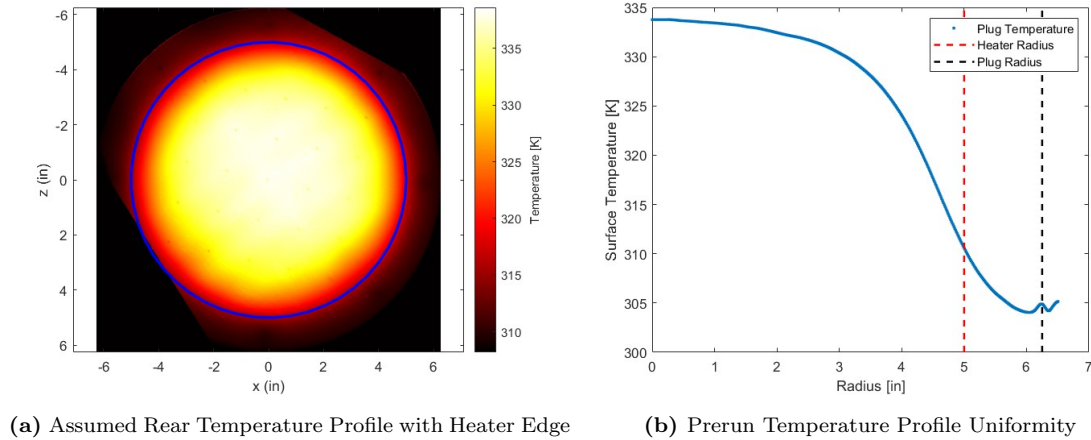
Figure 2.27: Temperature distribution of heated plug before run.

flux (and consequently the Stanton number) for a small area as the assumed temperature difference is higher than the true temperature difference between the two surfaces. Another explanation is that the uneven heating around this area increased errors when calculating the adiabatic wall temperature, and this error is then exasperated in the Stanton number calculation. Correcting this issue is outside the scope of this thesis, but is important to note as the data outside the constant heated region is unreliable because of this. Future work should emphasize making the constant heated region as large as possible to increase the usable SBLI surface area.

2.7   Oil Flow Visualization

The final method for characterizing the mean flow topology is oil flow visualization. Oil flow visualization provides good insight into the location of notable features of the the interaction on the surface. Looking at the streaks allows for the visualization of the initial influence of separation on the incoming flow, the separation line, and the reattachment line. Determining the location of both the separation and reattachment line are how the interaction is determined to be cylindrical or conical, and thus having multiple methods to determine the location of these features is useful to increase the confidence of the results. This is especially true for the location of reattachment. Figure 1.2 shows the location of reattachment in relation to the pressure distribution, and the location of reattachment in relation to the Stanton number distribution will be discussed in later sections, but both methods only offer an approximate location of reattachment. While there is still some uncertainty when determining this location using oil flow, it offers a more accurate result to increase confidence in determining whether the interaction is cylindrical or conical.

Merzkirch (1987) and Koca et al. (2024) discuss different surface flow visualization techniques used in recent works. The method determined to be the most feasible for these tests is outlined in Merzkirch (1987), where a mixture of roughly 50% TiO_2, 50% kerosene, and 1% oleic acid to help bind the TiO_2 to the kerosene
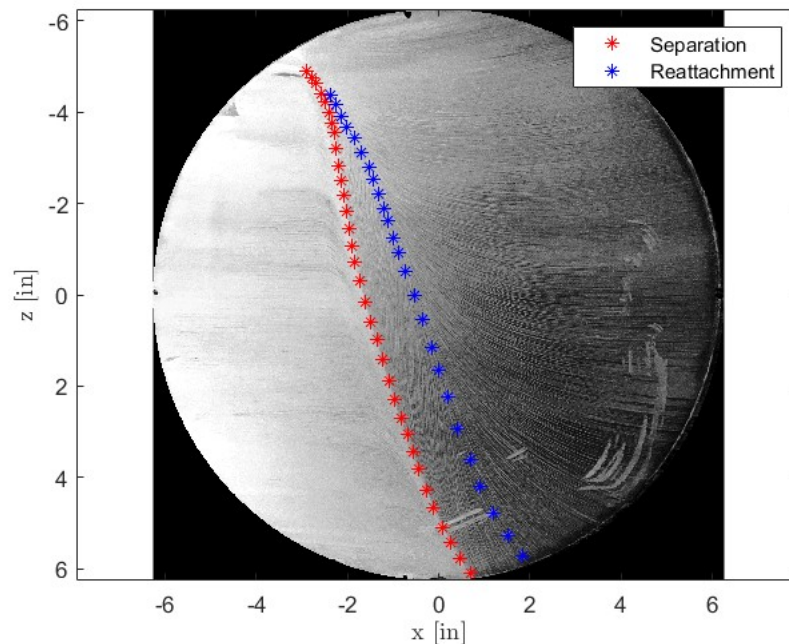
Figure 2.28: Plotted separation and reattachment points.

is painted on the surface of the SBLI to reveal skin friction lines. While the tunnel runs, the mixture follows the direction of the local skin friction gradient and the kerosene begins to evaporate. The run continues until only the TiO_2 remains on the surface to reveal the local flow features on the surface.

For these experiments, the large scale of APWT and chaotic manner of startup made it very difficult to get the mixture to reveal defined lines for Mach 3.0 runs. The startup period of Mach 3.0 proved to be too long, and all the kerosene evaporated before the SBLI was able to form. Thus, oil flow visualization was unable to be collected for Mach 3.0 flows, but successful runs were completed for Mach 2.1 cases.

To study these images, a mixture of hand picked points and code based image processing is used to ensure accurate reading of the images. Data taken from these images proves consistent with results from ISWT and showed good agreement with pressure and heat flux measurements as will be discussed later. The first method of picking points done by hand was used to determine the location of separation and reattachment. This is accomplished by selecting many points along the line to first draw an initial profile of the separation and reattachment lines. An example of this can be seen in Figure 2.28, which depicts the points selected along the separation (red) and reattachment (blue) lines. Due to the nature of selecting points by hand, some level of error is associated with this method. To help minimize this error, a kernel smoothing regression similar to the method discussed in the mean pressure section is used to smooth over some of the imperfections in the hand selected points, but this smoothing is minimal as to prevent deviation from the true separation and reattachment lines. Lastly, to determine the error bars, the process of selecting points is done five times, and the maximum deviation from the selected line across all five sets of points is used to determine a maximum
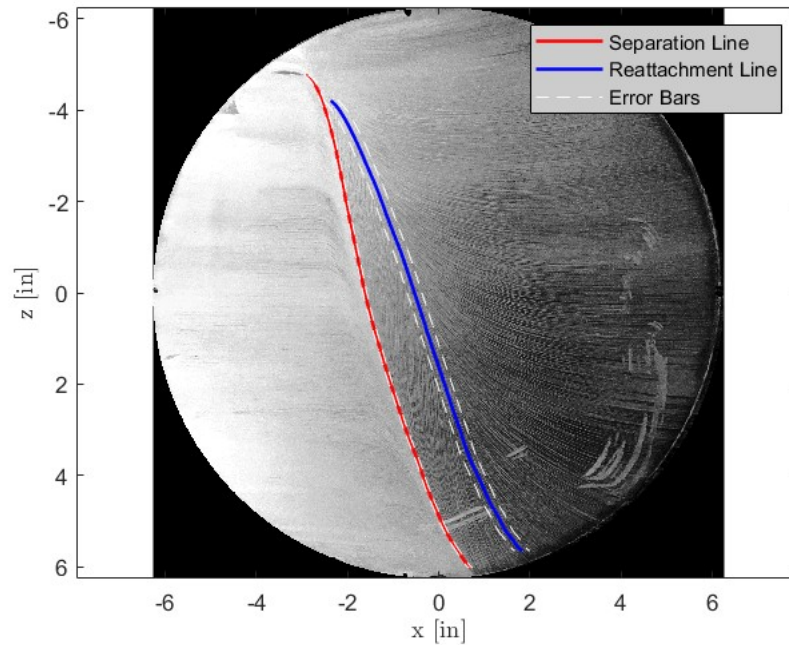
Figure 2.29: Oil flow for Mach 2.1, $\psi = 20°$

error for the lines. A figure of the smoothed lines and the associated error bars is shown in Figure 2.29. Notably, the confidence interval of the location of the separation line is much smaller than the one for the reattachment line. To further support this location, skin friction vectors have also been plotted.

For the black and white image of the oil flow, the picture can be converted to intensity (0 representing black and 255 representing white). Then, the change in intensity in the x and y for each pixel is used to determine the partial derivative of the intensity at each pixel of the image. This derivative can then be used to determine the direction of the streak at each location because the change in intensity should be at a minimum along the streak line where the TiO_2 is left on the surface. These results and the results from the hand picked points allow for a high confidence in the results from the oil flow visualization. A raw image of the results from this process is shown in Figure 2.30.
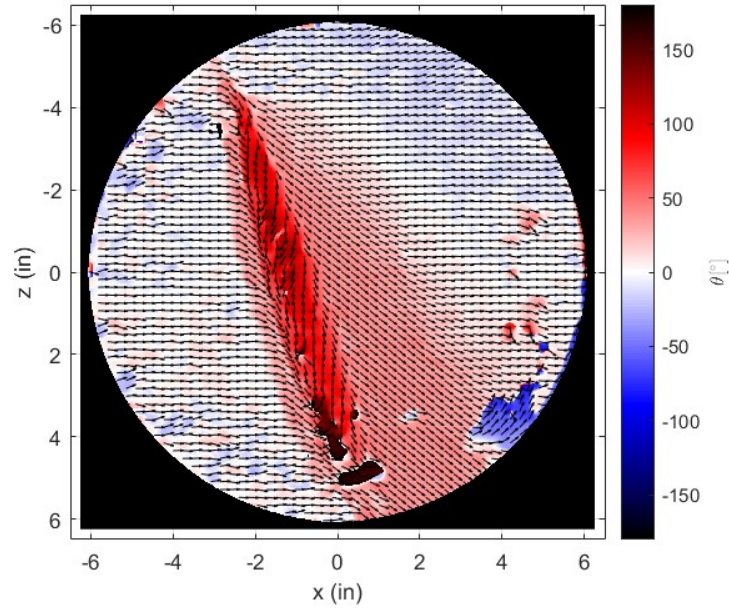
(a) $M = 2.1, \psi = 20°$
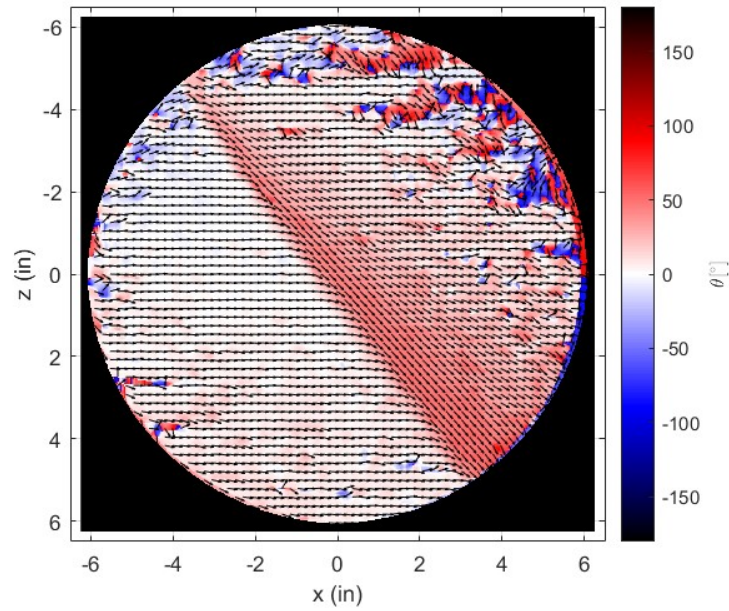
(b) $M = 2.1, \psi = 40°$

Figure 2.30: Results from image processing of streaks using intensity derivatives.

Chapter 3

Results

3.1 Oil Flow Visualization

The study of the streaks left by the swept SBLI using oil flow visualization has revealed that the $20°$ case separated and the $40°$ case remains attached. Figure 3.1 shows the important flow features for the Mach 2.1, $\psi = 20°$ and $\psi = 40°$ cases over the oil flow images. In these figures and all subsequent data presented in this thesis, the freestream direction is left to right. The solid black line outlines the location of the shock generator above the SBLI surface. The dashed magenta and cyan lines represent the location of the impinging shock and expansion fan locations on the surface, respectively. The dashed white line shows the location of the initial upstream influence as determined by mean pressure measurements (the determination of this line will be covered in the mean pressure measurements part of this section). The purple dashed circle represents the location of the mean pressure region. Lastly, for the $\psi = 20°$ case, the red and blue lines represent the separation and reattachment lines respectively. Around the center of the image, there is high confidence in the selection of these points, but both the side closest to the root and the side near the tip were difficult to determine. For the side near the root of the shock generator, the thicker layer of TiO_2 makes it difficult to determine if the line plotted is real or an artifact of the uneven oil distribution next to the small gap between the plug and tunnel wall. On the side of the plug near the tip of the shock generator, the separation line is still clearly visible, but the reattachment line becomes very difficult to determine. For this reason, the error around these points is expected to be slightly higher than in the center of the plug, but, as will be discussed at the end of this section, this is outside the region of interest and is thus not accounted for.

Looking at the initial pressure rise line, it is seen that the streaks tend to be straight in the direction of the freestream upstream of the line, and begin to curve just downstream of this line as expected. This figure further indicates the existence of flow separation in that the flow can be seen diverging from the reattachment line where the flow is forced upstream just in front of the reattachment line and returns to moving downstream aft the reattachment line. On the contrary, the $40°$ case shows no indication of separation. From Figure 3.1, the $40°$ case shows a deflection of the flow just downstream of the initial pressure rise line, but has no reverse flow. Interestingly, along the span of the tunnel for the $40°$ case, the streaks become more swept at higher spanwise locations until at the end of the span they are parallel to the sweep angle. This is especially
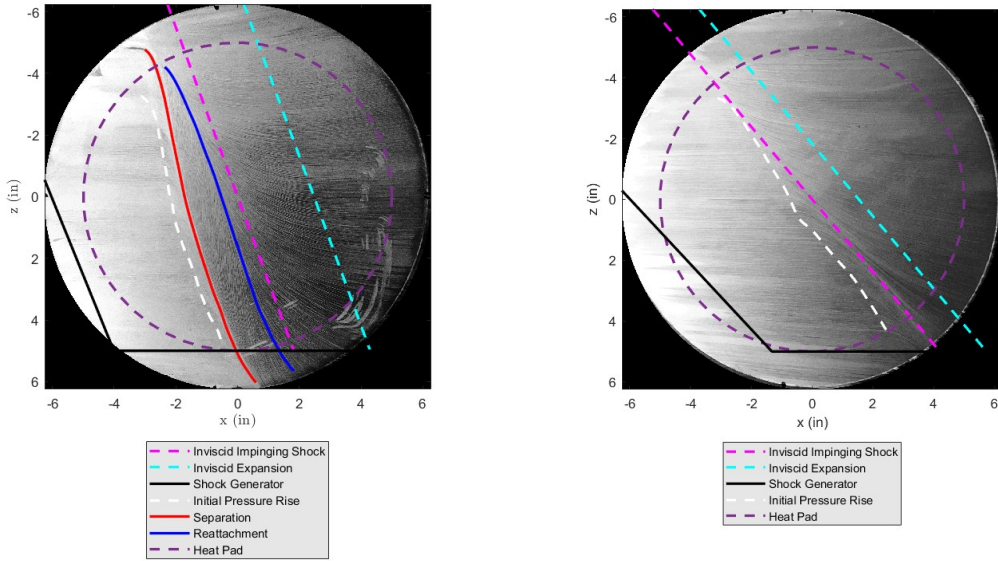
(a) $M = 2.1, \psi = 20°, C_{p_n} = 0.6, p_0 = 30psi$ (b) $M = 2.1, \psi = 40°, C_{p_n} = 0.6, p_0 = 30psi$

Figure 3.1: Oil flow visualization of $\psi = 20°$ and $\psi = 40°$ sweep cases in APWT with relevant flow conditions plotted.

apparent in Figure 3.3. This would suggest the spanwise component of flow is increasing along the span of the interaction as there is an almost immediately change in the direction from the freestream direction to the sweep angle after the impinging shock. This is in agreement with similar work done by Padmanabhan et al. (2021a), that shows the spanwise component of the flow increases along the span of the interaction in the direction of sweep.

Comparing these images to the ones taken in ISWT Figure 3.2, for the 20° case, the location of reattachment is slightly upstream of the inviscid impinging shock as in APWT. Further, the region of reverse flow is clearly visible in both tunnels. However, one main difference between this case is the two lines around separation in the ISWT SBLI. Doehrmann (2018) first noted this phenomena and suggested a few theories for this. Firstly, it could be due to the unsteady motion of the shock foot causing the oil to coalesce at the furthest upstream and downstream locations of this shock motion. Another theory is that the shock fan caused by the boundary layer at the base of the shock might create an initial pressure rise that is strong enough to cause the oil to coalesce at this pressure gradient, and the second streak indicates the location of the true separation. Neither of these theories has been proven as of yet, but the interaction in APWT seems to offer no insight into this phenomena. The oil flow in APWT shows no indication of the second line near the separation region. This result is more consistent with previous works that study oil flow in SBLI, which show a single clear line at the separation line rather than this double line (Saad et al., 2023; Jurkovich, 1984).

(a) $M = 2.3, \psi = 20°, C_{p_n} = 0.6$ **(b)** $M = 2.3, \psi = 40°, C_{p_n} = 0.6$
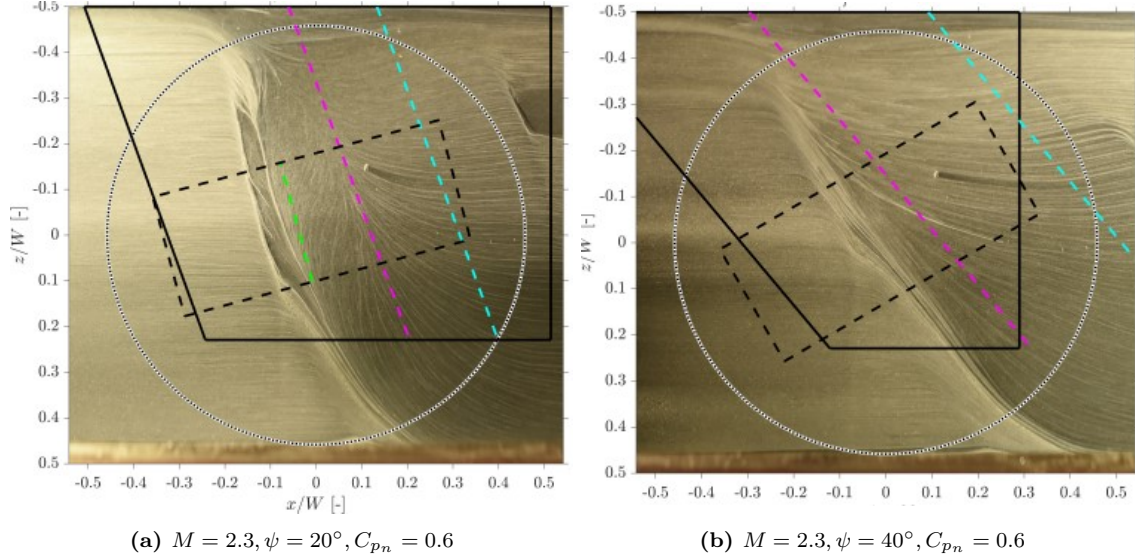
Figure 3.2: Oil flow visualization from ISWT with relevant flow conditions plotted Vitols (2024).

Further analysis of the oil flow using the streak vectors supports the location of the separation, reattachment, and initial upstream influence of the interaction lines. Figure 3.3 highlights the change in vector direction with a color gradient on the image where white is the freestream direction. As can be seen, there are clear direction changes in the flow just downstream of the initial pressure rise, another clear direction change at the separation line, and lastly diverging vectors at the reattachment line. Further, this plot shows the effect of the expansion fan on the flow as the flow returns to the freestream direction downstream of the inviscid expansion location.

Given the location of the separation and reattachment lines, determining cylindrical or conical separation and the location of the quasi-infinite region can be determined. Figure 3.4 shows the sweep angle of the separation and reattachment lines where the center of the tunnel is defined at $z = 0$ and the location of the root is at $z = -7.5$ inches. As expected, the angle of the separation line is much smoother because the points were picked by hand and it is a much clearer line to define. Conversely, the reattachment line varies much more along the span, but this is not a real flow feature. Rather, it is an artifact of selecting points slightly off of the true location of the reattachment line. This is further emphasized by looking at the error bars on this line compared to the separation line. As noted in the previous section, the errors were estimated from the location of the both the separation and reattachment lines. These errors are used to calculate the associated error for Figure 3.4, Figure 3.5, and Figure 3.6. With this taken into account, it can be inferred that the reattachment line angle along the sweep is likely a smooth line in between the respective error bars. Similar to this, the distance from separation to reattachment has been calculated along the span of the interaction. This distance is defined as the distance to the reattachment line normal to the separation line at each spanwise. The results of this are shown in Figure 3.5. Looking at Figure 3.5 and Figure 3.4, the slope of the reattachment line is steeper than the separation line for initial part of the interaction, but
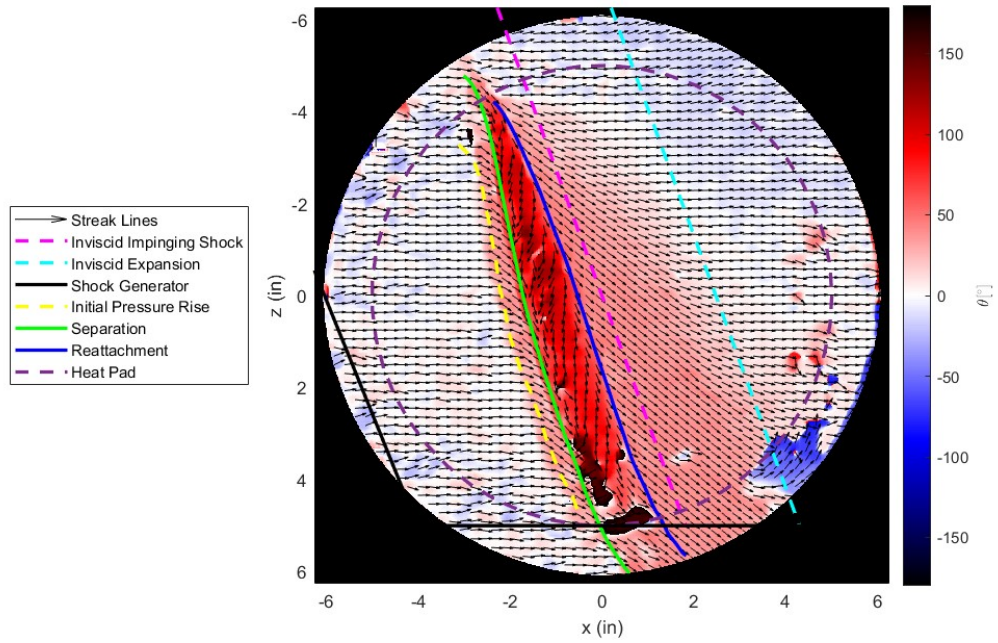
(a) $M = 2.1, \psi = 20°, C_{p_n} = 0.6$
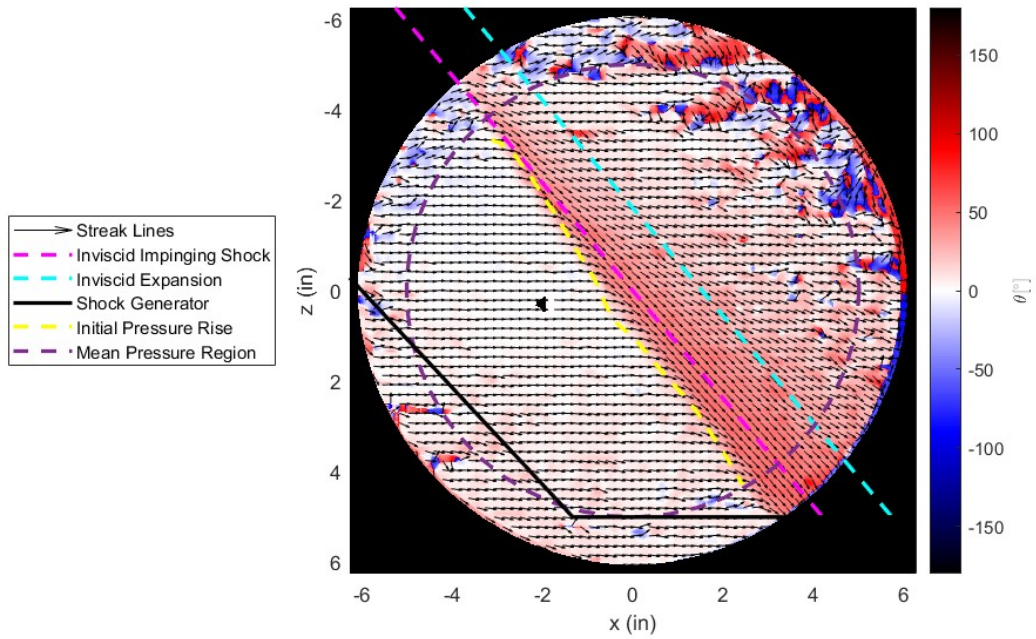
(b) $M = 2.1, \psi = 40°, C_{p_n} = 0.6$

Figure 3.3: Streak visualization for flow in APWT with relevant flow conditions.
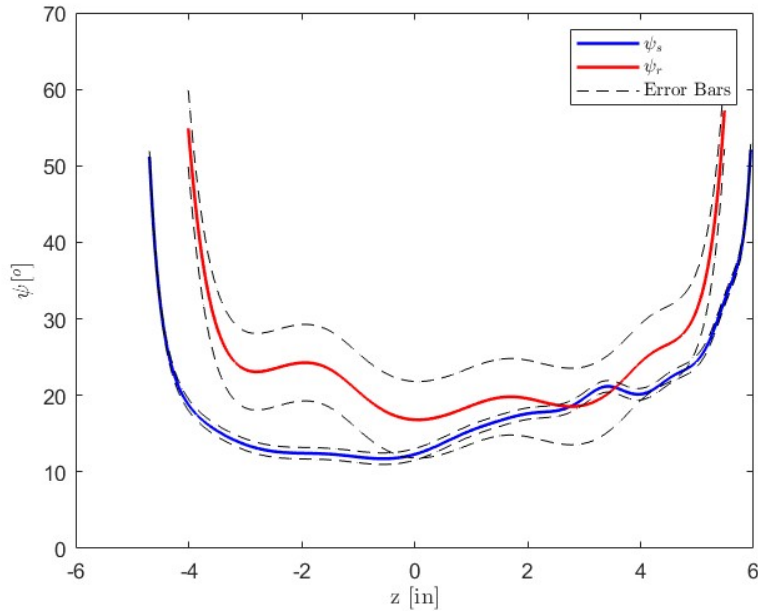
Figure 3.4: Sweep angle of the separation and reattachment lines along span for $M = 2.1, \psi = 20°$.

near $z = 0$, these lines approach the same sweep angle. Therefore, the normal distance from separation to reattachment gets larger along the span until around $z = 0$, but then approaches a relatively constant value. Even with the associated error, these trends suggest that the interaction becomes cylindrical further from the root of the shock generator. However, it is still beneficial to study the entire span of the interaction within the quasi-infinite region to ensure the entire interaction is accounted for, especially in cases where no oil flow data is present.

The final plot (Figure 3.6) depicts the change in sweep of the separation line along the span of the interaction. As shown here, the sweep of the separation line is relatively constant across the majority of the span. Therefore, the quasi-infinite region for this interaction is defined as the section of the interaction where the change in slope is near zero. Due to the selection of points, this is not an exact method of defining a region as there is some variability in these selected points, but it is estimated to be from $z = -4$ to $z = 4$ as indicated by the red dashed lines on Figure 3.6 and Figure 3.7. These values are chosen such that the estimated change in sweep is less than $1°$. This provides a margin for error such that just outside this region likely still falls within the quasi-infinite region, but until a systematic method for choosing this region is agreed upon, this method offers reliable results with a greater confidence that root and tip effects are not influencing the results. However, while this tells what the quasi-infinite region is for this specific case, each case will have a different region. Without oil flow for the Mach 3.0 cases, this region is approximated from the mean pressure results which will be discussed in the next section, but the z-limit is held within this $z = \pm 4$.

(a) Normal distance from separation to reattachment

(b) Coordinate system for the distance from separation to reattachment
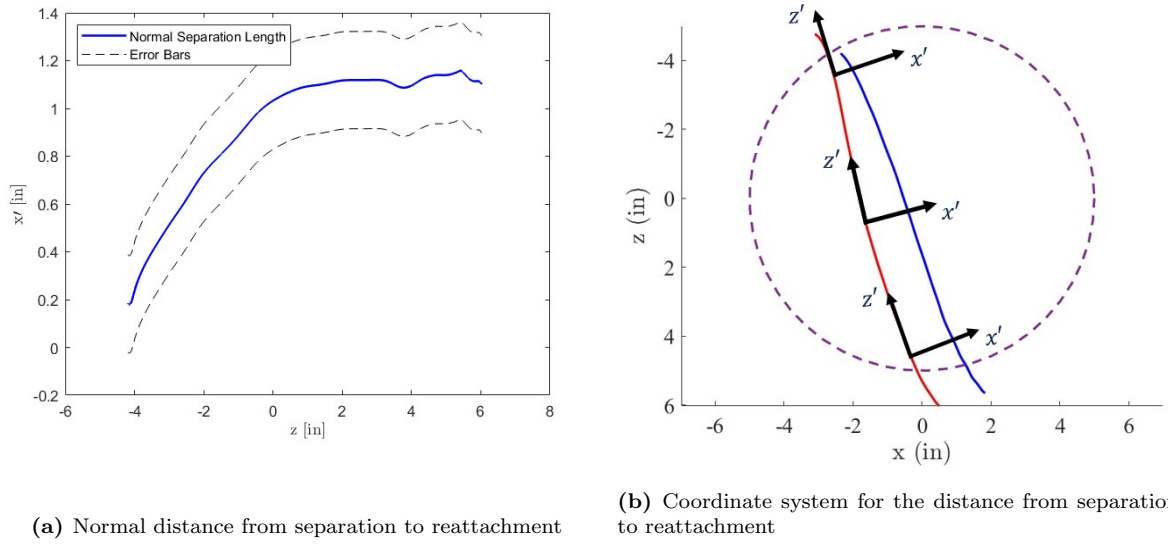
Figure 3.5: Distance from the separation line to the reattachment line along span Figure 3.5a with the defined distance at each spanwise location Figure 3.5b.
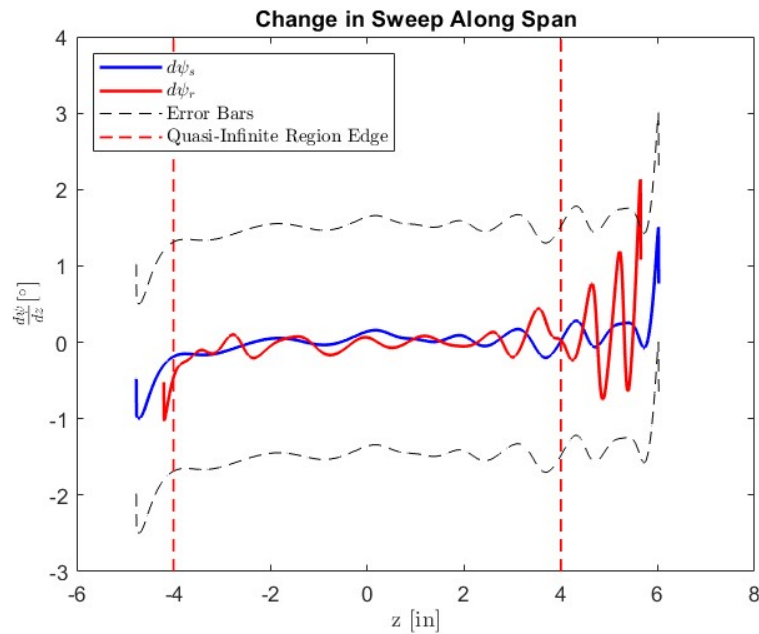
Figure 3.6: Change in sweep of the separation line along span with red circles noting the edge of the quasi-infinite region.
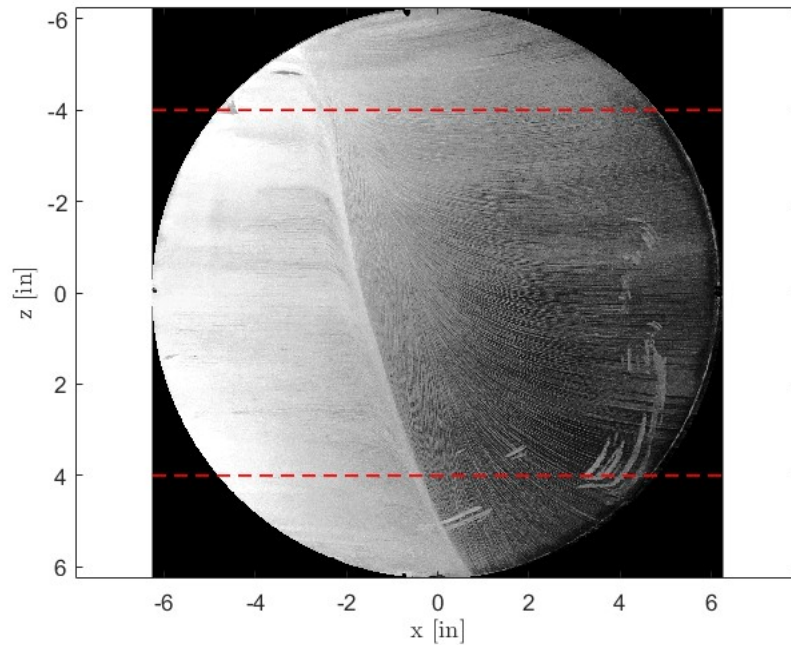
Figure 3.7: Region of interest based on area of constant sweep.

3.2 Mean Pressure Measurements

Static pressure measurements are utilized to determine if a case indicates separation of the interaction. Figure 3.9 shows the interpolated C_{p_n} map for the five cases run. Looking at these pressure values, the first notable point is that there is some variability in regions that should hold constant values. For example, the C_{p_n} should be zero upstream of the initial pressure rise, but there is some variability in the upstream pressures. This is likely due to small errors in pressure measurements and tunnel noise, but not assumed to have a significant impact on the results. It is next important to note that the interpolation of data from the distributed points to the striuctured grid has caused some flow features to appear that are not physical. Most notably, the pressure rise of the 40° case at both Mach 2.1 and Mach 3.0 occurs nearly parallel to the inviscid shock for the majority of the span of the interaction, but there is a sizable change in this slope near (0,0) of the plug before it returns to that 40° sweep angle. The location of this happens just outside the first ring of points where pressure information is collected, and is therefore in an area with missing data. The resulting interpolation at this location makes it look like there is a phenomenon is occurring in the region in the middle of the plug, but comparing to Figure 3.1 and Figure 3.3 supports that there is nothing occurring at this location on the plug. This is just an artifact of missing data at the initial pressure rise line. However, even with these errors, the interpolated mean pressure profile of the interaction shows good agreement with the oil flow images as can be seen in Figure 3.8. As expected, the initial pressure rise of the interaction aligns well with the first change in streaks on the oil flow, and the separation and reattachment lines flow the
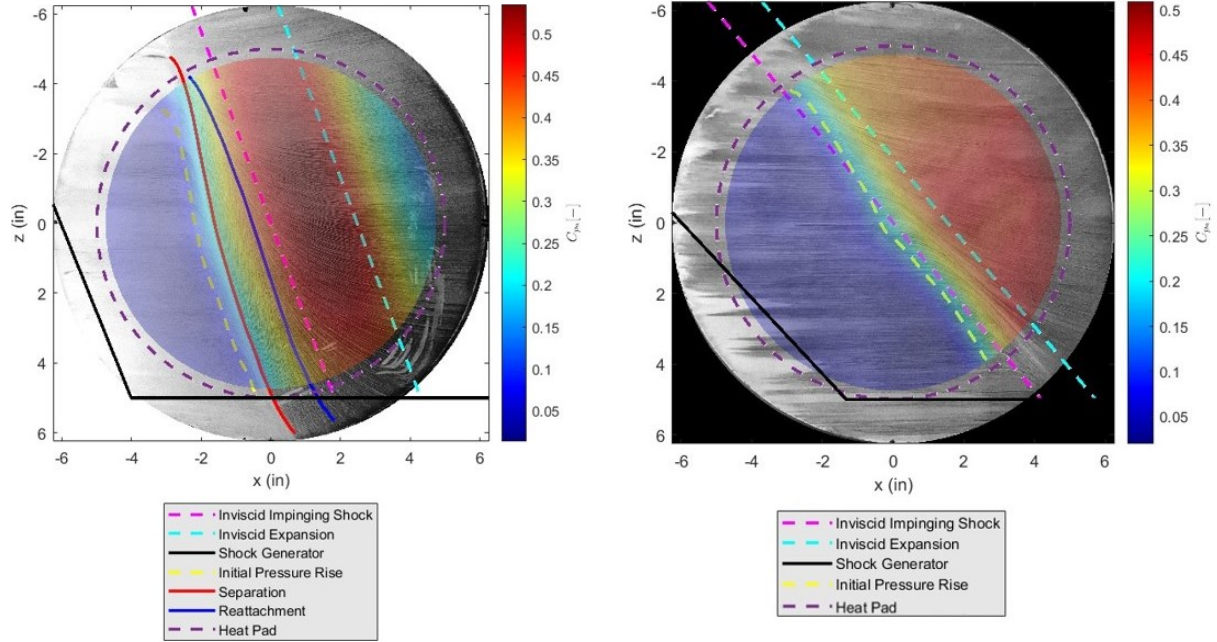
(a) Oil flow and pressure map overlap for $\psi = 20°$

(b) Oil flow and pressure map overlap for $\psi = 40°$

Figure 3.8: Mean pressure and oil flow visualization comparison for Mach 2.1 cases.

pressure contour well for the 20° case. Even for the 40° case, outside the area near the center of the plug, the initial upstream influence of pressure aligns well with the oil streaks, and the very sudden pressure rise matches with the quick change in the direction of the streaks before they return to the freestream direction.

It is also important to note that the case with a $C_{p_n} = 0.4$ looks much less smooth. Due to time constraints, only half the number of runs were able to be completed for this case. This caused the number of data points collected to be half the amount of the rest of the cases. So, interpolated results from this case appear worse. These rough flow features are not expected to be physical, and data taken from this case is still expected to be useful as only the values from the pressure measurements are used in pressure distribution calculations and not the interpolated values. Further, it can be seen that the interaction of this case occurs very far downstream of the plug, and some information of the interaction is lost because of this. This is a result of constraints on where the shock generator could be mounted in the tunnel, and the results ascertained from this case need further analysis to better support any conclusions drawn from features far downstream in this case.

To visualize this data, it is required to define a new coordinate system that accounts for this sweep. This allows for a uniform comparison between different tests that have different separation locations and different sweep angles. Figure 3.10 shows an example of the chosen coordinate system. The blue line represents the initial pressure rise. $x_s = 0$ is chosen as the line where the initial pressure rise is at $z = 0$. For consistency, $z_s = 0$ remains at the location where $z = 0$.
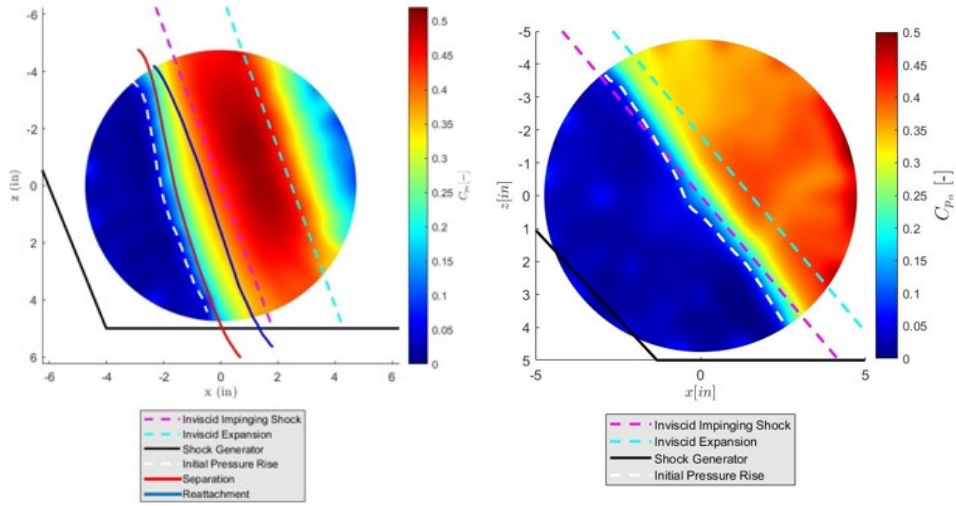
(a) $M = 2.1, \psi = 20°, C_{p_n} = 0.6, p_0 = 33psi$

(b) $M = 2.1, \psi = 40°, C_{p_n} = 0.6, p_0 = 33psi$
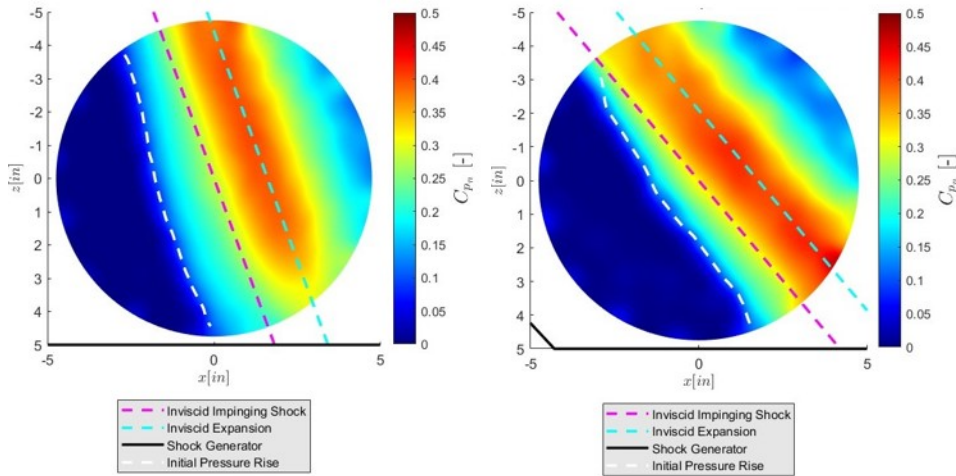
(c) $M = 3.0, \psi = 20°, C_{p_n} = 0.6, p_0 = 88psi$

(d) $M = 3.0, \psi = 40°, C_{p_n} = 0.6, p_0 = 90psi$
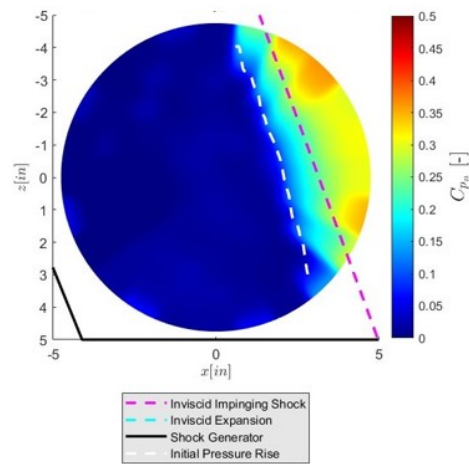
(e) $M = 3.0, \psi = 20°, C_{p_n} = 0.4, p_0 = 90psi$

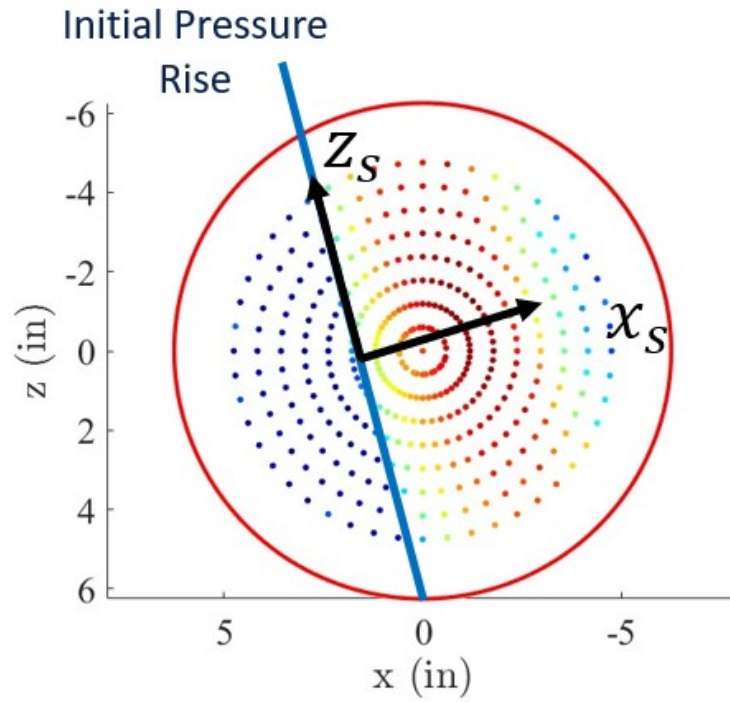**Figure 3.9:** Interpolated C_{p_n} map for all cases studied.

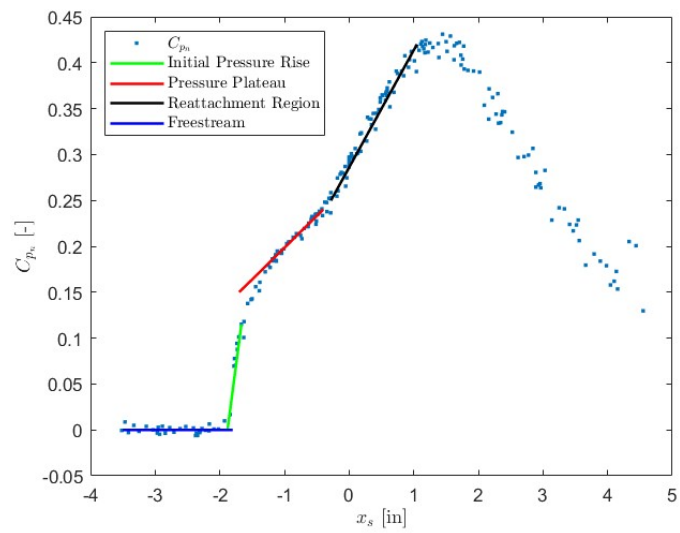**Figure 3.10:** Defines new coordinate system for the C_{p_n} distributions.

Figure 3.11: C_{p_n} distribution with relevant flow features noted.

Table 3.1: Separation Line Sweep Angle.

M_∞ [-]	2.1		2.3		3.0		
C_{p_n} [-]	0.6						0.4
ψ [°]	20	40	20	40	20	40	20
ψ_s [°]	17.47	34.41	15	34	16.70	35.57	15.17

3.2.1 Region of Interest

As previously mentioned, finding the quasi-infinite region is an important step to ensure the results are not skewed by wall or tip effects. Another important aspect of the region of interest is the angle that this information is studied at. Figure 3.12 shows the ROI chosen for each case. The span in the x and z direction is chosen such that the points used to compare pressure data are still within the quasi-infinite region. In future testing, this should be done in a more systematic way using oil flow similar to the Mach 2.1 case. However, for the present study, a region is chosen such that the data collapses well on the pressure distribution. The angle at which the region is rotated is selected using the initial pressure rise. To find this initial pressure rise, Figure 3.11 shows a line that follows the slope of the initial pressure rise. The location of the initial pressure rise for the pressure distribution is chosen such that this line is extrapolated down to the y axis, and the x value where C_{p_n} equals zero is chosen as the onset of the pressure influence. Figure 3.13 shows a comparison of the sweep angle to the angle of the initial pressure rise line for the Mach 2.1, 20° sweep case. This shows that the slopes of the two lines are very similar throughout the interaction, meaning the angle of separation can be interpreted by the angle of the initial pressure rise. To determine the angle the ROI should be set at, the average sweep angle across the ROI of the initial pressure rise line is used. A pressure distribution along the ROI is used determine if the angle is correct for this application. If the angle is correct, the pressure rise along the direction normal to the separation line should occur at approximately the same location across the entire span of the ROI. By looking at each of the pressure distribution figures in this section, it is clear that the angle this method produces is ideal because all the data points picked from the ROI form a strong collapse for each case. Table 3.1 shows this separation angle found from the initial pressure rise for each case with the results from ISWT as well. It is noted that the separation angles are close between tunnels, but the separation angle in APWT is higher. Specifically for the 20° case at Mach 2.1, the sweep angle is averaged over an area where the sweep is is approaching 20°. The sweep angle is shown to be cylindrical, but the average sweep across the chosen ROI is slightly less than 20°, making the interaction look conical. It is likely that the same is true for the 20° cases at Mach 3.0, but further analysis is required to support this claim.

In the ROI for each case, the C_{p_n} along the normal direction of the separation angle is plotted to match the 2-D pressure distribution as shown in Figure 1.2. This method allows for a pressure rise that occurs at the same location across the span of the interaction, thus allowing for a similar analysis of this data that accounts

(a) $M = 2.1, \psi = 20°, C_{p_n} = 0.6, p_0 = 45psi$

(b) $M = 2.1, \psi = 40°, C_{p_n} = 0.6, p_0 = 46psi$

(c) $M = 3.0, \psi = 20°, C_{p_n} = 0.6, p_0 = 90psi$

(d) $M = 3.0, \psi = 40°, C_{p_n} = 0.6, p_0 = 90psi$

(e) $M = 3.0, \psi = 20°, C_{p_n} = 0.4, p_0 = 88psi$
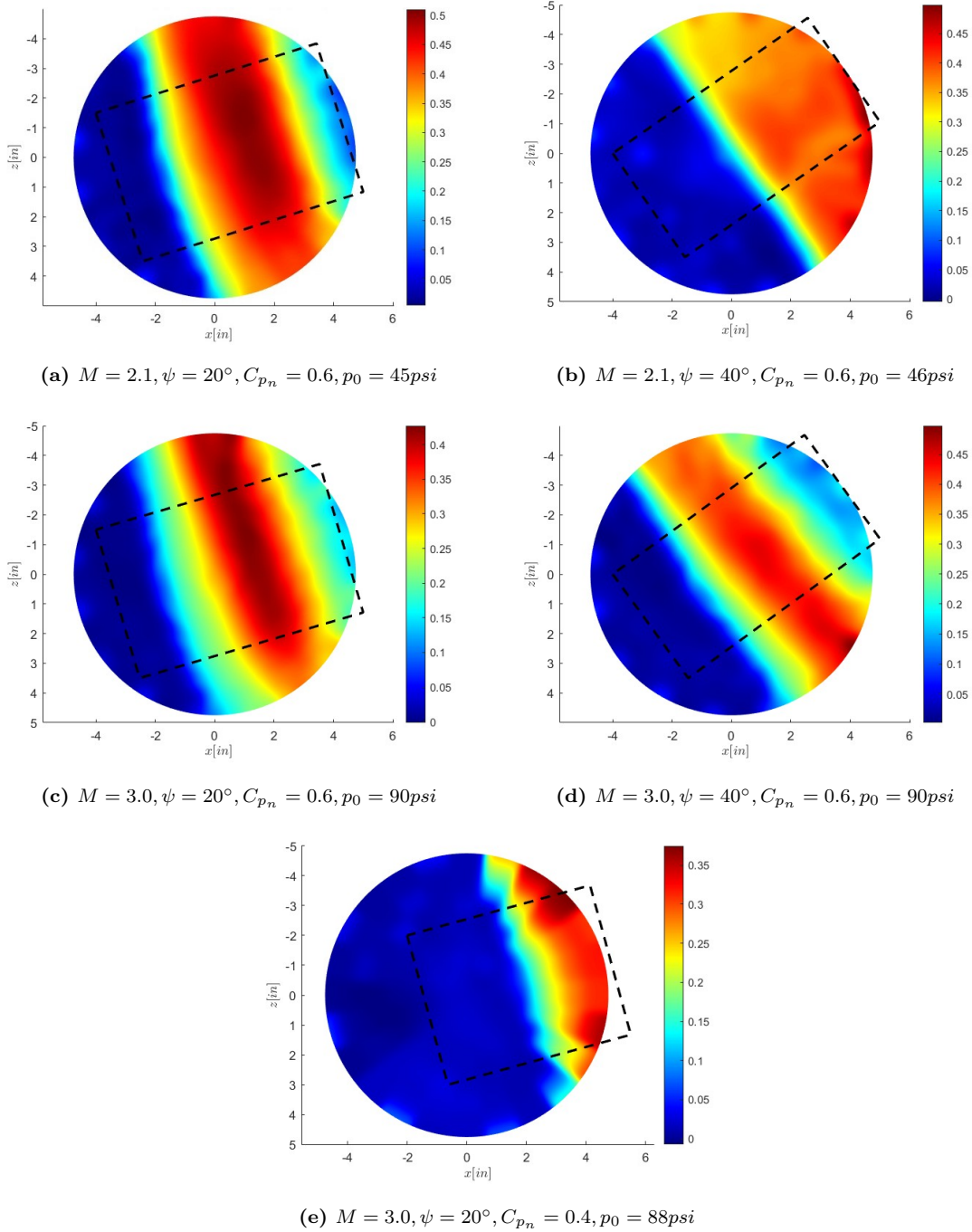
Figure 3.12: Region of interest for all cases.
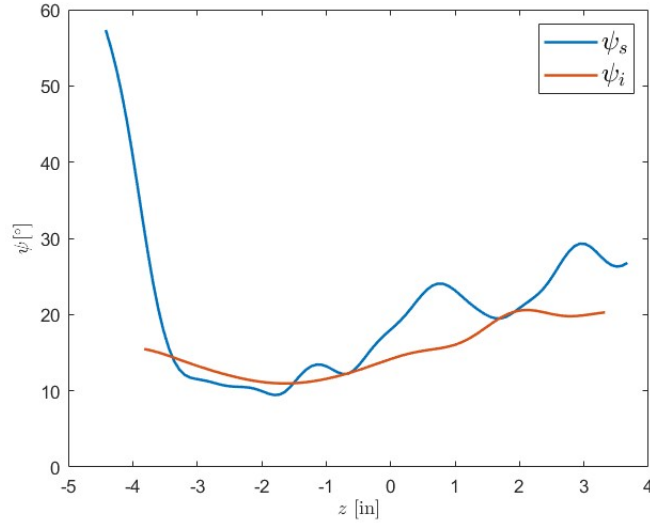
Figure 3.13: Comparison of sweep angle of the separation line (ψ_s) and the initial pressure rise line (ψ_i).

for the sweep of the interaction. Some spreading of the data can be seen towards the downstream section of the interaction, especially in higher sweep cases. This is due to the difference between the separation and reattachment shock angles, but this is minimal and to be expected with the conical shape of the interaction during the first part of the interaction near the root.

3.2.2   Varying Sweep

To further support the location of the separation and reattachment found with oil flow visualization for the Mach 2.1, $\psi = 20°$ case, Figure 3.14 shows these features in relation to the pressure distribution along the region of interest. The pressure plateau region of this interaction is only slight, which could be due to unsteady motion in the interaction causing the mean pressure profile to appear less separated as explained by Souverein et al. (2013). However, the location of separation and reattachment align well with theory as the separation location occurs just in front of the first change in slope of the distribution, and the reattachment line occurs just in after of the second increase in slope of the distribution. Further, it is shown that the location of the inviscid expansion occurs just behind the drop in pressure.

For the Mach 2.1 cases, Figure 3.15 shows the C_{p_n} distribution in the respective ROI for the $\psi = 20°$ and $\psi = 40°$ cases. To best compare between different sweep angles, the x location of each distribution is shifted such that the initial pressure rise (the green line in Figure 3.11) corresponds to zero on the x-axis. Further, as will be discussed in the aspect ratio comparison section, the x-axis is scaled with the boundary layer height to best compare between cases in the different tunnels. Using the C_{p_n} scaling, pressure rise across different sweep angles should overlap outside of the separation region. In Figure 3.15, it is noted that the pressure rise for the 40° case does not reach the same value as the 20° case. This could be due to the
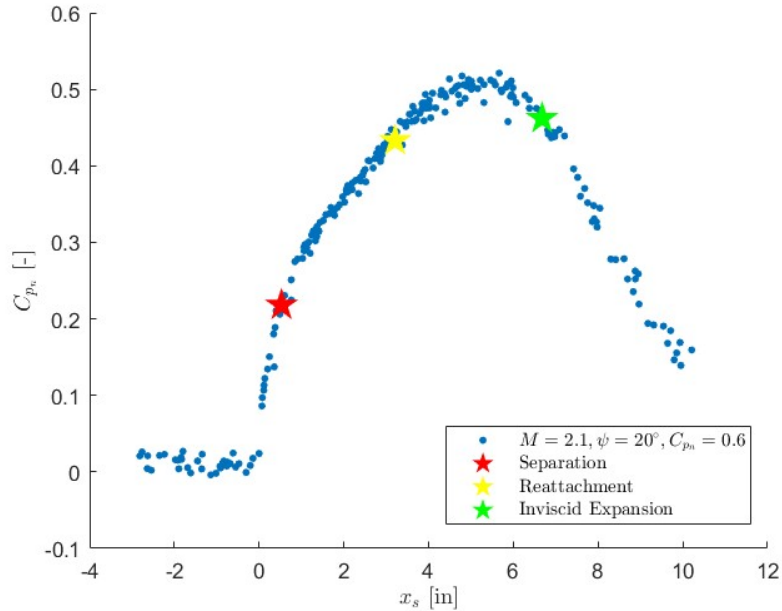
Figure 3.14: Mach 2.1, $\psi = 20°$ C_{p_n} distribution with separation, reattachment, and inviscid expansion locations.

expansion fan being too close to the interaction, or simply viscous factors that are not accounted for when determining the pressure rise across the shock for these experiments. However, work by Vitols (2024) shows this pressure rise becomes constant when using C_{p_n} to comare different sweep cases. It is therefore concluded that the location of the impinging inviscid expansion fan in relation to the rest of the interaction. Looking at Figure 3.9, it is clear the expansion fan lands much closer to the interaction than in the rest of the cases. This is believed to cause the pressure rise to stall, and would explain the lack of any indication of separation. Padmanabhan (2023) and Vitols (2024) found that the results of the 40° cases do not indicate separation, but the normal pressure rise still matches the final pressure downstream of reattachment. Further, a slight change in slope indicative of some influence of the impinging shock still occur, whereas this case almost looks like an inviscid pressure rise which could be physical for this interaction, but further investigation of this is required before stating that the 40° case at Mach 2.1 behaves in this manor.

Comparison of sweep cases in Mach 3.0 flow are done similarly to the Mach 2.1 cases as shown in Figure 3.16. For the 20° sweep, a clear pressure plateau indicates separation. The 40° case shows some change in pressure rise at a similar location in the x direction, but it is very minimal and is indicative of a case with no separation. The pressure rise for each $C_{p_n} = 0.6$ case also reaches a similar maximum C_{p_n} value, further supporting the hypothesis that the expansion for the Mach 2.1, 40° case interferes with the interaction and causes pressure not to reach its peak value. With the 20° case separating and the 40° case not separating, this suggests at the tested C_{p_n} the sweep that causes separation is between $\psi = 20°$ and $\psi = 40°$ which is consistent with results by Padmanabhan (2023) and Vitols (2024).
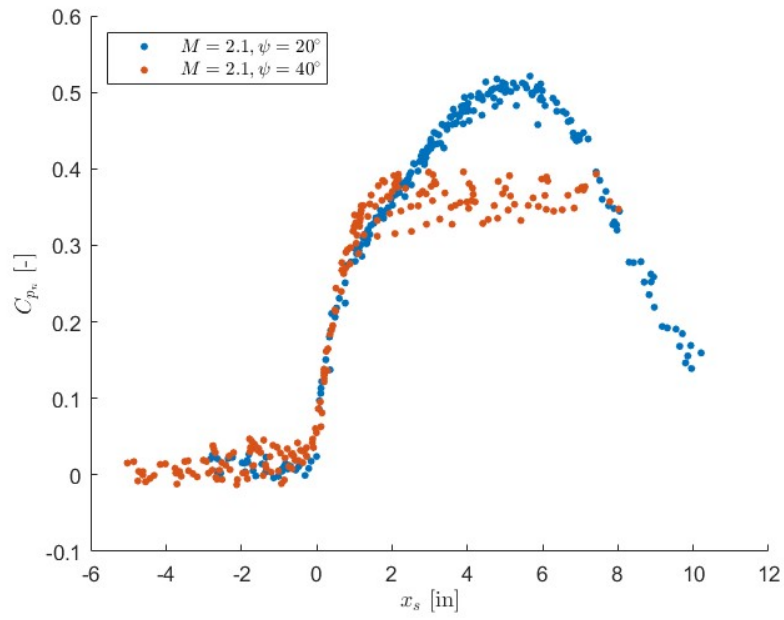
Figure 3.15: C_{p_n} distributions for Mach 2.1 cases.
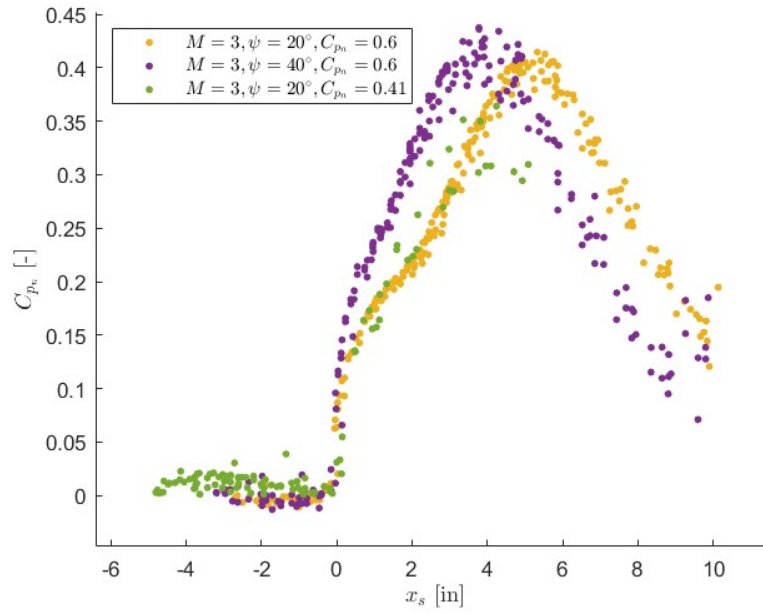
Figure 3.16: C_{p_n} distributions for Mach 3.0 cases.

3.2.3   Varying Mach number

Comparing the sweep cases across Mach number is used to isolate the effects of Mach for each case. In addition to this, a comparison of the effects of varying C_{p_n} can be determined as well. First, looking at the 20° sweep cases, the unit Reynolds number is $3.85 \times 10^7 \frac{1}{m}$ and $4.88 \times 10^7 \frac{1}{m}$ for the Mach 2.1 and Mach 3.0 cases respectively, limiting any effects the change in Reynolds number could have on the interaction. It is noted that the maximum C_{p_n} achieved for the Mach 2.1 case is higher than the pressures seen by the other two cases (although the pressures for the $C_{p_n} = 0.41$ case could get higher further downstream of the plug where data wasn't taken). Looking at the two Mach 3.0 runs, the pressure distributions follow a very similar trend in the initial portion of the interaction which follows the Free Interaction Theory as proposed by Chapman et al. (1958). Chapman proposed that the separation resulting from a shock is influenced by both the Reynolds number and the Mach number of the freestream. Equation 3.1 shows this relation as presented by Xue et al. (2023) where C_{f0} is the skin friction coefficient affected by Reynolds number, and $F(\bar{x})$ is a universal corelation factor in which a few different values have been proposed across the literature (Erdös et al., 2011; Giepman et al., 2018; Matheis and Hickel, 2015; Zhenguo et al., 2015; Tao et al., 2014). Due to the Reynolds numbers being similar for the two Mach numbers here, and the pressure rise in the interaction is inversely proportional to the Mach number, it would follow that the pressure rise is higher for the lower Mach case and that the interaction is driven more by the Mach and less by the difference in Reynolds number between cases.

$$\frac{p}{p_\infty} = 1 + F(\bar{x})\sqrt{\frac{C_{f0}}{2(M_\infty{}^2 - 1)^{1/2}}} \tag{3.1}$$

Chapman et al. states that pressure rise in the initial interaction region is determined by Mach number and Reynolds number and not the downstream influences of pressure. This means that the pressure rise the boundary layer can withstand before separating should be independent of the strength of the shock, thus stating that the initial shape of the C_{p_n} distributions would be similar similar across all C_{p_n} values for similar Mach numbers. With the limited streamwise data, it is unclear what occurs further along this pressure distribution, but these (Figure 3.17) follow this trend for the data that was collected. A final takeaway of these results suggest that the separation is stronger at the higher Mach number. This could be due to the stronger pressure gradient across the shock for the Mach 3, where $p_3/p_\infty = 3.28$ and $p_3/p_\infty = 2.25$ for Mach 3.0 and 2.1 respectively. This could suggest that the pressure plateau is more dependent on the pressure rise across the reflected shock than on C_{p_n} or C_p.

For the 40° case, as previously mentioned, it is expected that the Mach 2.1 data is influenced more than the rest of the cases by the expansion fan of the shock generator. Figure 3.18 further supports this by showing that the Mach 2.1 case has no indication of a pressure plateau, and Free Interaction Theory would suggest this pressure rise should be higher for the lower Mach number case. However, the trend of the higher Mach number having a stronger separation still holds true in this case. Following the pressure distribution
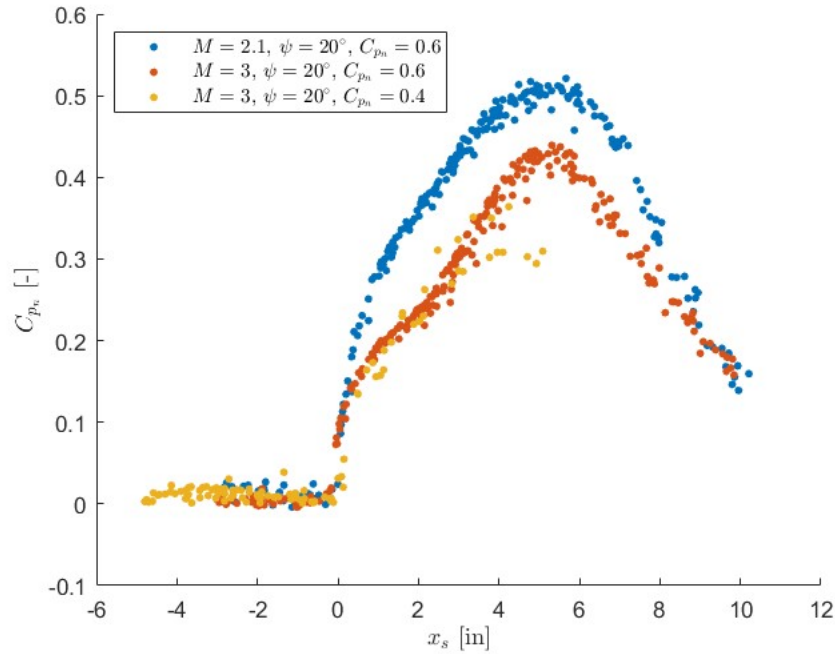
Figure 3.17: C_{p_n} distributions for $\psi = 20°$ cases.

of the Mach 2.1 data, the initial pressure rise does match well until the influence of the pressure rise causes the Mach 3.0 distribution to begin to plateau slightly.

3.2.4 ISWT Comparison

Comparing data from ISWT adds several new variables, all of which could change the result of the mean flow properties in ways that cannot be explained by changing too many variables at once. Comparing the data taken in APWT to the data taken in ISWT can further support the results from each set of experiments, but it is important to note that the aspect ratio, Reynolds number, Mach number, and shape factor of the boundary layer all have an effect on the interaction, and differences between tunnels' data could be a result of any number or all of these factors. This means that only qualitative information should be taken from the comparison between these tunnels, and any quantitative information would need further validation by better isolating specific variables between tests. For this comparison, comparing similar sweeps for each case offers the best way to compare the two tunnels. Figure 3.19 shows the pressure distribution for the 20° cases in APWT and ISWT. The cases in APWT and ISWT are aligned the same way as previously explained in which the line fit over the initial pressure rise is set to cross the x axis at zero. Referring again to Equation 3.1, the pressure rise is a function of the skin friction coefficient. Interestingly, while the Reynolds number for the Mach 2.3 case is much lower than the other two cases, the values of skin friction are very similar between the two tunnels at 2.6×10^{-3} and 2.0×10^{-3} for APWT and ISWT respectively (although the margin of error for the value for APWT is much higher than the ISWT value, so this should be taken
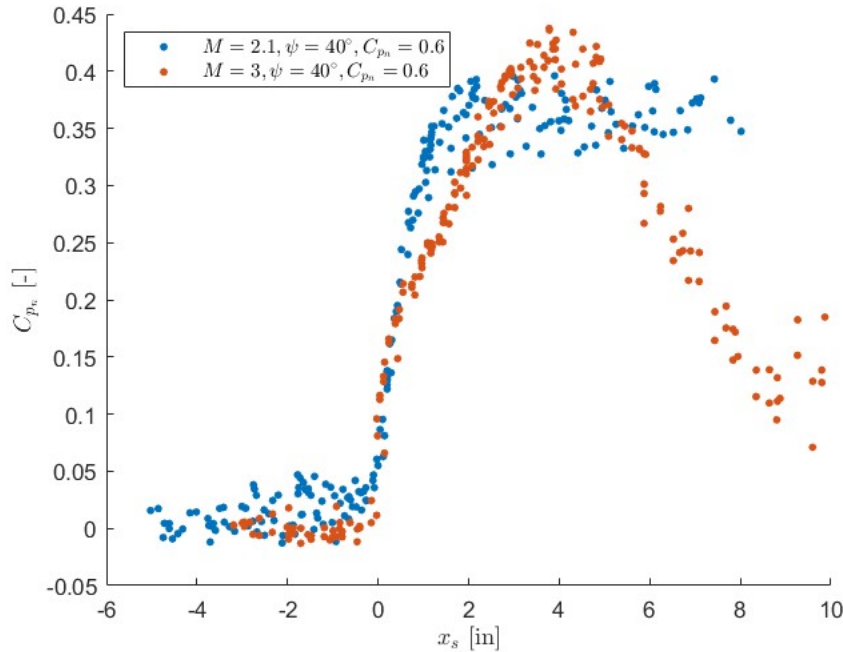
Figure 3.18: C_{p_n} distributions for $\psi = 40°$ cases.

into consideration when comparing the two values). So, it would follow that the pressure distribution would be more dependent on Mach number between the three cases shown. Figure 3.19 follows this trend quite well for the initial pressure plateau region of the pressure distribution as the lower Mach numbers begin to plateau at higher C_{p_n} values compared to the higher Mach numbers.

Looking at Figure 3.20, the pressure distributions for these cases show very good agreement. For the Mach 2.3 and Mach 3.0 cases, there is a slight change in the slope of the pressure rise around $C_{p_n} = 0.3$ and $C_{p_n} = 0.2$ respectively, but each case shows that separation is very unlikely for these cases. If the trends for the 20° case were to apply to this case as well, it would be expected that the pressure rise for Mach 2.1 would be also be the highest for this case. Because the pressure rise is very sudden, does not reach as high of a C_{p_n}, and has no indication of a slope change during the pressure rise, this further indicates that the expansion fan is likely interfering with the interaction.

3.3 Heat Flux Measurements

The final method of characterizing the mean flow topology is heat flux measurements. The heat flux is used as a way to determine the location of the initial pressure rise and the separation location. However, this method does not prove the existence of separation, but only helps verify the location of the initial pressure rise and separation. This is very beneficial in the 20° cases in these tests that have been shown to separation
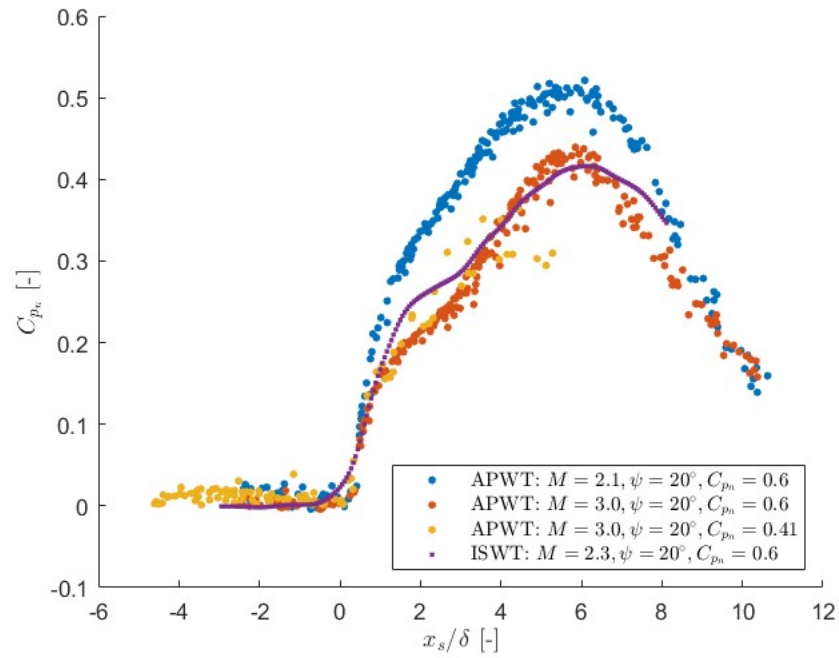
Figure 3.19: C_{p_n} distributions for $\psi = 20°$ cases across both tunnels.
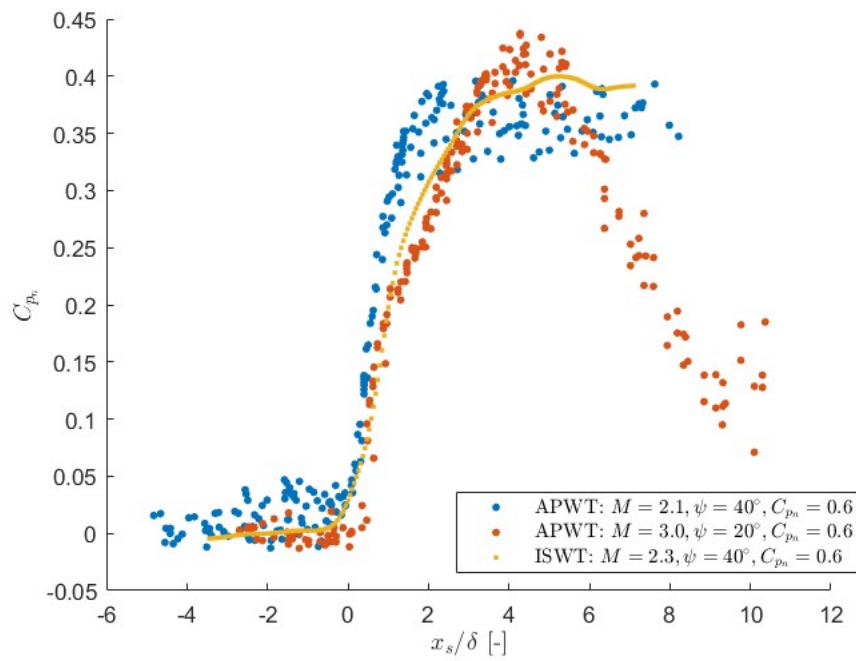
Figure 3.20: C_{p_n} distributions for $\psi = 40°$ cases across both tunnels.

in previous work (Vitols, 2024; Padmanabhan, 2023), but no oil flow is data is available to determine this separation location.

3.3.1 Adiabatic Wall Temperature

To determine Stanton number, it is first important to determine the adiabatic wall temperature for these experiments. By determining the adiabatic wall temperature from the heat flux measured by the camera, a comparison to the theoretical value predicted by assuming a turbulent boundary layer can be made to further support the results of temperatures measured by the camera. Assuming the change in wall temperature has a minimal change in the Stanton number, heat flux measurements at multiple plug temperatures allows for the determination of the adiabatic wall temperature by plotting the heat flux and temperature, then using a linear regression to fit a line through the data to extrapolate at what wall temperature heat flux would be zero. The confidence in this method produces a large range of possible adiabatic wall temperatures with the given heat flux measurements due to the large variation in the heat flux throughout the run and therefore requires further validation. This result will be discussed later in this section.

When calculating Stanton number, adiabatic wall temperature can be found by using the recovery factor as discussed by Wimbrow (1949). Wimbrow states that recovery factor is well represented by $Pr^{\frac{1}{3}}$ in the freestream boundary layer. For the current study, this is estimated to be 0.896. Recovery factor and the relation to adiabatic wall temperature is defined as shown in Equation 3.2. It is noted that the recovery factor is constant, but it is a function of total temperature and and freestream temperature, which are not constant in these experiments. To account for this, Equation 3.2 is multiplied by $\frac{1/T_0}{1/T_0}$ to give Equation 3.3 which has a constant r value, and therefore should also have a constant $\frac{T_{aw}}{T_0}$ value because the ratio of total temperature and static temperature of the freestream is only a function of Mach number and the specific heat ratio which are constant. Finally, this allows for the Stanton number at each time step to be calculated using Equation 3.4 where T_∞ is calculated from the total temperature at each time step. For the Mach 3.0 cases, the total temperature is known and used to normalize the wall temperature. Results are shown in Figure 3.21c and show good agreement with a recovery factor of 0.901 in the boundary layer.

$$r = \frac{T_{aw} - T_\infty}{T_0 - T_\infty} \tag{3.2}$$

$$r = \frac{\frac{T_{aw}}{T_0} - \frac{T_\infty}{T_0}}{1 - \frac{T_\infty}{T_0}} \tag{3.3}$$

$$St = \frac{q_w}{(\frac{T_{aw}}{T_0}T_0 - T_w)\rho_\infty u_\infty C_p} \tag{3.4}$$

Results for Mach 2.1 require more assumptions due to the unknown total temperature of the run. The adiabatic wall temperature is heavily dependent on the total temperature in this situation; much more than

that of the changes in heat flux values associated with the rear temperature of the plug. Figure 3.21 shows the raw heat flux measurements taken in similar locations in the boundary layer as the Mach 3.0 data is. The temperatures are normalized by a constant total temperature across each case in Figure 3.21a. This shows that the data does not align well to form a linear relation as the Mach 3.0 data did. Therefore, to produce an accurate adiabatic wall temperature, a more accurate total temperature is required and must be estimated. To achieve this, a small group of points in the boundary layer are chosen from each run to represent the boundary layer in the constant heated region of the plug. The values of the total temperature for each run are then adjusted such that the recovery factor in the freestream equates to 0.892. This adds a very likely error due to the unknown slope of the linear regression between the cases. By adjusting the total temperature, it is possible to get a steeper or more shallow slope without adjusting the measured heat flux and achieve the same recovery factor. To help minimize the unknowns caused by this process, the change in total temperature across each run is kept at $-1.2°$C per second as discussed previously. The runs with a more spread out grouping across temperature likely had a higher total temperature drop during the run compared to the more tightly packed groups, but this is not accounted for to prevent further biasing results. The uncertainties caused by this process are unavoidable, but an important aspect in achieving a realistic adiabatic wall temperature profile. The results from this section should be taken as qualitative and less so quantitative. Higher uncertainty associated with temperature measurement, heat flux measurement, and total temperature estimations offer useful preliminary results, but will require further validation before conclusions can be drawn from quantitative results.

An example of the adiabatic wall temperature and recovery factor profile extracted from this method is shown in Figure 3.22. Results here are consistent with those found by Vitols (2024) and Gross et al. (2018) which found that the recovery factor near the initial pressure rise increases to nearly one. An image of the St for all five cases is shown in Figure 3.23.

3.3.2 Stanton Number distribution

The uneven heating of the plug made it difficult to determine an accurate St for the entire surface. Due to the predicted difference in the rear temperature profile compared to the pre-run temperature discussed previously, there is a "ring" of higher St values which is not a physical property of the flow. As a result, it is important to pick a region within the area that is unaffected by this artificial spike in St to best visualize the results. The ROI for the Stanton number distribution is slightly different than the mean pressure ROI. Figure 3.24 shows an example of the region of interest for the St distribution, and the plotted values from this ROI for a partial and full ROI. Due to the uneven plug heating, using the entirety of the ROI selected from the mean pressure data smooths over much of the important feature of the St trace (Figure 3.24d). To account for this, a smaller section in the center of the ROI for the mean pressure distribution is used to attain the St trace as shown in Figure 3.24b. For the ROI, the black squares are the spatial calibration points that have been removed to ensure no artificial peeks or valleys in the data occur from these locations.
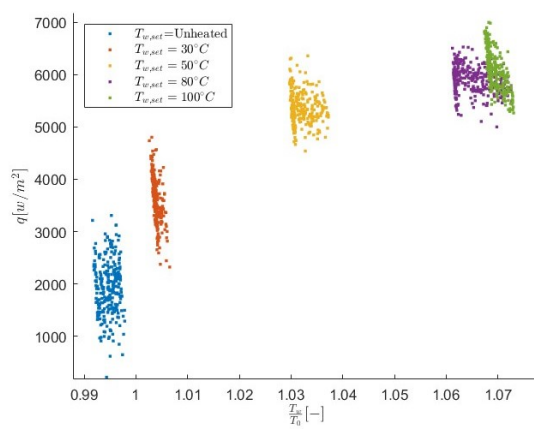
(a) Constant total temperature distribution between runs at $M = 2.1$.
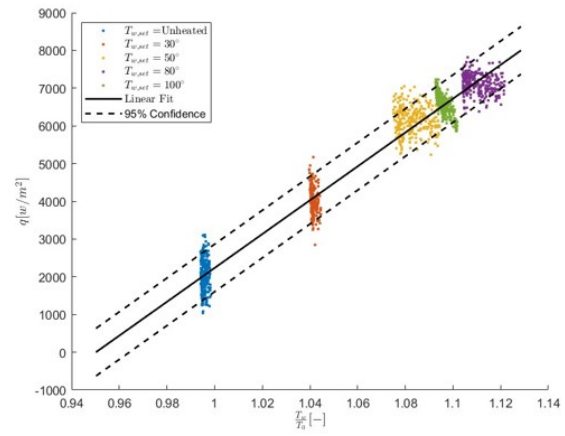
(b) Adjusted total temperature distribution between runs for $M = 2.1$.
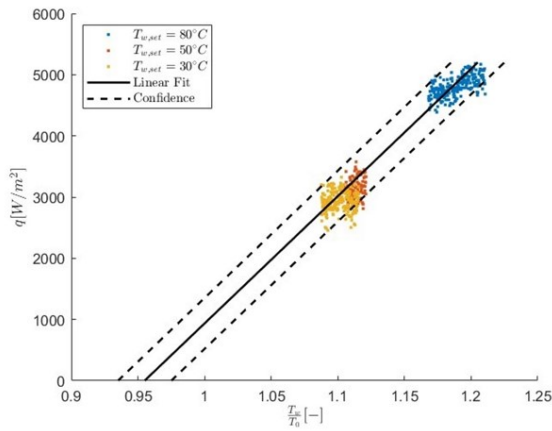
(c) Total temperature distribution between runs for $M = 3.0$.
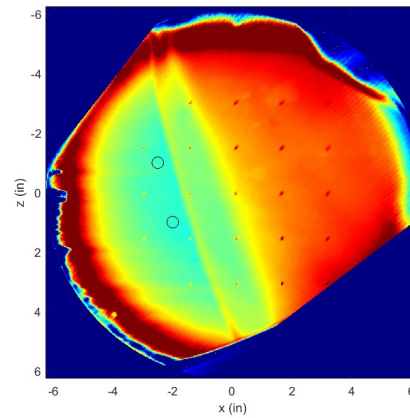
(d) Location of freestream data used for each case.

Figure 3.21: Comparison of the adjusted and unadjusted heat flux data for $M = 2.1$ in the freestream boundary layer with wall temperature normalized by a total temperature and the heat flux data for $M = 3.0$ using the measured total temperature for each $M = 3.0$ run.

(a) T_{aw} for $M = 2.1$

(b) T_{aw} for $M = 3.0$

(c) Recovery factor for $M = 2.1$

(d) Recovery factor for $M = 3.0$
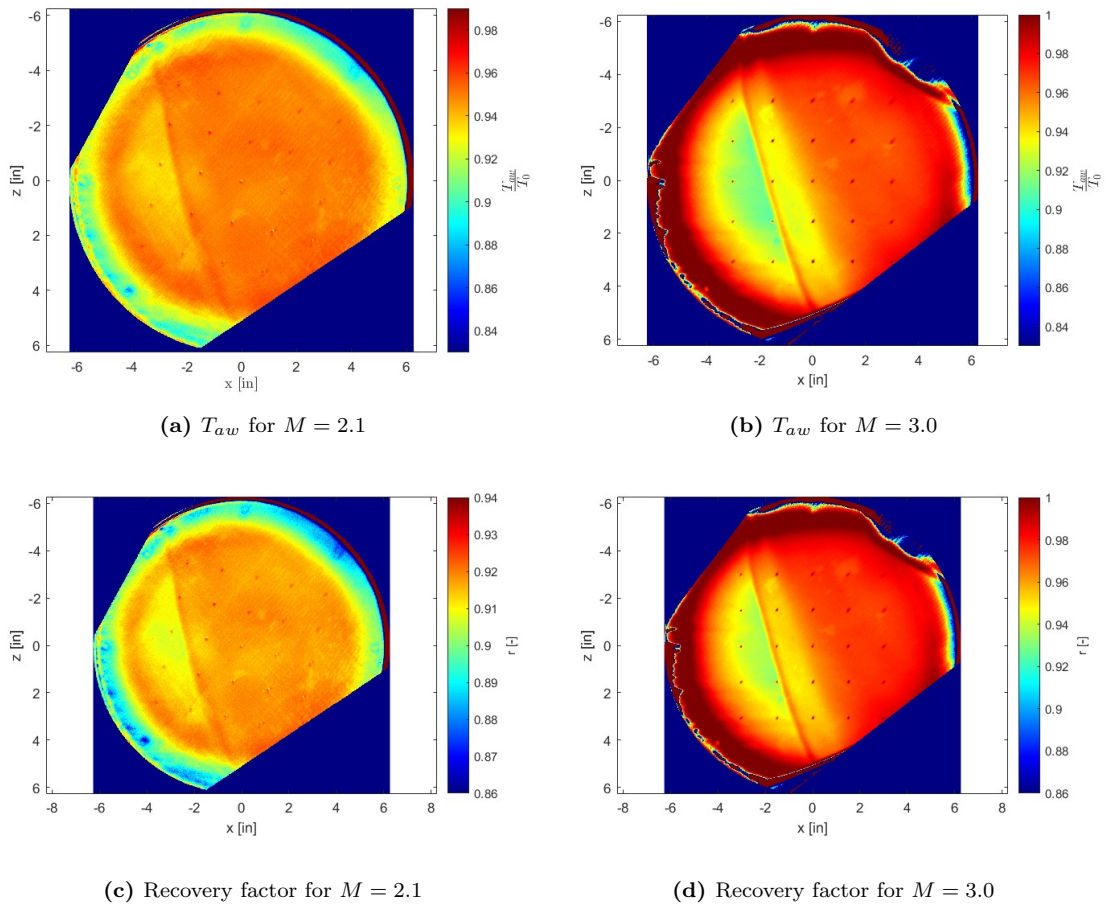
Figure 3.22: Adiabatic Wall Temperature and recovery factor for $\psi = 20°$ cases at Mach 2.1 and Mach 3.

(a) Stanton number for $M = 2.1, \psi = 20°, C_{p_n} = 0.6$

(b) Stanton number for $M = 2.1, \psi = 40°, C_{p_n} = 0.6$

(c) Stanton number for $M = 3.0, \psi = 20°, C_{p_n} = 0.4$

(d) Stanton number for $M = 3.0, \psi = 20°, C_{p_n} = 0.6$

(e) Stanton number for $M = 3.0, \psi = 40°, C_{p_n} = 0.6$
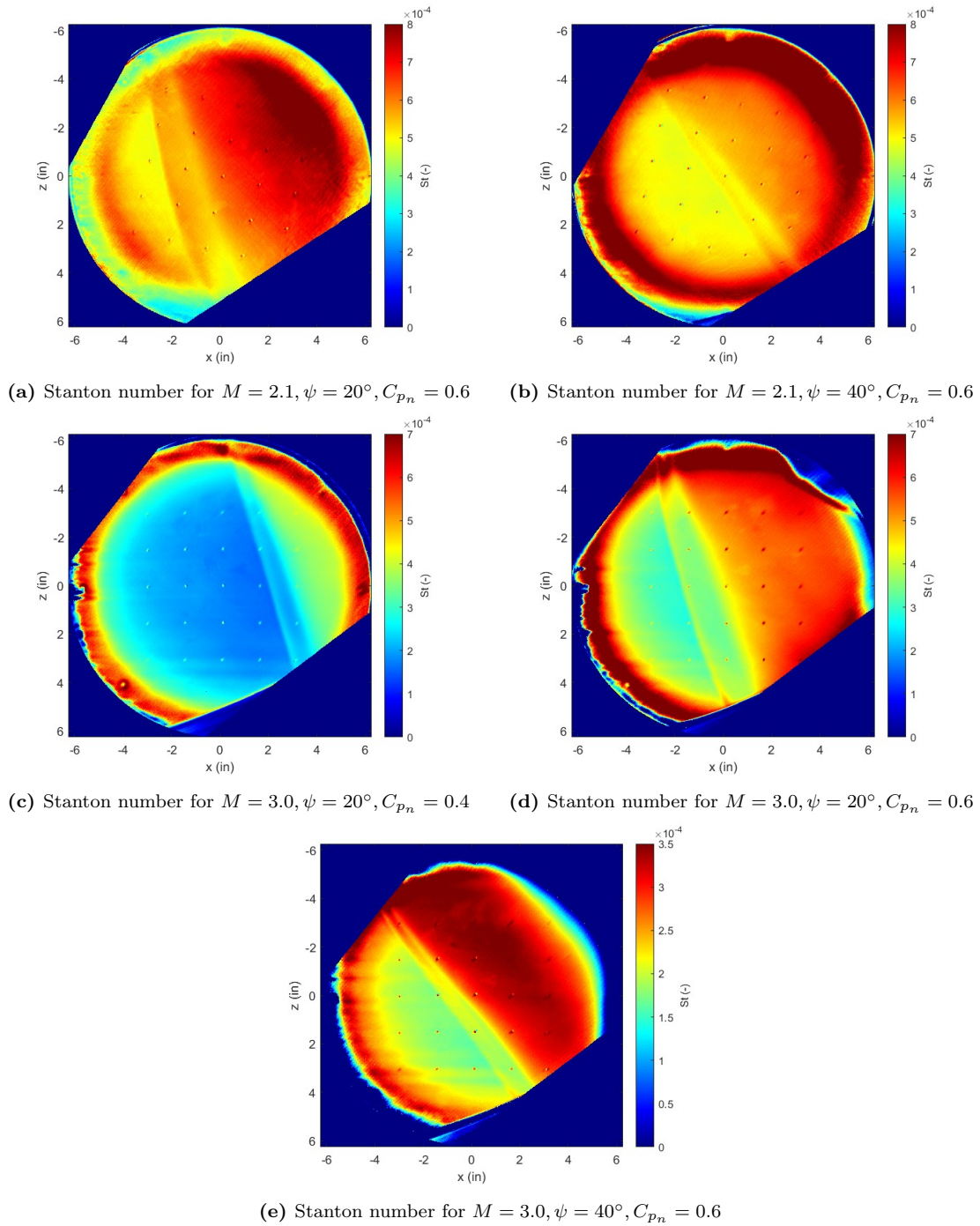
Figure 3.23: Plot of the Stanton Number for all cases.

(a) Smaller ROI used for St trace.

(b) St trace attained from smaller ROI.

(c) Full ROI from mean pressure distribution.

(d) St trace attained from full ROI.
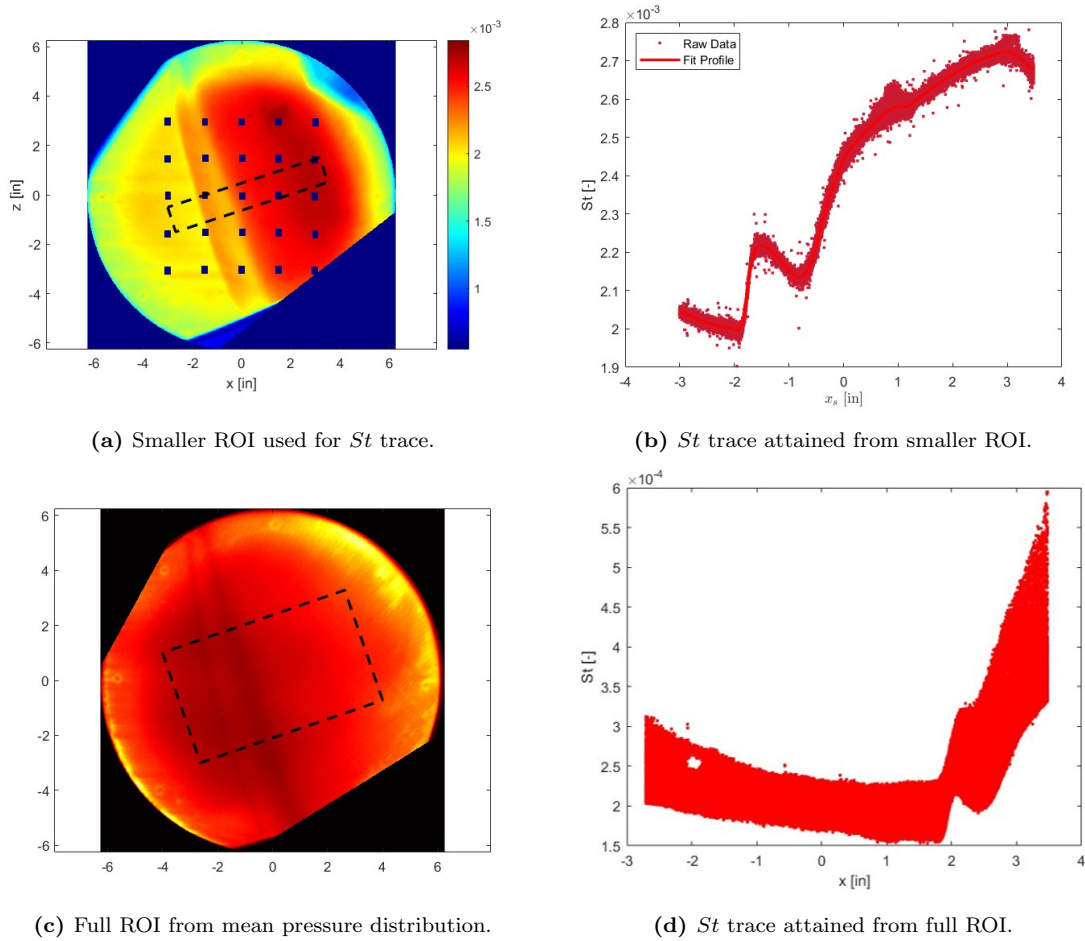
Figure 3.24: Stanton number distribution for full and partial ROI.

In the St distribution, the point values represent results within the ROI, and the solid red line is the mean value at each x location traced over the data to better visualize the results and to be used for a comparison between IR measurements and mean pressure measurements.

From this nonuniform profile, it is important to determine that the results inside this ring of uneven heating are reliable. The St should be constant along the plug if there were no SBLI on the surface, and therefore should be constant upstream of the SBLI. If the chosen ROI offers accurate results, St values upstream of the interaction should be a constant value. Figure 3.31, Figure 3.32, Figure 3.33, Figure 3.34, and Figure 3.35 show the St distribution for all run configurations overlapped with the pressure distribution. These show some error associated with the ring of higher St values discussed previously, but many of these values have relatively uniform St values upstream of the first drop in St. Further, by noting the uniform values of Figure 3.35 upstream of the initial pressure rise, it is seen that in the constant heated region, confidence in the St values are higher compared to the outer region of the plug. Thus, the values near the initial pressure rise and downstream of the initial pressure rise are in the region of high confidence. Still,

the values from this are taken more qualitatively than quantitatively as much of the upstream results show a steady decrease in St where it should be constant.

3.4   Measurement Comparison

A comparison of the oil flow visualization, Stanton number, and mean pressure data leads to further insight about the flow features for the Mach 2.1 flow. While oil flow was not able to be collected for the Mach 3.0 cases, a comparison of the lower Mach number validates flow features and allows one to infer what is happening at the higher Mach numbers. By overlaying each of the methods, it helps the reader visualize what each of the important aspects of the flow are for the different methods. This is particularly useful for the Stanton number images as the double minima along the sweep angle is not very intuitive. The associated error in the location of these images in relation to one another is small, but could offer potential error due to the required image transformation from the raw image to a 2-D image. As a check, each method utilizes the same plug port in the wind tunnel, and the edge of the plug is checked to overlap for each case to ensure the location of the data is as expected.
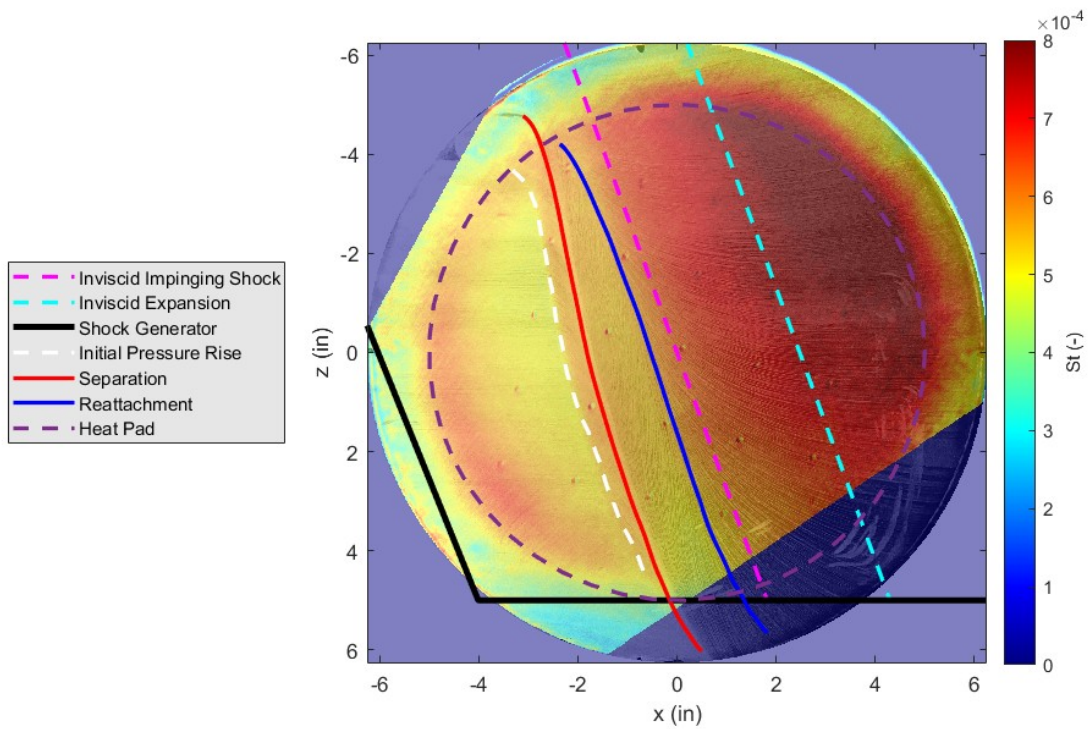
3.4.1   Oil Flow and Stanton Number

Stanton number is compared to oil flow by overlaying the two images as seen in Figure 3.25 and Figure 3.26. Looking at these flow features in relation to the Stanton number image is useful to help visualize what the Stanton number distribution represents. However, it is difficult in the present configuration to see the Stanton number features in relation to the flow features due to the relatively faint oil flow features compared to the Stanton number image. Thus, as an aid to this comparison, flow features are shown in one image and excluded in the other (Figure 3.25, Figure 3.26) to better understand the flow features of the Stanton number images.

For all cases, the first Stanton minima occurs at the initial pressure rise which is consistent with the results found by Hayashi et al. (1986). Comparing this St image with oil flow, the first indication of change in flow direction also appears at this local Stanton number minima. Figure 3.25 and Figure 3.26 show the initial turn in the oil flow aligns well with the overlapped IR image. This trend is very clear in Figure 3.25 in which the initial pressure rise occurs just in between the St change in magnitude, which is shown to be the local minima in these experiments. Figure 3.3 also shows good agreement between methods as the change in direction of the oil flow only occurs once the initial pressure rise occurs. This is in good agreement with results from ISWT. Figure 3.30 shows the mean pressure contour plotted over the Stanton number. Isolating just the region of interest outlined in the dotted black line, the first local Stanton number minima also occurs at the initial pressure rise.

A line can be plotted across the span of the interaction at both the local minima of the initial pressure rise and the local maxima of the separation line for each case. Figure 3.28 shows the precision of this method for the Mach 2.1 data and the Mach 3.0 data, but the lines plotted using this data are smoothed using a kernel

Figure 3.25: Stanton Number and oil flow visualization comparison for 20° sweep case at Mach 2.1.
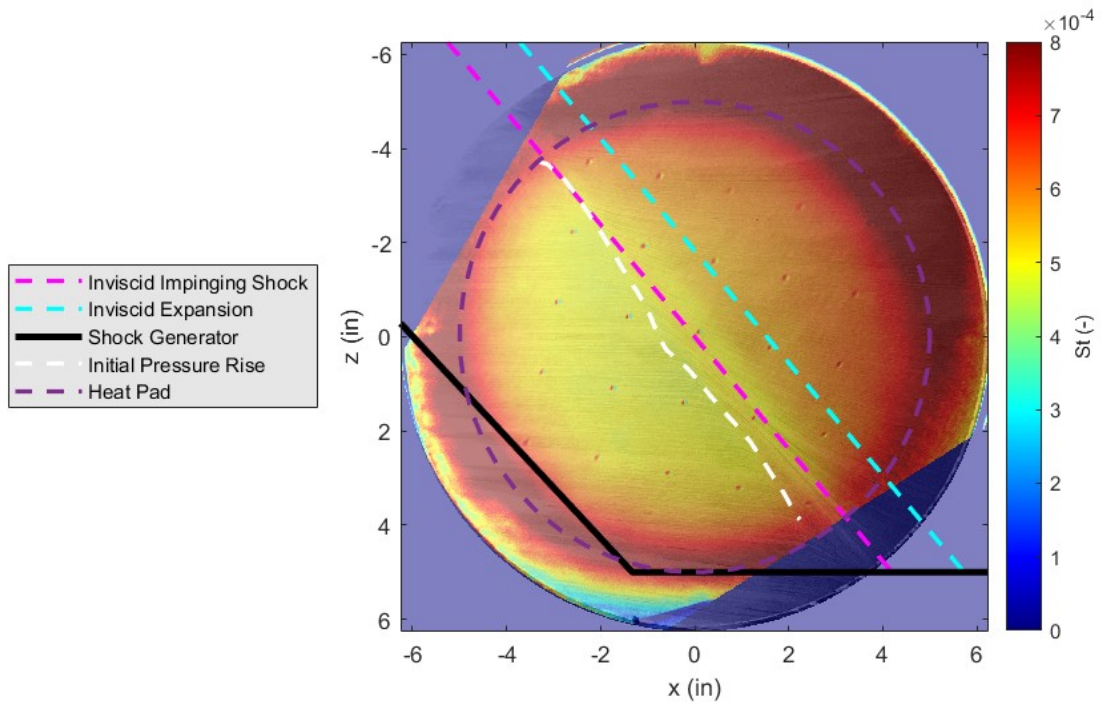
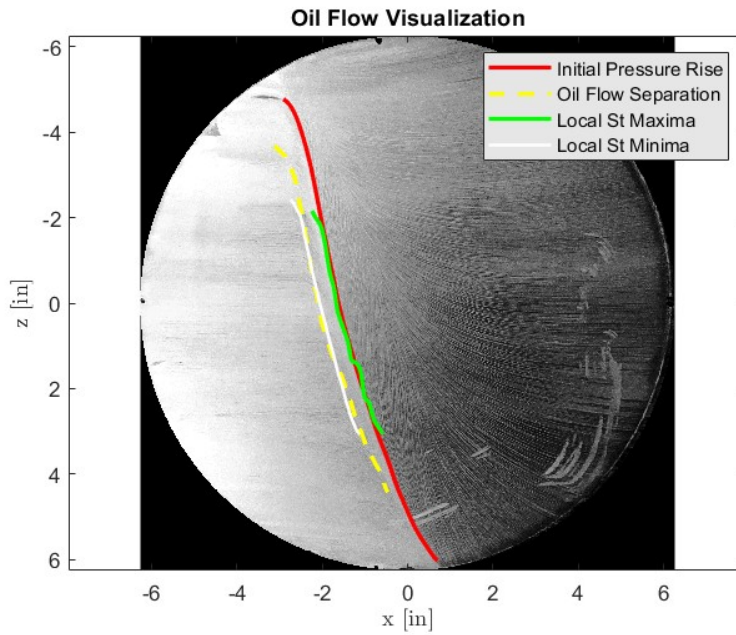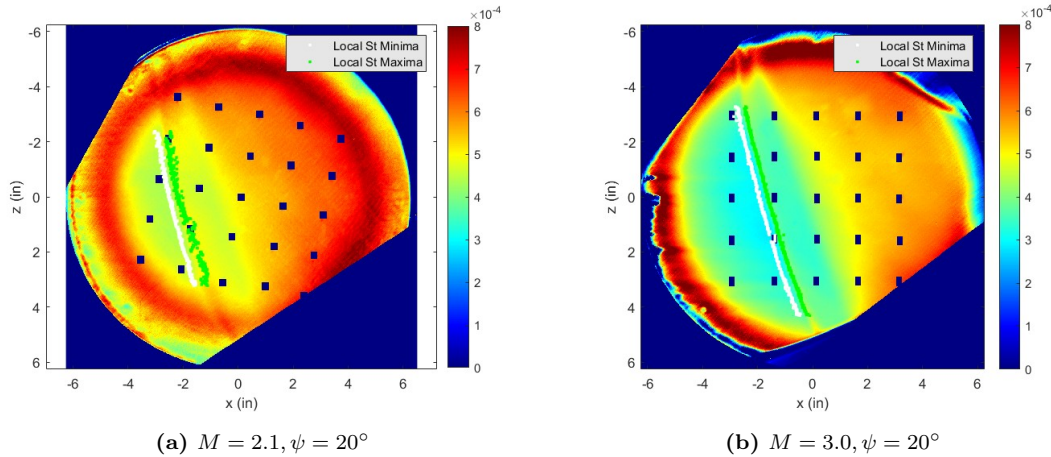**Figure 3.26:** Stanton Number and oil flow visualization comparison for $40°$ sweep case at Mach 2.1..

Figure 3.27: Comparison of separation and initial pressure rise locations between various methods.

**(a)** $M = 2.1, \psi = 20°$ **(b)** $M = 3.0, \psi = 20°$

**Figure 3.28:** Points found along span for the local St maxima and minima.

smoothing regression. However, because these features are present in separated and attached interactions, this is only done for the 20° cases, but not for the 40° cases which show no signs of separation based on the oil flow and mean pressure data. Figure 3.27 shows the oil flow image with the initial pressure rise found from the mean pressure data plotted, as well as the initial pressure rise and separation found from the St images. These show good agreement in the location of the initial pressure rise found from both methods, as well as good overlap of the separation line from the oil flow image and the separation found from the St image. This characterization shows that the initial pressure rise and separation location can be found for the Mach 3.0 cases with reasonable confidence in the location this method indicates. These results are shown in Figure 3.38, Figure 3.39, and Figure 3.40.

The second local feature is the local maxima in the St distribution. This maxima correlates well with the location of the separation as can be seen in Figure 3.25 where the separation line shown in blue aligns with peak St value. This is better visualized by Figure 3.29. This figure shows very good agreement with the maximum St value along the span (green line) and the separation line (red line). Figure 3.31 further shows this trend in which the location of the separation line falls directly over the local Stanton number peak.This result is also confirmed by Hayashi et al. (1986) for the unswept case, which found that the local St maxima aligned well with the separation line. For the Mach 3.0 data, this is supported by comparing the location of the initial pressure rise and the local peak heating. Due to the initial pressure rise being just upstream of separation and following the separation sweep angle closely, this peak heating should be just downstream of the initial pressure rise. This is confirmed for the Mach 3.0 cases in Figure 3.33, Figure 3.34, and Figure 3.35.

Figure 3.31, Figure 3.32, Figure 3.33, Figure 3.34, and Figure 3.35 show the overlap of the St distribution and the mean pressure distribution for each case. For this data, information on the location of the important flow features can be extracted. To create these plots, separate scales on the y axis are used between each as the Stanton number between runs varies. The initial pressure rise, separation, and reattachment lines are plotted for each case using the St distribution from local maxima and minima that have been described.
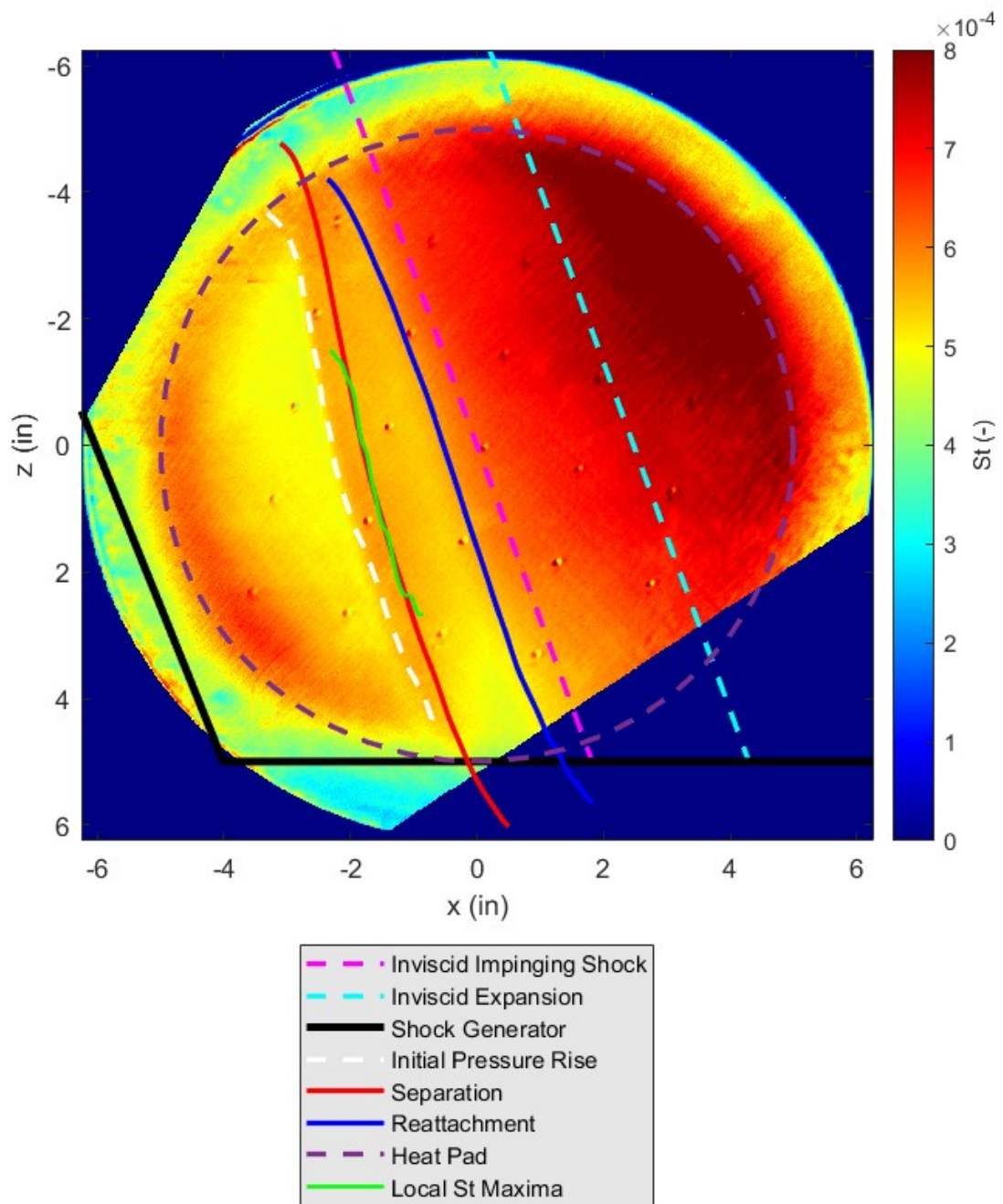
Figure 3.29: Maximum Stanton number distribution over the separation line.

(a) $M = 2.3, \psi = 20°$ (b) $M = 2.3, \psi = 40°$
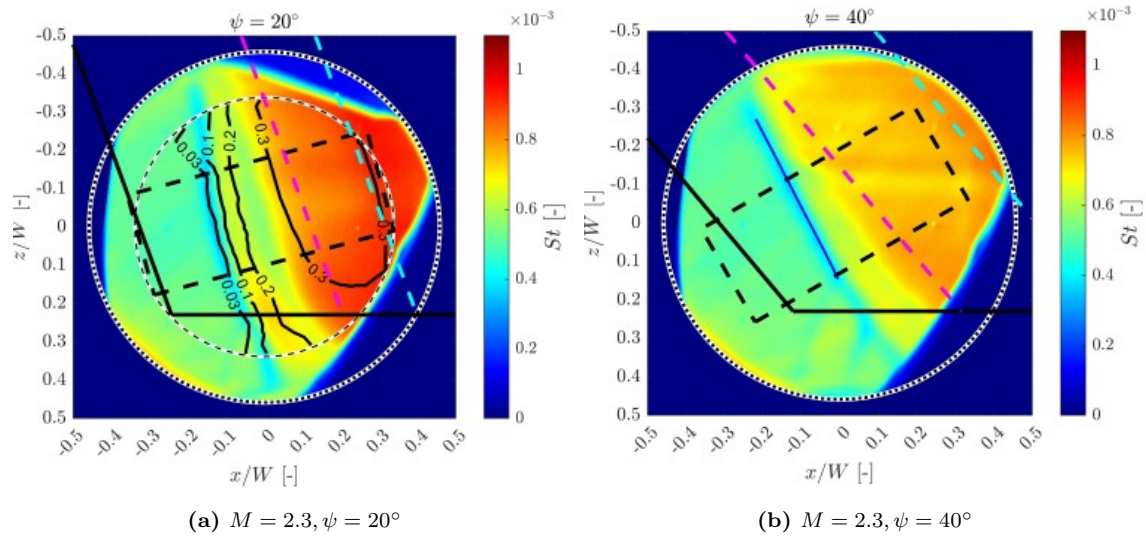
Figure 3.30: Mean pressure and Stanton number comparison in ISWT Vitols (2024).
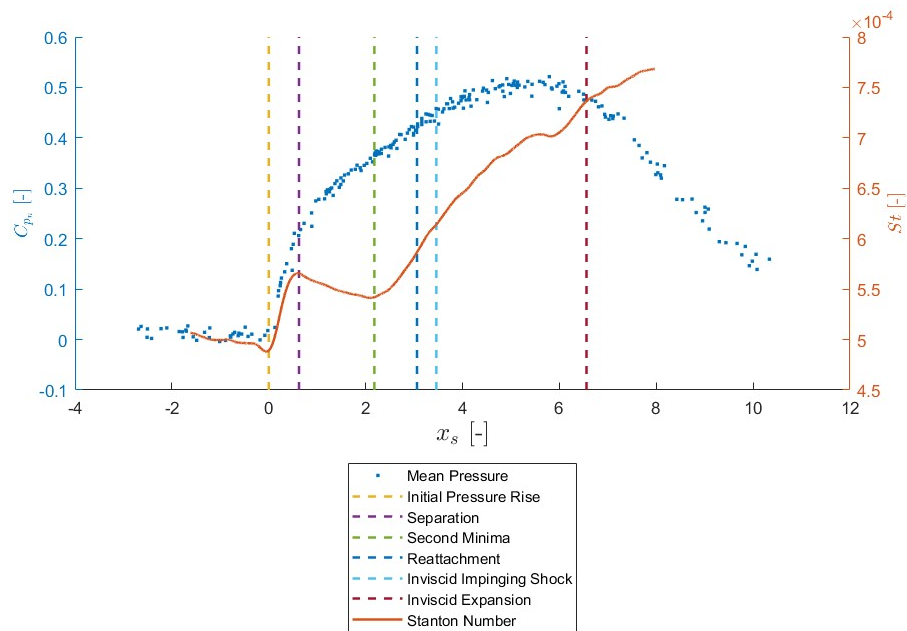
Figure 3.31: Stanton Number and mean pressure distribution with associated flow features for $M = 2.1, \psi = 20°, C_{p_n} = 0.6$.
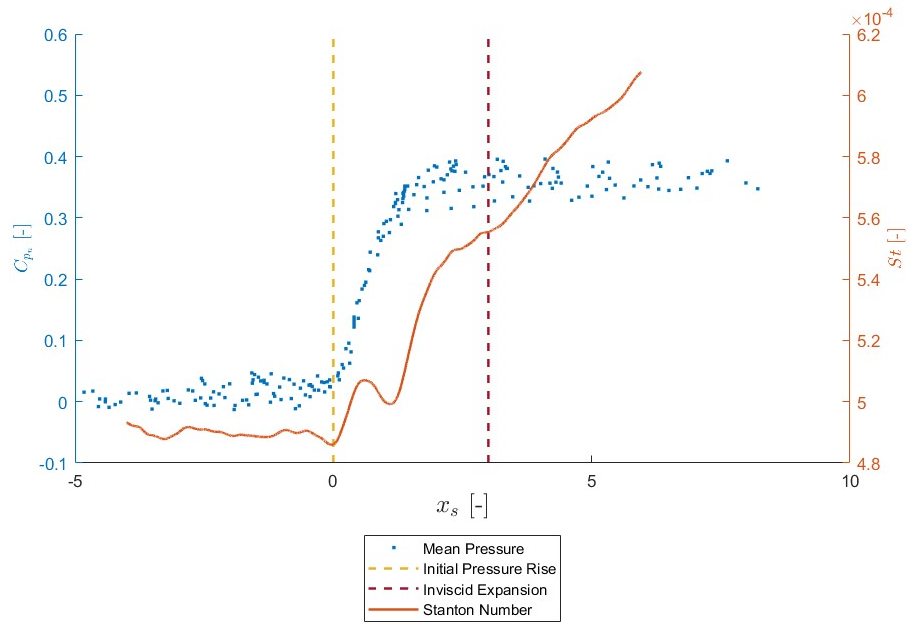
Figure 3.32: Stanton Number and mean pressure distribution with associated flow features for $M = 2.1, \psi = 40°, C_{p_n} = 0.6$.
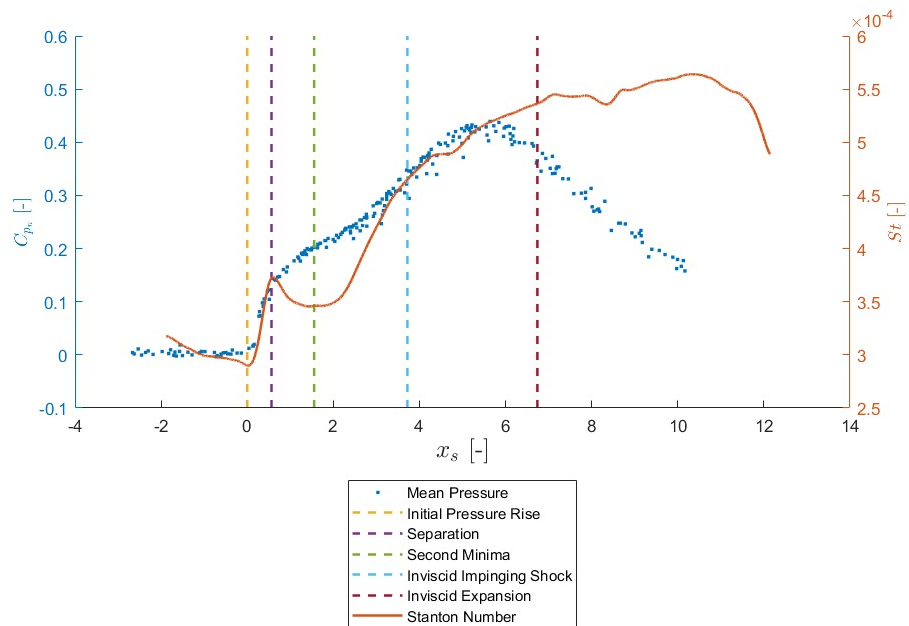
Figure 3.33: Stanton Number and mean pressure distribution with associated flow features for $M = 3.0, \psi = 20°, C_{p_n} = 0.6$.
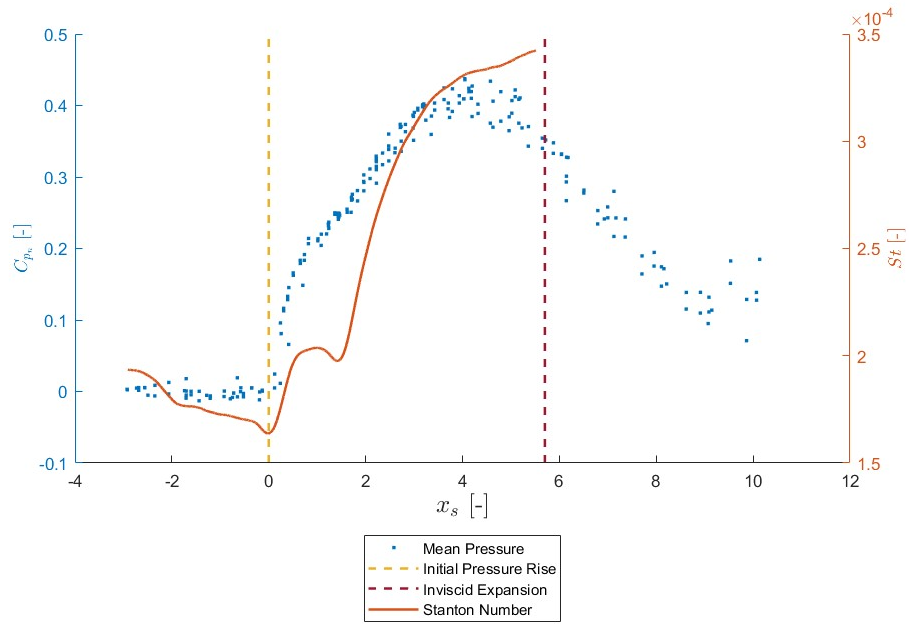
Figure 3.34: Stanton Number and mean pressure distribution with associated flow features for $M = 3.0, \psi = 40°, C_{p_n} = 0.6$.
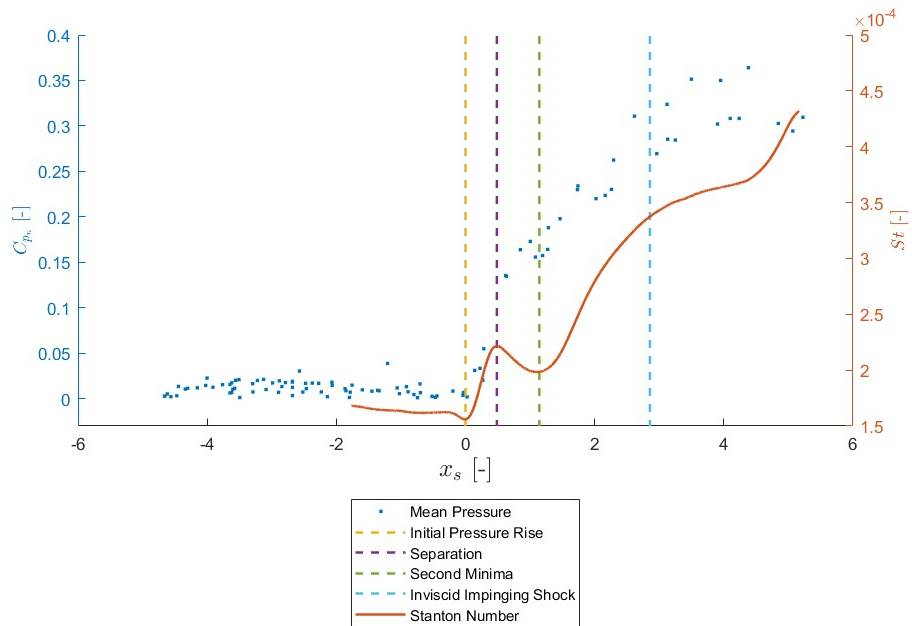
Figure 3.35: Stanton Number and mean pressure distribution with associated flow features for $M = 3.0, \psi = 20°, C_{p_n} = 0.4$.

This is true for all cases except the 20° case at Mach 2.1 in which the known location of the separation and reattachment from oil flow are used. Lastly, the known location of the expansion fan is plotted on each distribution.

The first flow feature marked is the initial influence of the interaction on the freestream. This value shows good correlation of the first St minima and the initial pressure rise as was previously highlighted. The next flow feature highlighted is the separation line. For the Mach 2.1 case, this shows excellent agreement with the local maxima of the St distribution. For the rest of the cases, the added separation line based on the St distribution does correlate well to the pressure distribution, although the precision of this comparison is difficult due to the gradual slopes seen in the pressure distributions. As previously mentioned, the onset of separation occurs just before the pressure plateau. Hayashi et al. (1986) proved this St maxima with for the 2-D case aligned well with this location. The location of the maxima for these cases again looks to overlap relatively well, but it is noted that it is difficult to see the exact location of the onset of this plateau region, so further work should be done to confirm these results. Looking at the 40° case for Mach 2.1 flow, it is even noted that a slight change in slope of the mean pressure distribution is seen where the separation line would be if the flow had separated.

The next flow feature is the inviscid impinging shock line. This is location is know, but it can be used to help estimated the location of the reattachment line. This feature is much more difficult to determine an exact location for, so confidence in the location of reattachment based on the St distribution is much lower compared to the other two extracted flow features from the St distribution. However, looking at Figures 3.36 - 3.40, there is a slight decrease in the slope of the line after the second local Stanton number minima and just before the location of the inviscid impinging shock location. This change in slope is the reattachment line. This is can be clearly seen in Figure 3.33 and Figure 3.35, which shows the location of the inviscid impinging shock just downstream of the change in slope of the Stanton number distribution. This feature is less prominent in the the the Mach 2.1 case (Figure 3.31), and is likely a result of the less clear image produced in the Mach 2.1 experiments. It can therefore be inferred that the location of reattachment is just at or before the change in slope of the Stanton distribution downstream of the second local minima for each case.
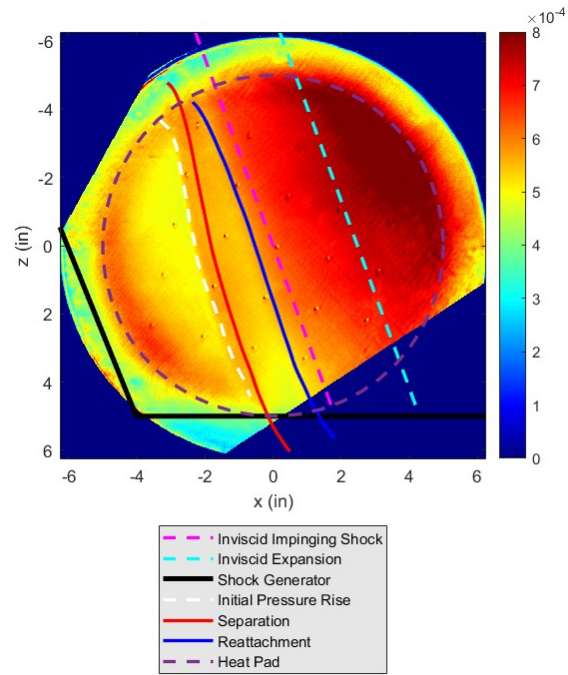
Figure 3.36: Stanton number and associated flow features for $M = 2.1, \psi = 20°, C_{p_n} = 0.6$
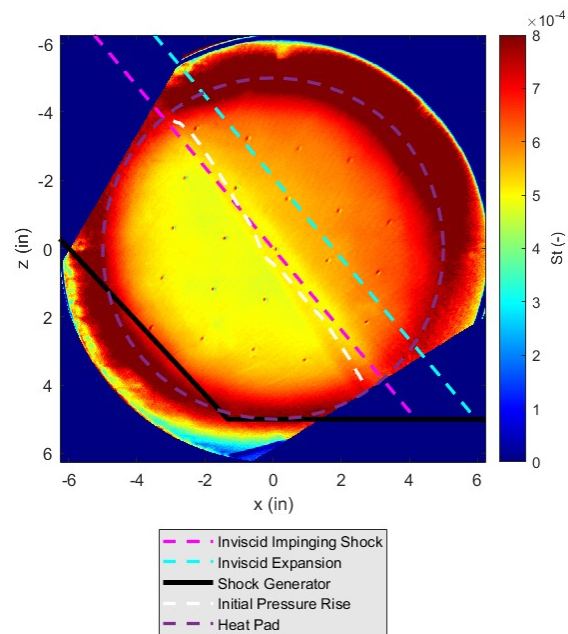
Figure 3.37: Stanton number and associated flow features for $M = 2.1, \psi = 40°, C_{p_n} = 0.6$

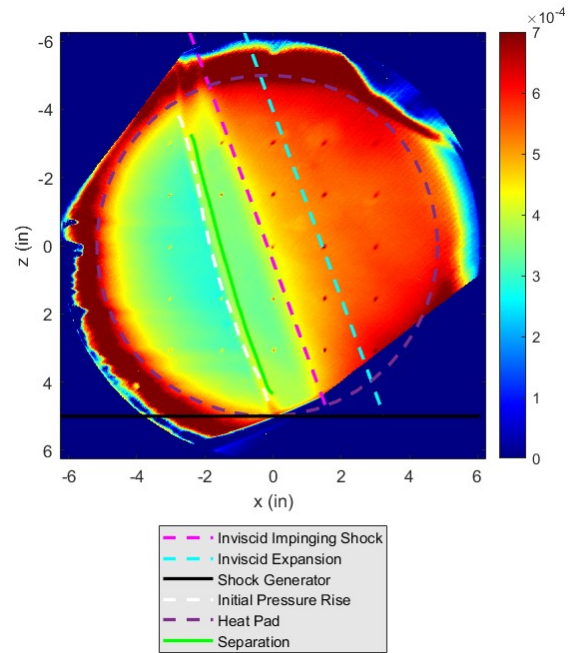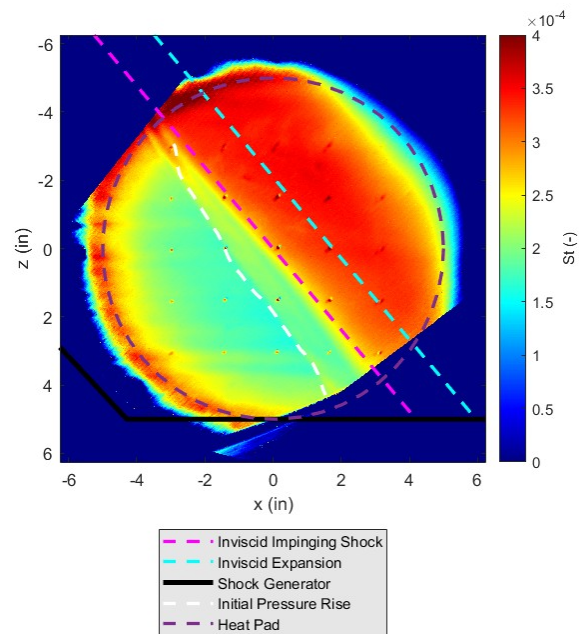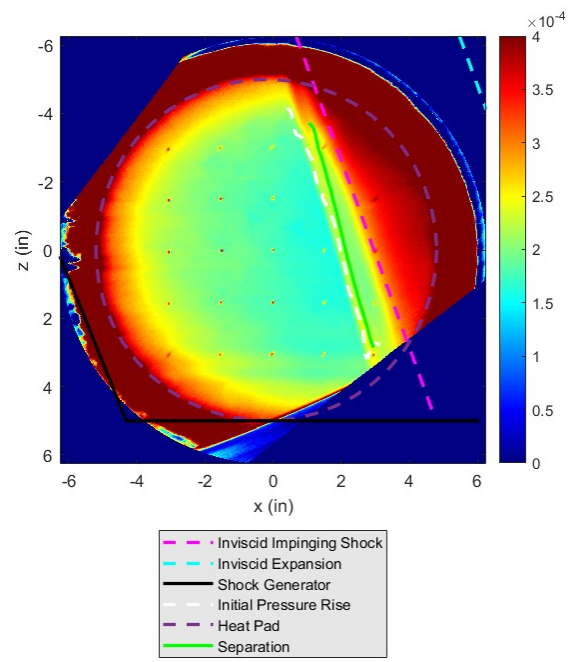**Figure 3.38:** Stanton number and associated flow features for $M = 3.0, \psi = 20°, C_{p_n} = 0.6$

Figure 3.39: Stanton number and associated flow features for $M = 3.0, \psi = 40°, C_{p_n} = 0.6$

Figure 3.40: Stanton number and associated flow features for $M = 3.0, \psi = 20°, C_{p_n} = 0.4$

Chapter 4

Conclusion

Swept SBLIs have been studied in Mach 2.1 and Mach 3.0 flow at 20 and 40° sweep angles on a fully turbulent boundary layer in the 15-in x 15-in Arizona Polysonic Wind Tunnel (APWT). The mean flow topology is characterized using oil flow visualization, heat flux measurements, and mean pressure measurements. The overall goal of this work is to determine if increasing the aspect ratio of the shock generator produces the same mean flow topology in the swept SBLI. Heat flux measurements and mean pressure measurements offer useful insight into the relevant features of the SBLI, and oil flow visualization is used to confirm the results found by the other two methods. By comparing these methods directly, each case shows good agreement between methods and results found in the literature. Furthermore, these results show good agreement with work done with a smaller aspect ratio shock generator in the 3.25-in x 4.75-in Arizona Indraft Supersonic Wind Tunnel (ISWT).

Previous work from ISWT has shown that a 40° sweep with a normal pressure rise across the shock of $C_{p_n} = 0.6$ produces no sign of separation, but a 30° sweep angle at the same pressure rise does separate (Vitols, 2024). It has also been concluded that the mean conical similarity in the ISWT case is partially influenced by limited span of the tunnel. APWT results show that the 20° sweep case is separated, but the 40° is not for both Mach 2.1 and Mach 3.0. This is consistent with results from the smaller aspect ratio experiments in ISWT. However, results from the 40° sweep case at Mach 2.1 of this experiment require further validation due to the location of the impinging expansion fan possibly interacting with the SBLI. Further, the effect of the expansion fan on the SBLI should be studied for all cases, both in APWT and ISWT. For the 20° sweep case, it is found that separation evolves with conical similarity near the root of the shock generator, but shows signs of cylindrical behavior further along the span. Therefore, increasing the aspect ratio (as done in APWT) seems to allow the interaction to become cylindrical due to a larger span. Higher aspect ratio experiments would help to confirm this.

Heat flux measurements were used to determine the adiabatic wall temperature of the interaction. It is widely known that the recovery temperature of the freestream boundary layer is approximately $Pr^{1/3} \approx 0.896$, and results from Mach 3.0 runs are in good agreement with this. With the Mach 2.1 having an unknown total temperature, the total temperature was estimated such that the recovery factor in the freestream aligned with this principle. Results from this show that the recovery factor increases to nearly one at the separation

line, then decreases back to freestream conditions in the separation region. Finally, it increases again near reattachment and remains higher than the freestream recovery factor before the interaction.

A more complete test matrix is required to draw additional conclusions, but some trends are noted here.

- An increase in Mach number increases the amplitude of the initial pressure plateau for similar sweep cases. This includes data from APWT at Mach 2.1 and Mach 3.0, as well as data from ISWT at Mach 2.3. Further, changing only the C_{p_n} appears to also show similar magnitude for the initial pressure rise of the C_{p_n} distribution which is in agreement with Free Interaction Theory. It is therefore suggested that the C_{p_n} distribution follows Free Interaction Theory for 3-D SBLIs, but the C_p distribution should be investigated as well.

- The boundary layer at the designed $C_{p_n} = 0.6$ stays attached at a sweep angle somewhere between 20° and 40° sweep in APWT, and results from ISWT show that this transition is between 30° and 40°. Due to the many other similarities between results from ISWT and APWT, this maximum sweep angle that has a separated region is likely at a similar angle for both tunnels.

- While the change in Reynolds number was minimal for the tests done in APWT, no discernible differences are seen in the interaction features. A larger change in Reynolds number is seen when utilizing data taken from ISWT. Theory suggests this has little impact on the structure of the SBLIs and the major differences between APWT and ISWT are a result of other factors (aspect ratio, Mach number, etc.), but it is unclear if this results in any differences between the two cases.

- The increase in aspect ratio appears to show that the flow could develop cylindrical similarity provided the value is high enough. Results between APWT and ISWT are consistent when comparing the mean flow topology near the root of the interactions. This suggests that results from ISWT are impacted by sidewall effects, and a longer span of the interaction results in cylindrical similarity rather conical similarity.

- Scaling the interaction by boundary layer height allows for comparison between two different wind tunnels with similar boundary layer profiles, but very different boundary layer heights.

Future work should include a continuation of this test matrix with more Mach numbers, an increased aspect ratio, and more sweep angles. It would also be useful to run the 40° case with an increased distance of the expansion fan to investigate its influence on the SBLI. Further validation that the separation region becomes cylindrical given enough span would also be beneficial, and an increased aspect ratio would be able to prove this. To improve oil flow visualization, a different method should be implemented in APWT since startup features caused most of the kerosene to evaporate. This was particularly challenging in the Mach 3.0 case. The Mach 2.1 oil flow data from APWT is reliable, but a validation with oil flow visualization at higher Mach numbers would improve confidence in the overall interpretation. Future heat flux measurements can also be improved by having a more uniform heat surface. This would allow for a more accurate measurement

of the Stanton number across the entire span of the plug and ensure the entire surface can be utilized when studying the SBLI. Other factors of interest include varying C_{p_n} and studying the impact of the boundary layer state. Finally, unsteady pressure measurements would provide useful information about the interaction at each of these configurations.

Appendix A

Ketron® 1000 PEEK

Poly-ether-ether-ketone

Ketron® 1000 Polyetheretherketone PEEK is an unfilled, general purpose grade that offers the highest elongation and toughness of all materials in the PEEK family. Ideal for instrument and seal components, where ductility and inertness are critical, Ketron® 1000 PEEK shapes are known for their ability to fit within a variety of applications and industries.

PRODUCT DATASHEET

		ISO*			ASTM*		
		Test methods	Units	Indicative values	Test methods	Units	Indicative values
Thermal properties (1)	Melting temperature (DSC, 10°C (50°F) / min)	ISO 11357-1/-3	°C	340	ASTM D3418	°F	644
	Glass transition temperature (DMA- Tan δ) (2)		°C			°F	
	Thermal conductivity at 23°C (73°F)		W/(K.m)	0.25		BTU.in./(hr.ft².°F)	1.75
	Coefficient of linear thermal expansion (-40 to 150 °C) (-40 to 300°F)				ASTM E-831 (TMA)	µin./in./°F	26
	Coefficient of linear thermal expansion (23 to 100°C) (73°F to 210°F)		µm/(m.K)	50			
	Coefficient of linear thermal expansion (23 to 150°C) (73°F to 300°F)		µm/(m.K)	55			
	Coefficient of linear thermal expansion (>150°C) (> 300°F)		µm/(m.K)	130			
	Heat Deflection Temperature: method A: 1.8 MPa (264 PSI)	ISO 75-1/-2	°C	160	ASTM D648	°F	320
	Continuous allowable service temperature in air (20.000 hrs) (3)		°C	250		°F	480
	Min. service temperature (4)		°C	-50		°F	
	Flammability: UL 94 (3 mm (1/8 in.)) (5)			V-0			V-0
	Flammability: Oxygen Index	ISO 4589-1/-2	%	35			
Mechanical Properties (6)	Tensile strength	ISO 527-1/-2 (7)	MPa	115	ASTM D638 (8)	PSI	16,000
	Tensile strain (elongation) at yield	ISO 527-1/-2 (7)	%	5	ASTM D638 (8)	%	5
	Tensile strain (elongation) at break	ISO 527-1/-2 (7)	%	17	ASTM D638 (8)	%	40
	Tensile modulus of elasticity	ISO 527-1/-2 (9)	MPa	4,300	ASTM D638 (8)	KSI	630
	Shear Strength			55	ASTM D732	PSI	8,000
	Compressive stress at 1 / 2 / 5 % nominal strain	ISO 604 (10)	MPa	38 / 75 / 140			
	Compressive strength				ASTM D695 (11)	PSI	20,000
	Charpy impact strength - unnotched	ISO 179-1/1eU	kJ/m²	no break			
	Charpy impact strength - notched	ISO 179-1/1eA	kJ/m²	3.5			
	Izod Impact notched				ASTM D256	ft.lb./in	0.60
	Flexural strength	ISO 178 (12)	MPa	170	ASTM D790 (13)	PSI	25,000
	Flexural modulus of elasticity	ISO 178 (12)	MPa		ASTM D790	KSI	600
	Rockwell M hardness (14)	ISO 2039-2		105	ASTM D785		100
	Rockwell R hardness (14)	ISO 2039-2			ASTM 2240		126
Electrical Properties	Electric strength	IEC 60243-1 (15)	kV/mm	24	ASTM D149	Volts/mil	480
	Volume resistivity	IEC 62631-3-1	Ohm.cm	10E13	ASTM D257	Ohm.cm	
	Surface resistivity	ANSI/ESD STM 11.11	Ohm/sq.	10E12	ANSI/ESD STM 11.11	Ohm/sq.	10E12
	Dielectric constant at 1 MHz	IEC 62631-2-1		3.2	ASTM D150		3.3
	Dissipation factor at 1MHz	IEC 62631-2-1		0	ASTM D150		0
Miscellaneous	Colour			Tan, Black			Tan, Black
	Density	ISO 1183-1	g/cm³	1.31			
	Specific Gravity				ASTM D792		1.31
	Water absorption after 24h immersion in water of 23 °C (73°F)	ISO 62 (16)	%	0.06	ASTM D570 (17)	%	0.10
	Water absorption at saturation in water of 23 °C (73°F)		%	0.45	ASTM D570 (17)	%	0.5
	Wear rate	ISO 7148-2 (18)	µm/km	28	QTM 55010 (19)	In³.min/ft.lbs.hrX10⁻¹⁰	375
	Dynamic Coefficient of Friction (-)	ISO 7148-2 (18)		0.3-0.5	QTM 55007 (20)		0.32
	Limiting PV at 100 FPM				QTM 55007 (21)	ft.lbs/in².min	8,500
	Limiting PV at 0.1 / 1 m/s cylindrical sleeve bearings		MPa.m/s	0.33 / 0.21			
	Limiting PV at 0.5 m/s cylindrical sleeve bearings	QTM 55007 (21)	MPa.m/s				
	Chemical Resistance	www.mcam.com/en/support/chemical-resistance-information			www.mcam.com/en/support/chemical-resistance-information		

Note: 1 g/cm³ = 1,000 kg/m³ ; 1 MPa = 1 N/mm² ; 1 kV/mm = 1 MV/m   NYP: there is no yield point

This table, mainly to be used for comparison purposes, is a valuable help in the choice of a material. The data listed here fall within the normal range of product properties of dry material. However, they are not guaranteed and they should not be used to establish material specification limits nor used alone as the basis of design. See the remaining notes on the next page.

Ketron® is a registered trademark of Mitsubishi Chemical Advanced Materials

mcam.com

References

F. S. Alvi and G. S. Settles. Physical model of the swept shock wave/boundary-layer interaction flowfield. *AIAA Journal*, 30(9):2252–2258, 1992. doi: 10.2514/3.11212. URL https://doi.org/10.2514/3.11212.

O. Bardsley and W. Mair. Iii. the interaction between an oblique shock-wave and a turbulent boundary-layer. *The London, Edinburgh, and Dublin Philosophical Magazine and Journal of Science*, 42(324):29–36, 1951. doi: 10.1080/14786445108561220. URL https://doi.org/10.1080/14786445108561220.

A. Ceci, A. Palumbo, J. Larsson, and S. Pirozzoli. On low-frequency unsteadiness in swept shock wave–boundary layer interactions. *Journal of Fluid Mechanics*, 956:R1, 2023. doi: 10.1017/jfm.2023.2.

A. Ceci, A. Palumbo, J. Larsson, and S. Pirozzoli. Low-frequency unsteadiness in hypersonic swept shock wave-boundary layer interactions. *Phys. Rev. Fluids*, 9:054603, May 2024. doi: 10.1103/PhysRevFluids.9.054603. URL https://link.aps.org/doi/10.1103/PhysRevFluids.9.054603.

D. R. Chapman, D. M. Kuehn, and H. K. Larson. Investigation of separated flows in supersonic and subsonic streams with emphasis on the effect of transition. 1958. URL https://api.semanticscholar.org/CorpusID:55890391.

N. T. Clemens and V. Narayanaswamy. Low-frequency unsteadiness of shock wave/turbulent boundary layer interactions. *Annual Review of Fluid Mechanics*, 46(Volume 46, 2014):469–492, 2014. ISSN 1545-4479. doi: https://doi.org/10.1146/annurev-fluid-010313-141346. URL https://www.annualreviews.org/content/journals/10.1146/annurev-fluid-010313-141346.

R. A. Dawson, C. Pederson, and J. C. Little. *Effects of Sweep on Impinging Oblique Shock-Turbulent Boundary Layer Interaction*. American Institute of Aeronautics and Astronautics, 2015. doi: 10.2514/6.2015-2933. URL https://arc.aiaa.org/doi/abs/10.2514/6.2015-2933.

A. Doehrmann. Mean flow structure of swept impinging oblique shock boundary layer interactions. Master's thesis, The University of Arizona, 2018.

D. Dolling. *Effects of Mach number on upstream influence in sharp fin-induced shock wave turbulent boundary layer interaction*. American Institute of Aeronautics and Astronautics, 1984. doi: 10.2514/6.1984-95. URL https://arc.aiaa.org/doi/abs/10.2514/6.1984-95.

D. D. Dooner, N. F. Giannelis, and A. J. Neely. Design of a wind tunnel model to investigate hypersonic double-swept shock boundary layer interaction. In *AIAA SCITECH 2024 Forum*, page 1049, 2024.

J. Délery and J. P. Dussauge. Some physical aspects of shock wave/boundary layer interactions. *Shock Waves*, 19:453–468, 2009. doi: 10.1007/s00193-009-0220-z. URL https://doi.org/10.1007/s00193-009-0220-z.

J. Erdös, C. Dlaska, P. Szatmary, M. Humenberger, V. Vécsei, and S. Hajdu. Acute compartment syndrome in children: a case series in 24 patients and review of the literature. *International orthopaedics*, 35:569–575, 2011.

M. E. Erengil and D. S. Dolling. Effects of sweepback on unsteady separation in mach 5 compression ramp interactions. *AIAA Journal*, 31(2):302–311, 1993. doi: 10.2514/3.60176. URL https://doi.org/10.2514/3.60176.

H. H. Fernholz and P. J. Kline. On the breakdown of the crocco temperature-velocity relationship and the law of the wall in compressible two-dimensional turbulent boundary layers. In R. Dumas and L. Fulachier, editors, *Structure of Complex Turbulent Shear Flow*, pages 311–323, Berlin, Heidelberg, 1983. Springer Berlin Heidelberg. ISBN 978-3-642-81991-9.

A. Ferri. Technical memorandum - national advisory committee for aeronautics., 1939. ISSN 0096-7602.

G. E. Gadd, D. W. Holder, and J. D. Regan. An experimental investigation of the interaction between shock waves and boundary layers. *Proceedings of the Royal Society of London. Series A, Mathematical and Physical Sciences*, 226(1165):227–253, 1954. ISSN 00804630. URL http://www.jstor.org/stable/99431.

D. V. Gaitonde and M. C. Adler. Dynamics of three-dimensional shock-wave/boundary-layer interactions. *Annual Review of Fluid Mechanics*, 55(Volume 55, 2023):291–321, 2023. ISSN 1545-4479. doi: https://doi.org/10.1146/annurev-fluid-120720-022542. URL https://www.annualreviews.org/content/journals/10.1146/annurev-fluid-120720-022542.

B. Ganapathisubramani, N. T. Clemens, and D. S. Dolling. Low-frequency dynamics of shock-induced separation in a compression ramp interaction. *Journal of Fluid Mechanics*, 636:397–425, Oct 10 2009. URL https://ezproxy.library.arizona.edu/login?url=https://www.proquest.com/scholarly-journals/low-frequency-dynamics-shock-induced-separation/docview/210878045/se-2. Copyright - Copyright © Cambridge University Press 2009; Last updated - 2024-10-04; SubjectsTermNotLitGenreText - Environmental.

R. Giepman, F. Schrijer, and B. Van Oudheusden. A parametric study of laminar and transitional oblique shock wave reflections. *Journal of Fluid Mechanics*, 844:187–215, 2018.

T. J. Goldberg. Three-dimensional separation for interaction of shock waves with turbulent boundary layers. *AIAA Journal*, 11(11):1573–1575, November 1973.

A. Gross, J. C. Little, and H. F. Fasel. *Numerical Investigation of Shock Wave Turbulent Boundary Layer Interactions.* American Institute of Aeronautics and Astronautics, 2018. doi: 10.2514/6.2018-1807. URL https://arc.aiaa.org/doi/abs/10.2514/6.2018-1807.

J. Hainsworth, R. Dawson, and J. C. Little. *Experimental Study of Unswept and Swept Oblique Shock-Turbulent Boundary Layer Interactions.* American Institute of Aeronautics and Astronautics, 2014. doi: 10.2514/6.2014-2738. URL https://arc.aiaa.org/doi/abs/10.2514/6.2014-2738.

M. Hayashi and S. Aso. *Fluctuation of heat transfer in shock wave/turbulent boundary layer interaction.* American Institute of Aeronautics and Astronautics, 1986. doi: 10.2514/6.1988-426. URL https://arc.aiaa.org/doi/abs/10.2514/6.1988-426.

M. Hayashi, A. Sakurai, and S. Aso. Measurement of heat-transfer coefficients in shock wave-turbulent boundary layer interaction regions with a multi-layered thin film heat transfer gauge. In *NASA Technical Memorandum*, 1986. URL https://api.semanticscholar.org/CorpusID:93321177.

M. Holden. *Experimental studies of quasi-two-dimensional and three-dimensional viscous interaction regions induced by skewed-shock and swept-shock boundary layer interaction.* American Institute of Aeronautics and Astronautics, 1984. doi: 10.2514/6.1984-1677. URL https://arc.aiaa.org/doi/abs/10.2514/6.1984-1677.

R. A. Humble, F. Scarano, and B. W. van Oudheusden. Particle image velocimetry measurements of a shock wave/turbulent boundary layer interaction. *Experiments in Fluids*, 43(2):173–183, 2007. ISSN 1432-1114. doi: 10.1007/s00348-007-0337-8. URL https://doi.org/10.1007/s00348-007-0337-8.

L. Ibos, J.-P. Monchau, V. Feuillet, J. Dumoulin, P. Ausset, J. Hameury, and B. Hay. Investigation of the directional emissivity of materials using infrared thermography coupled with a periodic excitation. 01 2016. doi: 10.21611/qirt.2016.031.

M. Jurkovich. *Flow visualization studies of a 3-D shock/boundary layer interactionin the presence of a non-uniform approach boundary layer.* American Institute of Aeronautics and Astronautics, 1984. doi: 10.2514/6.1984-1560. URL https://arc.aiaa.org/doi/abs/10.2514/6.1984-1560.

K. Koca, S. Keskin, R. Şahin, D. Veerasamy, and M. S. Genç. Measurements of flow characterization revealing transition to turbulence associated with the partial flexibility-based flow control at low reynolds number. *Arabian Journal for Science and Engineering*, July 2024. ISSN 2191-4281. doi: 10.1007/s13369-024-09349-z. URL https://doi.org/10.1007/s13369-024-09349-z.

R. H. Korkegi. A simple correlation for incipient-turbulent boundary-layer separation due to a skewed shock wave. *AIAA Journal*, 11(11):1578–1579, 1973. doi: 10.2514/3.50637. URL https://doi.org/10.2514/3.50637.

S. Lee and A. Gross. Numerical investigation of sweep effect on turbulent shock-wave boundary-layer interaction. *AIAA Journal*, 60(2):712–730, 2022.

F. K. Lu, G. S. Settles, and C. C. Horstman. Mach number effects on conical surface features of swept shock-wave/boundary-layer interactions. *AIAA Journal*, 28(1):91–97, 1990. doi: 10.2514/3.10357. URL https://doi.org/10.2514/3.10357.

J. Matheis and S. Hickel. On the transition between regular and irregular shock patterns of shock-wave/boundary-layer interactions. *Journal of Fluid Mechanics*, 776:200–234, 2015.

S. Mazdeyasna, P. Ghassemi, and Q. Wang. Best practices for body temperature measurement with infrared thermography: External factors affecting accuracy. *Sensors*, 23(18), 2023. ISSN 1424-8220. doi: 10.3390/s23188011. URL https://www.mdpi.com/1424-8220/23/18/8011.

A. McCabe. The three-dimensional interaction of a shock wave with a turbulent boundary layer. *Aeronautical Quarterly*, XVII:231–252, August 1966.

W. Merzkirch. *Flow Visualization*. Academic Press, 2 edition, 1987.

A. J. Musker. Explicit expression for the smooth wall velocity distribution in a turbulent boundary layer. *AIAA Journal*, 17(6):655–657, 1979.

S. Padmanabhan. *Swept Impinging Oblique Shock Boundary Layer Interactions*. PhD thesis, The University of Arizona, 2023.

S. Padmanabhan, J. C. Maldonado, J. A. Threadgill, and J. C. Little. Experimental study of swept impinging oblique shock/boundary-layer interactions. *AIAA journal*, 59(1):140–149, 2021a.

S. Padmanabhan, J. C. Maldonado, J. A. S. Threadgill, and J. C. Little. Experimental study of swept impinging oblique shock/boundary-layer interactions. *AIAA Journal*, 59(1):140–149, 2021b. doi: 10.2514/1.J058910. URL https://doi.org/10.2514/1.J058910.

S. Padmanabhan, J. A. Threadgill, and J. C. Little. Flow similarity in swept shock/boundary layer interactions. In *AIAA Scitech 2022 Forum*, page 0942, 2022.

S. Piponniau, J. P. Dussauge, J. F. Debieve, and P. Dupont. A simple model for low-frequency unsteadiness in shock-induced separation. *Journal of Fluid Mechanics*, 629:87–108, 2009. doi: 10.1017/S0022112009006417.

A. Pope and K. Goin. *High Speed Wind Tunnel Testing*. Wiley, 1965. ISBN 9780471694021. URL https://books.google.com/books?id=yHFTAAAAMAAJ.

J. A. Rataczak, C. L. Running, and T. J. Juliano. Verification of quantitative infrared thermography heat-flux measurements. *Experimental Thermal and Fluid Science*, 121:110274, 2021. ISSN 0894-1777. doi: https://doi.org/10.1016/j.expthermflusci.2020.110274. URL https://www.sciencedirect.com/science/article/pii/S0894177720307779.

R. Rosen, D. Pavish, and A. Roshko. *A two-layer calculation for the initial interaction region of an unseparated supersonic turbulent boundary layer with a ramp*, pages 80–135. American Institute of Aeronautics and Astronautics, 1980. doi: 10.2514/6.1980-135. URL https://arc.aiaa.org/doi/abs/10.2514/6.1980-135.

H. W. L. A. Roshko and S. Dshawan. On reflection of shock waves from boundary layers, 1952.

M. R. Saad, A. C. Idris, H. Zare-Behtash, and K. Kontis. Flow visualization of shock wave/boundary-layer interaction controlled by micro-ramp at mach 5. In *Proceedings of the 6th European Conference for Aeronautics and Space Sciences (EUCASS)*, Kuala Lumpur, Malaysia, 2023. European Conference for Aeronautics and Space Sciences. Faculty of Engineering, National Defence University of Malaysia and School of Engineering, University of Glasgow.

H. Schlichting. *Boundary Layer Theory*. Springer, Berlin, 7th edition, 1979. ISBN 978-3-540-09158-3.

G. S. Settles and R. L. Kimmel. Similarity of quasiconical shock wave/turbulent boundary-layer interactions. *AIAA Journal*, 24(1):47–53, 1986. doi: 10.2514/3.9221. URL https://doi.org/10.2514/3.9221.

G. S. Settles and H.-Y. Teng. Cylindrical and conical flow regimes of three-dimensional shock/boundary-layer interactions. *AIAA journal*, 22(2):194–200, 1984.

G. S. Settles, C. C. Horstman, and T. M. McKenzie. Experimental and computational study of a swept compression corner interaction flowfield. *AIAA Journal*, 24(5):744–752, 1986. doi: 10.2514/3.9341. URL https://doi.org/10.2514/3.9341.

L. Souverein, P. Bakker, and P. Dupont. A scaling analysis for turbulent shock-wave/boundary-layer interactions. *Journal of Fluid Mechanics*, 714:505–535, 2013.

D. Spalding. A procedure for the calculation of boundary layers confined in ducts. *Journal of engineering physics*, 19(3):1085–1090, 1970.

R. I. Stalker. The pressure rise at shock-induced turbulent boundary-layer separation in three-dimensional supersonic flow. *Journal of Aeronautical Sciences*, (7), 1957.

C.-C. Sun and M. E. Childs. A modified wall wake velocity profile for turbulent compressible boundary layers. *Journal of Aircraft*, 10(6):381–383, 1973. doi: 10.2514/3.44376. URL https://doi.org/10.2514/3.44376.

O. Szulc, P. Doerffer, P. Flaszynski, and M. Braza. Moving wall effect on normal shock wave–turbulent boundary layer interaction on an airfoil. *International Journal of Numerical Methods for Heat Fluid Flow*, 34(7):2567–2600, 2024. URL https://doi.org/10.1108/HFF-06-2023-0338.

Y. Tao, X. Fan, and Y. Zhao. Viscous effects of shock reflection hysteresis in steady supersonic flows. *Journal of fluid mechanics*, 759:134–148, 2014.

J. A. Threadgill and P. J. Bruce. Shock wave boundary layer interaction unsteadiness: the effects of configuration and strength. In *54th AIAA aerospace sciences meeting*, page 0077, 2016.

J. A. Threadgill, I. Stab, A. Doehrmann, and J. C. Little. *Three-Dimensional Flow Features of Swept Impinging Oblique Shock/Boundary-Layer Interactions.* American Institute of Aeronautics and Astronautics, 2017. doi: 10.2514/6.2017-0759. URL https://arc.aiaa.org/doi/abs/10.2514/6.2017-0759.

J. A. S. Threadgill and J. C. Little. An inviscid analysis of swept oblique shock reflections. *Journal of Fluid Mechanics*, 890:A22, 2020. doi: 10.1017/jfm.2020.117.

F. D. Turbeville, C. Broslawski, and J. S. Cheatwood. *Progress on Quantitative Infrared Thermography at the NASA Langley Aerothermodynamic Laboratory.* AIAA, 2024. doi: 10.2514/6.2024-4281. URL https://arc.aiaa.org/doi/abs/10.2514/6.2024-4281.

E. R. Van Driest. Turbulent boundary layer in compressible fluids. *Journal of Spacecraft and Rockets*, 40 (6):1012–1028, 2003. doi: 10.2514/2.7048. URL https://doi.org/10.2514/2.7048.

L. Vanstone, M. N. Musta, S. Seckin, and N. Clemens. Experimental study of the mean structure and quasi-conical scaling of a swept-compression-ramp interaction at mach 2. *Journal of Fluid Mechanics*, 841:1–27, 2018. doi: 10.1017/jfm.2018.8.

M. Vitols. Mean flow characterization of swept shock/boundary layer interactions: Isolating the influence of sweep. Master's thesis, Technical University Berlin, Berlin, Germany, 2024.

W. R. Wimbrow. Experimental investigation of temperature recovery factors on bodies of revolution at supersonic speeds. Technical Report AD-a380 541, National Advisory Committee for Aeronautics, Washington, D.C., 1949.

G. Wu, Z. Wang, T. Shi, Z. Zhang, W. Jiang, F. Quan, and J. Chang. Effect of expansion waves on cowl shock wave and boundary layer interaction in hypersonic inlet. *Propulsion and Power Research*, 13(1):80–97, 2024. ISSN 2212-540X. doi: https://doi.org/10.1016/j.jppr.2024.02.001. URL https://www.sciencedirect.com/science/article/pii/S2212540X24000038.

L. Xue, Y. Jiao, C. Wang, and K. Cheng. Pressure plateau of separation induced by shock impingement in a mach 5 flow. *Journal of Fluid Mechanics*, 972:R1, 2023. doi: 10.1017/jfm.2023.725.

W. Zhenguo, Z. Yilong, Z. Yuxin, and F. Xiaoqiang. Prediction of massive separation of unstarted inlet via free-interaction theory. *AIAA Journal*, 53(4):1108–1112, 2015.

F.-Y. Zuo, A. Memmolo, and S. Pirozzoli. On wall pressure fluctuations in conical shock wave/turbulent boundary layer interaction. *Journal of Fluid Mechanics*, 967:A3, 2023. doi: 10.1017/jfm.2023.480.